1

1.0	45 2.8	2.5
	50 3.2	2.2
	56 3.6	
1.1	63 4.0	2.0
		1.8
1.25	1.4	1.6

NOTICE

AVIS

Canada

INTEGRATED-OPTIC WAVEGUIDES AND DEVICES

by

Robert Claude Gauthier

©

Submitted in partial fulfilment of the requirements
for the degree of Doctor of Philosophy
at
Dalhousie University
Halifax, Nova Scotia
May, 1988

DALHOUSIE UNIVERSITY

FACULTY OF GRADUATE STUDIES

The undersigned hereby certify that they have read and

recommend to the Faculty of Graduate Studies for acceptance

a thesis entitled " Integrated-Optic Waveguides and

 Devices"

by Robert Claude Gauthier

in partial fulfillment of the requirements for the degree of

Doctor of Philosophy.

Ⓒ

Dated ____ May 01, 1988 ____

External Examiner

Research Supervisor

Examining Committee

to: Cheryl-Anne, Ronald,
Ryan, Jason,
and mine to come

TABLE OF CONTENTS

vi

LIST OF FIGURES

Abstract

This research investigates the optical properties of guided wave optics. The attention is focused on waveguides formed in $LiNbO_3$, an electro-optic crystal, and a GaAs Multiple-Quantum-Well (MQW) structure, a semiconductor. Beam propagations in waveguides with metallic claddings, oriented at an angle to the optical axis and with gaps are studied in $LiNbO_3$ and are configured into several device geometries. The MQW waveguides are studied theoretically by examining the optical power dependent properties of an evanescent directional coupler.

In the waveguide geometries of above, the guided mode's optical properties are observed to depend on the propagation constant. The real component is related to the phase velocity of the guided mode while its imaginary component can lead to power attenuations. Both components are exploited in the design of devices based on the properties of the geometries studied. The waveguide structures studied here are simple in design and can serve as the building blocks for more complex systems.

List of Symbols

cm —- Centimeter

cs —- Cosine

dB —- Decibel

f —- Frequency

k_o —- Free space propagation constant

m —- Meter

mm —- Millimeter

mW —- Milliwatt

n —- Index of refraction

nm —- Nanometer

n_e —- Extraordinary index

n_{eff} —- Effective index of mode

n_o —- Ordinary index

q —- Charge per unit area

r —- Linear electro-optic coefficient

sn —- Sine

t —- Time

x —- x coordinate

x_i —- General coordinate

x_t —- Turning point

y —- y coordinate

z —- z coordinate

AC — Alternating current

B — Magnetic flux density

C — Degree celsius

D — Electric flux density

DC — Direct current

E — Electric field strength

Hg — Mercury

Hz — Hertz

J_f — Current density

L.H.S. — Left hand side

MQW — Multiple-Quantum-Well

R — Quadratic electro-optic coefficient

R.H.S. — Right hand side

T — Rotation tensor

TE — Transverse electric

TM — Transverse magnetic

V — Volt

W — Watt

X — Principal X axis of crystal

Y — Principal Y axis of crystal

Z — Principal Z axis of crystal

β — Propagation constant

λ — Wavelength

θ_p — Prism base angle

σ — Polarization state

θ — Propagation angle

ϵ — Dielectric constant

μm — Micrometer

∇ —- Gradient operator

ρ —- Charge density

μ_o —- Permeability of vacuum

ω —- Angular frequency

ψ —- Transverse electric field

ξ —- Transverse magnetic field

ϵ_o —- Permittivity of vacuum

H —- Magnetic field strength

$\frac{\gamma}{\gamma x}$ —- Partial derivative with respect to x

θ_c —- Critical angle

ϕ —- Phase change

π —- Pi

∞ —- Infinity

$\mathring{A}$ —- Angstrom

γ —- Surface tension

Acknowledgements

There are a larger number of persons who have contributed in this thesis work. To try and thank them all appropriately would require an additional 300 pages to be attached to the thesis.

To my wife Diane, it goes without saying that she plays the most important role in my life. Her support over the past few years has greatly helped in keeping me motivated to complete this degree.

A special thank you to Dr. Barry Paton, for sharing his knowledge with me over the past few years, setting the research in the right direction and not giving up on me.

I would like to thank Dr. Jacek Chrostowski of N.R.C. in Ottawa for providing guidance and facilities so that I was able to perform the building and initial testing of the waveguides. I would also like to thank the support staff at N.R.C. for taking care of the small but important details to keep the work moving smoothly.

Thank you to Dr. M. Cada for taking the time to discuss the various aspects of integrated-optics.

Thank you Christian and Andree Choquet, for opening your home to me, letting me use your car. Your willingness to put up with me made this project possible.

I would like to thank Graham Smith and the staff of Focal Marine Limited for their support and for providing access to key apparatus required in the experiments of the research.

There is always a group of summer students who take care of reorganizing

the labs. I would like to thank Dale Edgar, John Sawler, Brian Peters, and Ian Mackay for their help.

Ruth Allen and Bridget Trim, thank you for keeping the paper work in order and the mail moving.

To the personnel of the machine shop, Alex Feargrieve and Romano Janc, I appreciate the work you did for me.

Kevin, all the best to you. Oh by the way I challenge you to a game of squash.

Thank you to everyone I ever met.

CHAPTER 1.   THE REASON

1.1 Introduction

Light travels in a straight line unless constrained by the media to follow a curved path. Throughout the ages, light guiding technologies have become more sophisticated but limited to short distances primarily due to losses in optical power. The development of the diode laser in the 1960's and low loss optical fibres in the early 1970's, coupled with the information revolution, created a communications speed and distance race. These endeavors have been primarily undertaken by the larger companies and research institutions which have the resources to complement the stringent design and large capital expenditures required. In the university environment, research in the field of guided optical waves has been focused in the areas of fibre and integrated-optics with most of the work performed in the design, building and testing of sensors and discrete components such as modulators, attenuators, polarizers and switches. Fundamental to the understanding of this technology are the principles of guided wave optics.

This thesis will address the concepts of guided wave optics by focusing on waveguides in LiNbO$_3$, an anisotropic dielectric crystal, and waveguides in GaAs, a semiconductor material. It will be shown that the electric and magnetic fields of guided waves depends on several parameters such as the propagation constant (β), the wavelength (λ), the polarization state (σ) and the index of refraction profile (n). Integrated-optic devices such as attenuators, polarizers, switches and modulators can be designed based on the controlled alteration of any of the field's parameters. In the special case of the GaAs based structure, an additional property,

1
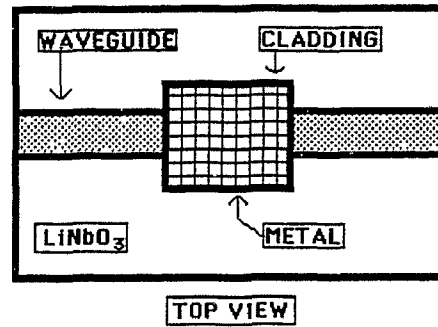
Figure 1.1: Geometry of the integrated-optic waveguide with cladding overlay.

the intensity of the input wave, also influences to a large extent the field profile due to the large nonlinearity exhibited by the waveguide structure. This material enables the possibility of novel all-optical devices.

There are a countless number of waveguide geometries which display the device characteristics mentioned above. For $LiNbO_3$, the research emphasis has been limited to waveguides with claddings, beams propagating at an angle to the optical axis and gaps in otherwise continuous waveguides. For the GaAs based structure, the evanescent wave coupling through a Multiple-Quantum-Well (MQW) is analysed. The waveguide geometries are discussed below along with a diagram of the waveguide configuration. The physical principle of interest is stated together with the interaction mechanism that enables integrated-optic devices to be possible.

1.1.1 Claddings

A typical integrated-optic device with a cladding overlay is shown in figure 1.1. Here the cladding interacts with the optical properties of the waveguide in such a way as to induce or increase the absorption coefficient and thus introduce larger overall propagation losses. The parameter of interest for device applications is the interaction length.
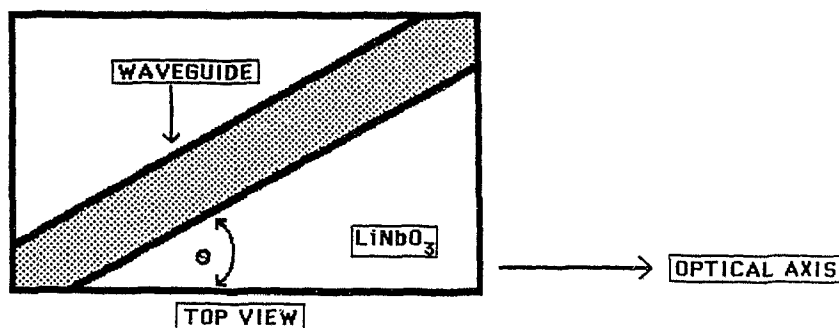
Figure 1.2: Geometry of the integrated-optic waveguide oriented at an angle to the optical axis.

1.1.2 Angles

In the geometry of figure 1.2, the waveguide is oriented at an angle (θ) to the optical axis of the crystal. Due to the anisotropy of the crystal substrate, the optical properties (loss coefficient, polarization rotation and mode selection) of the waveguide depends highly on the choice of propagation angle. The parameter of interest from the point of view of device applications is the electro-optic effect.

1.1.3 Gaps

In figure 1.3, the configuration of the gap containing waveguide is shown. Light which propagates in the waveguide encounters the termination and radiates its energy into the gap region. The second segment of the waveguide recouples a fraction of this energy into guided light. From a device point of view, the changing of the radiation pattern in the gap region is of interest in order to alter the coupling to the second waveguide. This is accomplished through the electro-optic effect.

1.1.4 Multiple-Quantum-Well

The basic design of the evanescent wave directional coupler is shown in figure
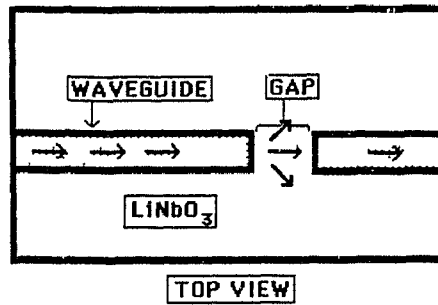
Figure 1.3: Geometry of the integrated-optic waveguide which contains a gap.
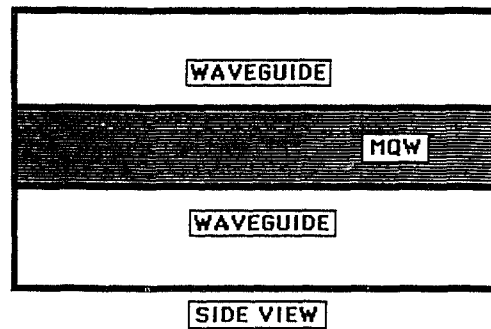
Figure 1.4: Geometry of the evanescent wave coupler.

1.4. It consists of two closely spaced parallel waveguides which couple power across the Multiple-Quantum-Well (MQW) layer. Due to the large nonlinearity exhibited by the MQW, the light's output characteristics and thus device properties depend on the input power level.

1.2 The Working Materials

There are several reasons for choosing LiNbO$_3$ as the working substrate material and these are listed below:

1) Strong electro-optic effect

2) Large anisotropy

3) Ease of making waveguides

4) Inert and stable material

5) Single crystals available

6) One surface of optical grade finish

7) Well documented substrate.

The GaAs work is completely theoretical since the required MQW structures where not available. This material is favoured as the substrate since the structure can be built using molecular beam epitaxy and it is compatible with existing GaAs based sources and detectors.

1.3 The Future

Integrated-optic waveguides provide the basis for a large variety of promising devices for lightwave communications and optical signal processing applications. The waveguide geometries examined in this thesis will form the basis of larger more complex systems. The advantage of using light instead of electrons to carry the information are numerous and have caused a mushrooming of applications for the technology. Integrated-optics will enable the integration of sources, detectors and other components, with the waveguides on a single substrate, increasing the density of components. Utilizing integration techniques similarly to those of the semiconductor industry promises to provide devices at mass production costs and in high yields. The formation of electro-optic components, which can act directly on the guided light without the need of opto-electronic conversions before and after processing of the signal, appear promising for future system applications. In the case of the MQW designs, controlling electrical interfaces can be bypassed altogether and the processing information encoded in the light beam.

CHAPTER 2. THE SUBSTRATE (LiNbO$_3$)

2.1 Introduction

An homogeneous transparent media can be characterized optically by a di-
electric constant, ϵ, or a refractive index, $n = \sqrt{\frac{\epsilon}{\epsilon_o}}$. Among the solutions of
Maxwell's equations are the monochromatic plane waves of homogeneous type. The
characteristic of the media is that these waves propagate with a definite velocity
c/n and without diminution of amplitude or change of polarization no matter what
the polarization and direction of propagation may be. These media are known as
singly refracting[1] and a good example is glass.

Most crystals and many liquids do not have the simple properties of singly
refracting media but are grouped based on their more complex properties into the
doubly refracting[1] class (two indices of refraction). The media in this class can be
subdivided according to whether they are or are not optically active and according
to whether they are isotropic or anisotropic.

2.2 Dielectric Tensor and Index Ellipsoid

LiNbO$_3$ is a member of the doubly refracting class. It is a nonactive media
which implies that the two polarizations for any given direction of propagation are
linear and at right angles to each other. To be doubly refracting and nonactive,
the substrate must be anisotropic, which means, among other things, that the
differences in indices are not the same for all directions of propagation. Furthermore,
the substrate has a unique axis for which the propagation of a wave polarized along

6

either transverse axis sees no difference in the indices and is known as the optical axis.

In Maxwell's theory, a dielectric medium is characterized by the relation between **E** and **D** when the excitation is monochromatic with any given frequency. For transparent singly refracting media, the relation is[2]:

$$\mathbf{D} = \epsilon \mathbf{E} \tag{2.1}$$

with ϵ as a scalar. To treat doubly refracting media, ϵ is replaced by a tensor of rank 3 and the relation between **E** and **D**, for an arbitrary set of cartesian axes fixed in the substrate, takes the form[3]:

$$\begin{pmatrix} D_x \\ D_y \\ D_z \end{pmatrix} = \begin{pmatrix} \epsilon_{xx} & \epsilon_{xy} & \epsilon_{xz} \\ \epsilon_{yx} & \epsilon_{yy} & \epsilon_{yz} \\ \epsilon_{zx} & \epsilon_{zy} & \epsilon_{zz} \end{pmatrix} \begin{pmatrix} E_x \\ E_y \\ E_z \end{pmatrix} \tag{2.2}$$

For LiNbO$_3$, which is nonactive, all the ϵ_{ij}'s are real and form a symmetric matrix. The values of the ϵ_{ij}'s depend only on the orientation of the cartesian axes relative to the crystal. If the axes are rotated, the individual elements of the tensor (ϵ_{ij}) change. There is a theorem on real symmetric matrices[4] which allows the axes to be chosen so that the dielectric tensor takes the form of a diagonal matrix:

$$\epsilon_d = \begin{pmatrix} \epsilon_x & 0 & 0 \\ 0 & \epsilon_y & 0 \\ 0 & 0 & \epsilon_z \end{pmatrix} \tag{2.3}$$

These particular axes are called the principal axes of the medium, and ϵ_x, ϵ_y and ϵ_z are called the principal dielectric constants. The anisotropy of the substrate can be thought of as originating through the structure of the crystal. In a crystal, the constituent atoms are in intimate contact and experience short-range forces, bonding the lattice together and affecting internal motion in the atoms. The electrons which give rise to the optical properties are elastically bound to positions of equilibrium, and unless the atoms neighbouring a given one are in an especially symmetrical arrangement, the binding of a given atom is anisotropic.
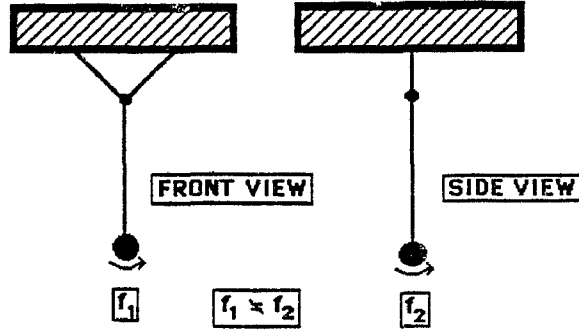
Figure 2.1: Mechanical illustration of anisotropy.

A mechanical illustration of anisotropic binding, in two dimensions, is the pendulum bob suspended by strings in the arrangement shown in figure 2.1. The yoke at the top gives rise to different natural frequencies for oscillation perpendicular and in the plane of the page. In the general orientation the rotation tensor, using the Euler angles[5], is of the form:

$$T = \begin{pmatrix} cs\phi cs\psi - sn\phi cs\theta sn\psi & -cs\phi sn\psi - sn\phi cs\theta cs\psi & sn\psi sn\theta \\ sn\phi cs\psi + cs\phi cs\theta sn\psi & -cs\phi sn\psi + cs\phi cs\theta cs\psi & -cs\phi sn\theta \\ sn\theta sn\psi & cs\theta cs\psi & cs\theta \end{pmatrix} \qquad (2.4)$$

where cs and sn represent cos and sin respectively, and can be used to define the elements of the dielectric tensor through the relation:

$$\epsilon = T^{-1}\epsilon_d T \qquad (2.5)$$

In this relation, T^{-1} represents the inverse of the rotation matrix and ϵ_d represents the diagonal dielectric tensor of the principal axis system.

The principal indices of refraction are defined by[6]:

$$n_x = \sqrt{\frac{\epsilon_x}{\epsilon_o}}$$

$$n_y = \sqrt{\frac{\epsilon_y}{\epsilon_o}} \qquad (2.6)$$

$$n_z = \sqrt{\frac{\epsilon_z}{\epsilon_o}}$$

LiNbO$_3$ being a uniaxial crystal, implies equality for two of the principal indices. For convenience, the optic axis is oriented along the z axis when the crystal has only one such axis, thus:

$$n_x = n_y = n_o \qquad (2.7)$$

and

$$n_z = n_e \qquad (2.8)$$

which are invarient under rotation about the z axis, The subscripts (o) and (e) indicate the ordinary and extraordinary indices of refraction. Their importance and differences will become clearer when discussing optical waveguides.

A convenient method of expressing the above mentioned properties is to utilize an index ellipsoid[7]. In an arbitrary cartesian reference system, it is expressed as:

$$\sum_{i,j=1}^{3} \frac{1}{n_i n_j} x_i x_j = 1 \qquad (2.9)$$

The index ellipsoid for LiNbO$_3$ takes a much simpler form in the principal axis system:

$$(\frac{x}{n_o})^2 + (\frac{y}{n_o})^2 + (\frac{z}{n_e})^2 = 1 \qquad (2.10)$$

A graphical representation of the index ellipsoid for LiNbO$_3$ in the principal axis system is shown in figure 2.2. The values of the ordinary and extraordinary indices of refraction at 0.6328 μm wavelength are taken as[9]:

$$n_o = 2.286 \qquad and \qquad n_e = 2.202 \qquad (2.11)$$

This method of describing the crystal is extremely useful when discussing the propagation of light in the waveguides and the electro-optic effects.
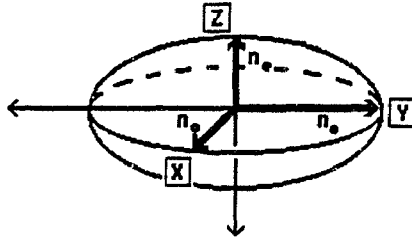
Figure 2.2: Index ellipsoid for LiNbO$_3$.

2.3 Electro-Optic Effect

When an electric field is applied across the crystal, the distribution of electrons within it is distorted, changing the polarizability of the material and hence its refractive index. It is convenient to consider the change in $\frac{1}{n_i^2}$ (i = o,e) with the application of a field since in the principal axis system the index ellipsoid (2.9) is given in terms of $\frac{1}{n_i^2}$. The new inverse index squared when the field is applied $(\frac{1}{n_{i,E}^2})$ can be written as[9]:

$$\frac{1}{n_{i,E}^2} = \frac{1}{n_i^2} + rE + RE^2 \qquad (2.12)$$

where r and R are the linear (or Pockel's, who first studied it in 1893) and quadratic (or Kerr, who discovered it in 1875) electro-optic coefficients, respectively. The coefficients in (2.12) are those of the primary effect which are independent of crystal strain. For LiNbO$_3$, the R coefficients are small compared to the r coefficients and are therefore neglected for small E. The general index ellipsoid of (2.9) with the Pockel's effect included takes the form:

$$\sum_{i,j,k=1}^{3} (\frac{1}{n_i n_j} + r_{ijk}E_k)x_i x_j = 1 \qquad (2.13)$$

The dielectric tensor (2.5) being symmetric enables the i,j indices to be interchanged allowing a contracted notation to be introduced[10].

$$1 = (11) \qquad\qquad 4 = (23) = (32)$$

$$2 = (22) \qquad\qquad 5 = (13) = (31) \qquad (2.14)$$

$$3 = (33) \qquad\qquad 6 = (12) = (21)$$

Using this contracted notation, the r coefficients can be expressed in a 6 X 3 matrix:

$$r = \begin{pmatrix} r_{11} & r_{12} & r_{13} \\ r_{21} & r_{22} & r_{23} \\ r_{31} & r_{32} & r_{33} \\ r_{41} & r_{42} & r_{43} \\ r_{51} & r_{52} & r_{53} \\ r_{61} & r_{62} & r_{63} \end{pmatrix} \qquad (2.15)$$

The expansion of the index ellipsoid with the contracted notation becomes:

$$(1/n_x^2 + r_{1k}E_k)x^2 + (1/n_y^2 + r_{2k}E_k)y^2 + (1/n_z^2 + r_{3k}E_k)z^2$$

$$+ 2r_{4k}E_k xy + 2r_{5k}E_k xz + 2r_{6k}E_k yz = 1 \qquad (2.16)$$

where E_k (k = 1,2,3) is a component of the applied electric field. In general, there are 18 r_{ij} coefficients to take into account when considering the electro-optic effect. Fortunately, the symmetry of the crystal introduces a number of zero elements and relations among the remaining elements. This results because the electric field is a vector quantity, not a scalar quantity, and thus direction is important. For example, if a crystal contains a mirror plane, inverting the crystal with respect to a fixed electric field should have no effect since the structure presented to the field remains unchanged. Therefore several coefficients must be zero in the matrix in order to leave the crystal invariant under this operation. Other symmetry operations can bring out relations amongst the remaining nonzero coefficients. This gives the form of the r matrix but the magnitude of the non zero elements must be measured experimentally. $LiNbO_3$ is a rhombohedral[9] crystal with point group symmetry 3m

below $1200°C^2$. This symmetry provides the r matix of the form:

$$r = \begin{pmatrix} 0 & -r_{22} & -r_{13} \\ 0 & r_{22} & r_{13} \\ 0 & 0 & r_{33} \\ 0 & r_{51} & 0 \\ -r_{51} & 0 & 0 \\ -r_{22} & 0 & 0 \end{pmatrix} \qquad (2.17)$$

The values of the nonzero elements of the electro-optic tensor which determine the strength of the electro-optic effect for $\lambda = 0.6328$ $\mu m^{8,9}$ are:

$$r_{22} = 3.4 X 10^{-12} m/V$$

$$r_{13} = 8.6 X 10^{-12} m/V \qquad (2.18)$$

$$r_{51} = 28 X 10^{-12} m/V$$

$$r_{33} = 30.8 X 10^{-12} m/V$$

The complete expanded index ellipsoid (2.16) for LiNbO$_3$ takes the following form when the zero terms of r matrix are excluded:

$$(1/n_x^2 - r_{22}E_2 + r_{13}E_3)x^2 + (1/n_y^2 + r_{22}E_2 + r_{13}E_3)y^2 +$$

$$(1/n_z^2 + r_{33}E_3)z^2 + r_{51}E_1(yz + xz) - r_{22}E_1 xy = 1 \qquad (2.19)$$

The effect of the applied electric field in the first three terms is to change the length of the principal axis and the corresponding index of refraction. For example, consider the change in the index of refraction which corresponds to the x axis, then:

$$\frac{1}{n_x^2} \Rightarrow \frac{1}{n_x^2} - r_{22}E_2 + r_{13}E_3 \qquad (2.20)$$

Thus, depending on the relative sizes of $r_{22}E_2$ and $r_{13}E_3$, the new index of refraction can be larger or smaller than the non applied field value.

The remaining terms in (2.19) rotate the ellipsoid with respect to the fixed coordinate system. For practical applications, it is desirable to orient the electric

field such that the terms in the index ellipsoid with r_{51} and r_{33} are the largest. Consider the term containing r_{51} first. It has the effect of rotating the axis, and since the natural birefringence is appreciable, this angle is small[9]. The lengths of the axes (and hence the indices) are changed by a small negligible amount. The r_{33} coefficient on the other hand can cause a substantial change in the length of the z principal index. If we write the new index as $n_z + \Delta n_z$ then:

$$\frac{1}{(n_z + \Delta n_z)^2} = \frac{1}{n_z^2} + r_{33}E_z \qquad (2.21)$$

For changes which are small in comparison to n_z (but not negligible) the expression for the change in length of n_z is:

$$\Delta n_z \approx \frac{-1}{2}r_{33}n_z^3 E_3 \qquad (2.22)$$

For a field of 1 volt/μm this produces a change of 1.5×10^{-4}.

It has been shown in this chapter that the complicated features of the LiNbO$_3$ substrate can be discussed using the simple concept of the index ellipsoid. Furthermore, the electro-optic properties can be interpreted by noting the changes caused to this ellipsoid. As shown above, the index change is quite small when compared to the bulk indices of the substrate but is large enough to make feasible a multitude of devices. Several such devices are the subject of this thesis. By orienting the waveguides along one of the principal axes of the crystal, the analysis of the optical properties can be reduced to that of isotropic waveguides which are discussed in the next chapter.

CHAPTER 3. THEORY OF DIELECTRIC WAVEGUIDES

3.1 Wave Equation

Dielectric waveguides are the structures that are used to confine and guide light in the devices and circuits of integrated-optics. A well-known dielectric waveguide is, of course, the optical fibre which usually has a circular cross-section. In contrast, the guides of interest to integrated-optics are usually planar, such as films and strips, or rectangular, such as channels. The aim of this chapter is to provide a compact theoretical framework of sufficient rigour and generality that it can be used as a basis for discussion in later chapters. First the optical properties of the step index slab waveguide structure are discussed. This structure is simple to analyze mathematically and brings out many important features relevant to the more complicated waveguide geometries. Throughout this chapter, guided light is coherent and monochromatic and the waveguides consist of dielectric media that are lossles and isotropic. The problem of including losses and anisotropy is left until chapters 6, 7, 8 and 9, where the waveguides and devices are discussed.

A convenient starting point in developing the wave equation, which governs the propagation of light in an isotropic dielectric structure, is Maxwell's equations of the form:

$$\nabla \cdot \mathbf{E} = \frac{\rho}{\epsilon} \tag{3.1}$$

$$\nabla \cdot \mathbf{B} = 0 \tag{3.2}$$

$$\nabla X \mathbf{E} + \frac{\partial \mathbf{B}}{\partial t} = 0 \tag{3.3}$$

$$\nabla X \mathbf{B} - \epsilon_r / c^2 \frac{\partial \mathbf{E}}{\partial t} = \mu_o \mathbf{J}_f \tag{3.4}$$

where $\mathbf{J}_f$ is the current density and ρ is the charge density.

The wave equation for electric fields can be obtained by taking the curl of equation (3.3), using a vector identity[11] and then using equations (3.1) and (3.4). The final result is:

$$\nabla^2\mathbf{E} - \epsilon\mu_0\frac{\partial^2\mathbf{E}}{\partial t^2} = \nabla(\frac{\rho}{\epsilon}) + \mu_o\frac{\partial\mathbf{J}_f}{\partial t} \tag{3.5}$$

Similarly the wave equation for the magnetic field can be obtained starting from equation (3.4), which results in:

$$\nabla^2\mathbf{B} - \epsilon\mu_o\frac{\partial^2\mathbf{B}}{\partial t^2} = -\mu_o\nabla X J_f \tag{3.6}$$

The substrates of interest do not contain any free charges (ρ and $\mathbf{J}_f = 0$) and as a result the wave equations for the $\mathbf{E}$ and $\mathbf{H}$ fields of the dielectric structure reduce to:

$$\nabla^2\mathbf{E} - \epsilon\mu_o\frac{\partial^2\mathbf{E}}{\partial t^2} = 0 \tag{3.7}$$

$$\nabla^2\mathbf{H} - \epsilon\mu_o\frac{\partial^2\mathbf{H}}{\partial t^2} = 0 \tag{3.8}$$

The waveguiding properties of the dielectric structure are expressed through variations in ϵ as will be shown in the remainder of the chapter. The media are assumed to be isotropic, which implies that ϵ is a diagonal tensor with equal elements. The dielectric constant is related to the index of refraction through the relation $n^2(x,y) = \frac{\epsilon(x,y)}{\epsilon_o}$ This expression is similar to that given in chapter 2, but now the spatial variations due to the waveguide structure are emphasized.

Throughout this analysis the time variation is taken as $e^{-i\omega t}$ and the waves propagate in the z direction with propagation constant β. It is the propagation constant, β, which determines to a larger extent the properties of guided waves. The solutions of the wave equation can then be written as:

$$\mathbf{E} = \psi(x,y)e^{-i(\omega t - \beta z)} \tag{3.9}$$

$$\mathbf{H} = \xi(x,y)e^{-i(\omega t - \beta z)} \tag{3.10}$$

The equation that governs the transverse behaviour of the fields can then be written as:

$$\left(\nabla_t^2 + (\tfrac{\omega}{c})^2(n^2(x,y) - \beta^2) \right) \begin{pmatrix} \psi(x,y) \\ \xi(x,y) \end{pmatrix} = 0 \tag{3.11}$$

where

$$\nabla_t^2 = \nabla^2 - \frac{\partial^2}{\partial z^2} \tag{3.12}$$

A general requirement for a guide for electromagnetic radiation is that the energy flows along the guiding structure not perpendicular to it. This means that the fields will be appreciable only in the immediate vicinity of the guiding structure. Generally speaking, a beam propagating in a transversely inhomogeneous medium tends to bend towards the region of higher index of refraction. Thus the high index of refraction in the guiding region has an effect similar to that of a converging lens. Under appropriate conditions this converging effect, due to an higher core index, may exactly cancel out the spreading due to diffraction. When this happens a guided mode is supported by the dielectric structure and mathematically it can be represented by a mode index, m or n.

The waveguide modes supported by an arbitrary dielectric structure have an important and useful orthogonality property. For TE modes it is expressed as:

$$\frac{\frac{\beta_m}{k_o}}{2\sqrt{\frac{\mu_o}{\epsilon_o}}} \int \int \mathbf{E}_m \mathbf{E}_n^* da = \delta_{mn} \tag{3.13}$$

while for TM modes it becomes:

$$\frac{\frac{\mu_o \beta_m}{k_o}}{2\sqrt{\frac{\mu_o}{\epsilon_o}}} \int \int \mathbf{H}_m \frac{1}{\epsilon} \mathbf{H}_n^* da = \delta_{mn} \tag{3.14}$$

These expression can be used to normalize the power in the waveguide and are made use of in later chapters.
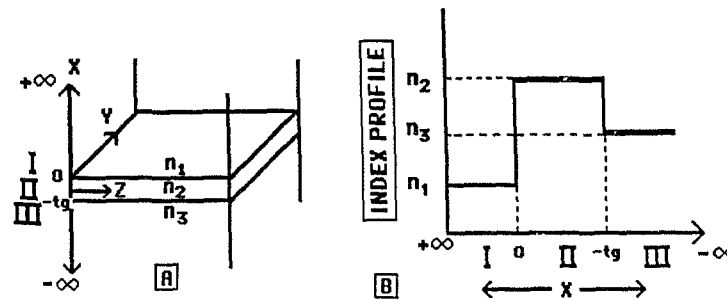
Figure 3.1: A - Structure of the dielectric slab waveguide, B - Index of refraction profile for the slab.

3.2 One Dimensional Step Index Slab Waveguide

The dielectric slab waveguide structure considered is shown in figure 3.1 A. It consist of three layers in contact with the light confining layers, n_1 and n_3, which are assumed to extend to infinity in the $+ x$ and $- x$ directions respectively. The central layer has an index of refraction, n_2, and is in contact with the upper and lower layers at $x = 0$ and $x = - t_g$. The index of refraction profile for the structure is shown in figure 3.1 B. Typical differences in the indices of refraction between the guiding and cover layers range from 10^{-3} to 10^{-1}, and the guiding layer has a typical thickness of 1 to 10 μm.

In the step index slab waveguide structure, equation (3.11) holds separately in each region. Thus the wave equation is solved in each region independently, then the tangential components of the fields are matched at the interfaces making use of one set of boundary conditions. Another important boundary condition is that the field amplitudes are zero at $x = \pm\infty$. The field components in the confining layer must have this behaviour in order that no energy flows perpendicular to the interfaces. The z axis propagation constant (β) must be the same throughout the

guiding structure in order to satisfy the boundary conditions at all points on the interfaces of the homogeneous media.

The basic problem is that of finding the solution to the eigenvalue equation (3.11), subject to the above mentioned boundary conditions. In general there are an infinite number of eigenvalues, β, corresponding to an infinite number of modes. However, only a finite number of these modes are confined near the central higher index layer and have a propagation constant β between $k_o n_3 < \beta < k_o n_2$ for $n_3 > n_1$. For the structure of the wave equation reduces to:

$$\left(\frac{\partial^2}{\partial x^2} + (k_o n_i^2 - \beta^2) \right) \begin{pmatrix} \psi \\ \xi \end{pmatrix} = 0 \tag{3.15}$$

where i corresponds to regions I, II and III, respectively. The guide can in general support a finite number of transverse electric (TE) modes with field components E_y, H_x, H_z, and transverse magnetic (TM) modes with components H_y, E_x, E_z.

3.2.1 TE modes

The electric and magnetic field component for the TE modes can be taken as:

$$E_y(x, y, z, t) = \psi_y(x) e^{-i(\omega t - \beta z)} \tag{3.16}$$

$$H_x(x, y, z, t) = \frac{-i}{\omega \mu_o} \frac{\partial E_y}{\partial z} \tag{3.17}$$

$$H_z(x, y, z, t) = \frac{i}{\omega \mu_o} \frac{\partial E_y}{\partial x} \tag{3.18}$$

where the functional form of the TE modes in the three regions is expressed as:

$$\psi_y(x) = A e^{(-qx)} \qquad\qquad 0 < x < \infty \tag{3.19}$$

$$\psi_y(x) = B\cos(hx) + C\sin(hx) \qquad -t_g < x < 0 \tag{3.20}$$

$$\psi_y(x) = D e^{p(x + t_g)} \qquad\qquad -\infty < x < -t_g \tag{3.21}$$

and

$$h = \sqrt{n_2^2 k_o^2 - \beta^2} \qquad (3.22)$$

$$q = \sqrt{\beta^2 - n_1^2 k_o^2} \qquad (3.23)$$

$$p = \sqrt{\beta^2 - n_3^2 k_o^2} \qquad (3.24)$$

and

$$k_c = \frac{\omega}{c} \qquad (3.25)$$

The constants q and p are the exponential decay constants in regions I and III respectively, and h is the transverse propagation constant in region II.

The acceptable solutions of ψ_y and $\xi_z = \frac{i}{\mu_o \omega} \frac{\gamma \psi_y}{\gamma x}$ should be continuous at both $x = 0$ and $x = -t_g$ interfaces. The continuity of ξ_y enables the following relation to be obtained amongst the coefficients.

$$B = A \qquad (3.26)$$

$$C = -q/hA \qquad (3.27)$$

$$D = (cos(ht_g) + q/hsin(ht_g))A \qquad (3.28)$$

The undetermined constant A is arbitrary and is usually defined so that the ξ_y field corresponds to a power flow of 1 W per unit width in the y direction in the mode. Making use of the orthogonality condition (3.13), the normalization condition can be written as:

$$\frac{\frac{\beta_m}{k_o}}{2\sqrt{\frac{\mu_o}{\epsilon_o}}} \int_{-\infty}^{\infty} |\psi_y^m(x)|^2 dx = 1 \qquad (3.29)$$

where m corresponds to the mode order. The continuity requirement of $\frac{\partial \psi_y}{\partial x}$ at $x = -t_g$ gives the mode condition expression, which implies that the propagation constant satisfies the following eigenvalue equation:

$$tan(ht_g) = \frac{(p+q)}{h(1 - \frac{(pq)}{h^2})} \qquad (3.30)$$

Given a set of indices, n_i, and the waveguide thickness, equation (3.29) yields an infinite number of β values for a given wavelength. The number of solutions, β_m, between $\max(n_1:n_3)$ and n_2 indicates the number of guided modes that the structure can support.

For TE modes the electric field component is polarized along the y axis , thus these modes can be excited by an incident wave linearly polarized with the electric field also directed along the y axis.

3.2.2 TM modes

The derivation for TM modes follows similarly to that for TE modes. The field components are:

$$H_y(x,y,z,t) = \xi_y(x)e^{-i(\omega t - \beta z)} \tag{3.31}$$

$$E_x(x,y,z,t) = \frac{\beta}{\omega\epsilon}\xi_y(x)e^{-i(\omega t - \beta z)} \tag{3.32}$$

$$E_z(x,y,z,t) = \frac{-i}{\omega\epsilon}\frac{\partial \xi_y}{\partial x}e^{-i(\omega t - \beta z)} \tag{3.33}$$

The mode function $\xi_y(x)$, with the boundary conditions satisfied, is expressed as:

$$\xi_y(x) = \frac{-A'h}{q'}e^{qx} \qquad \infty \geq x \geq 0 \tag{3.34}$$

$$\xi_y(x) = A'(\frac{-h}{q'}cos(hx) + sin(hx)) \qquad -t_g \leq x \leq 0 \tag{3.35}$$

$$\xi_y(x) = -A'(\frac{h}{q'}cos(ht_g) + sin(ht_g))e^{p(x+t_g)} \qquad -\infty \leq x \leq -t_g \tag{3.36}$$

where A' is normalized to a power flow of 1 W per unit length along the y axis.

The continuity of H_y and E_z at the interfaces leads to the eigenvalue equation for the β's expressed as:

$$tan(ht_g) = \frac{(p' + q')}{h(1 - \frac{(p'q')}{h^2})} \tag{3.37}$$

$$p' = \frac{n_2^2}{n_3^2}p \tag{3.38}$$

$$q' = \frac{n_2^2}{n_1^2}q \tag{3.39}$$

The number of allowed values of β indicates the number of possible guided modes in the structure. Since the electric field component is polarized along the x axis (neglecting the tilt towards the z axis due to the presence of the E_z component), the TM modes can be excited with an incident wave having the electric field polarized along the x axis.

3.2.3 Discussion

A guided mode can easily be visualized using the classical ray approach and Snell's law as shown in figure 3.2. The existence of the eigenvalue spectrum of β's can be interpreted as follows. If a ray propagates down the structure and suffers total internal reflection at the upper and lower interfaces, it returns to a position further down the guide, which is at the same distance from the interfaces and propagating with the same angle. In the figure, two of these points are marked by the dots on the core ray. The mode will be guided provided the phases at these two points match exactly. Not all propagating angles will satisfy this condition; the number depends on the waveguide structure in much the same way as the allowed β's depend on the waveguide parameters. If the walls were perfectly reflecting and the medium lossles, we would expect to have an infinite number of ray angles, θ, giving guided modes (θ allowed approaches a continuum near 90 degrees). In our structure of three dielectric layers, a ray that is incident at an angle greater than the critical angle (determined by setting $n_2/n_3 \sin(\theta_c) = 1$) will not suffer total internal reflection but will refract into the adjacent area and radiate away. For this ray, energy propagates perpendicular to the guiding structure and this mode does not
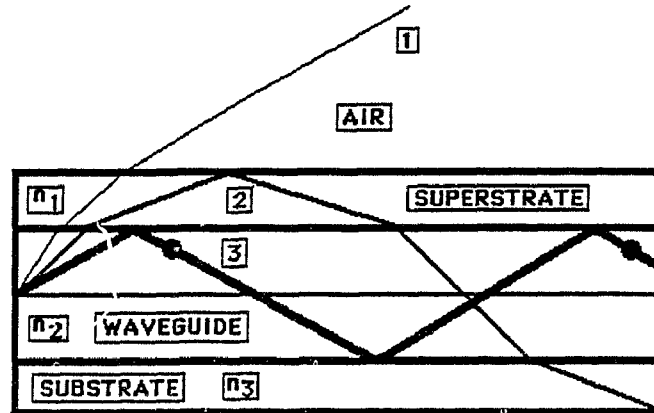
Figure 3.2: Ray picture of guided modes, 1. Air mode, 2. Substrate-superstrate mode, 3. Guided mode.

constitute a guided mode. This sets an upper boundary on the possible ray angles if they are to remain guided. Therefore, only a finite number of rays will interfere constructively in the waveguide structure and thus a finite number of guided modes are possible. This is similar to the finite number of eigenvalues β that are allowed as solutions to the eigenvalue equations (3.30) and (3.37).

The wave equation approach and the ray approach provide two methods of treating optical waveguides. When the waveguides are substantialy larger than the wavelength each approach provides results in good agreement. The propagation constants in this case are defined as the z component of the ray's propagation vector as shown in figure 3.3. This definition is also employed when the wavelength is comparable to the guide width, but care should be taken to analyze the problem using wave theory not ray theory. In many discussions it may be simpler to interpret a mode in the ray approximation, which is simpler to visualize.

The solutions for (3.30) and (3.37) for TE and TM modes, respectively, for a particular index of refraction profile are shown in figure 3.4 for the case of GaAs. The y axis represents the normalized propagation constant β_m/k_o (effective index), which can range from $\max(n_1,n_3)$ to n_2. The x axis is the normalized thickness of the guide t_g given in units of λ. Important waveguide information can be deduced
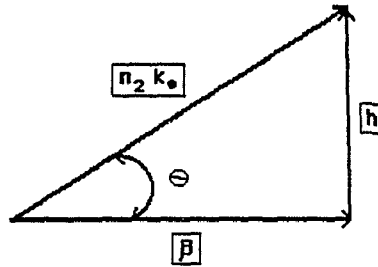
Figure 3.3: Ray interpretation of the propagation constant.

from this figure.

Consider the situation when t_g/λ is allowed to increase. This corresponds to either increasing the physical width of the guide or decreasing the wavelength. This has the effect of increasing the optical width of the waveguide and can increase the number of guided modes. Also, for this increase the value of the normalized propagation constant gets larger and approaches the waveguide layer index value n_2. In this case, the modes are becoming more highly confined in the guiding region and the amplitude of the field at the waveguide-confining layer interface is reduced.

On the other hand, when the optical width of the waveguide is decreased, a mode which was initially guided in the structure may now be cut off and the eigenvalue β will not fall in the allowed range of guided values. Modes which are still guided will extend further into the confining layers with a larger field amplitude at the waveguide-confining layer interface. If the optical width is decreased even further, a point may be reached at which no guided solutions to the eigenvalue equation are possible. When this occurs the waveguide cannot support any guided modes and is totally cut off.
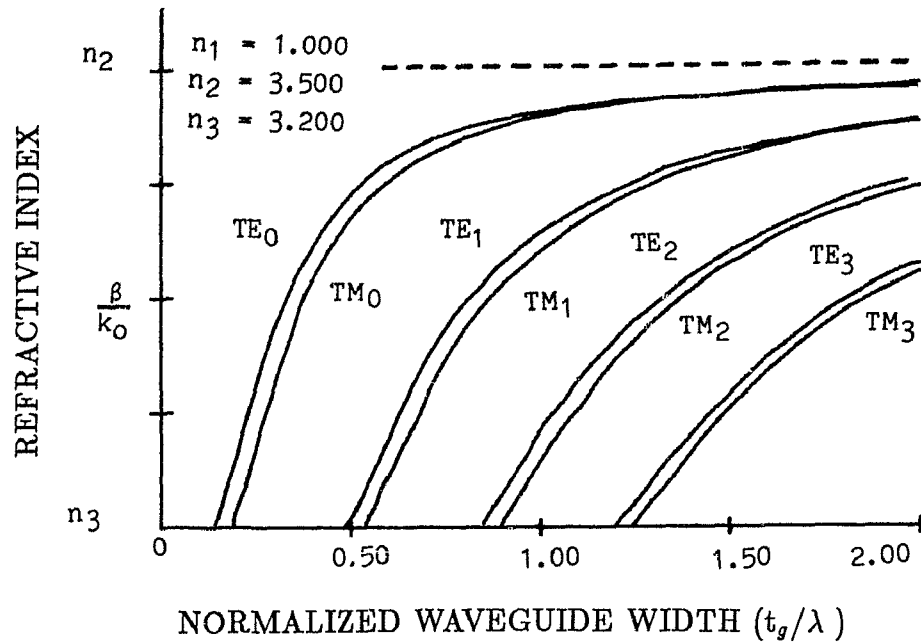
Figure 3.4: Effective mode index versus normalized waveguide width for the four lowest order TE and TM modes.

3.2.4 Computer Generated Mode Profiles

A computer program has been written which solves the slab waveguide problem by assuming a series representation for the electric field profile. Then, through a recursion relation generated by the wave equation and the use of the boundary conditions, the coefficients of the series have been obtained. The index of refraction profiles, electric field profiles and irradiance patterns generated for the two lowest order modes of the symmetrical and asymmetrical waveguide structures, are reproduced in figures 3.5 to 3.8. The lowest order mode contains only one maximum in the centre of the guiding layer for the symmetrical waveguide and is slightly offset towards the higher confining index for the asymmetrical waveguide. Since there are no minima in the waveguide region, the order 0 is given for this mode (m = 0). The second order mode is labeled m = 1, since there is one minimum in the guiding region. As a result, two maxima are observed in the guiding region with the minimum between them. In the irradiance pattern there is no confinement along
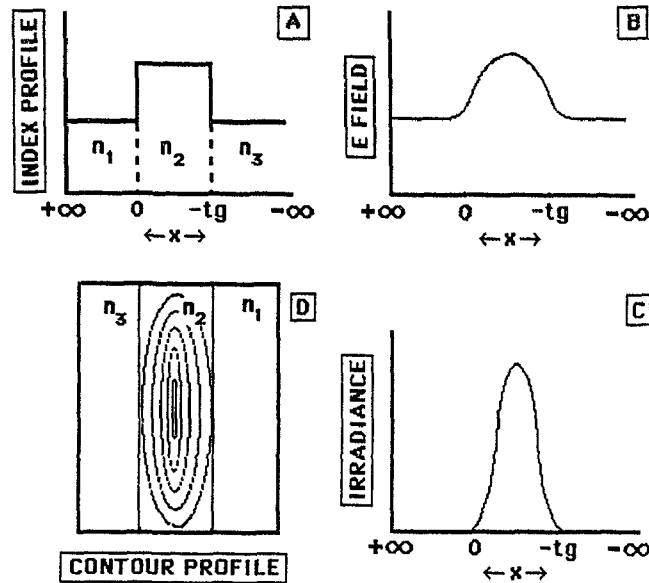
Figure 3.5: Lowest order TE mode in a symmetrical slab waveguide, A - Index of refraction profile, B - Electric field profile, C - Irradiance pattern, D - Contour profile.

the y axis and the width of the profile is dictated by the scattered light and exciting beam divergence.

3.3 One Dimensional Graded Index Slab Waveguide

The grading of the index of refraction profile of region II, from a maximum of n_2 (see figure 3.10 for example) at the I-II interface to a minimum of n_3 at the II-III interface, is the next degree of complexity to be added to the waveguide analysis. For this structure the wave equation (3.15) is still valid, provided the index n_2 is adjusted to reflect the graded nature of the guiding region. In most situations the graded index of refraction can be fitted to match an analytic function, after which more elegant techniques[12-15] can be employed to obtain the mode functional form and propagation constants. When the change in the index of refraction is slow compared to the wavelength, or many modes can be supported by the structure, approximate solutions using the WKB technique[16-18], for example, can be employed
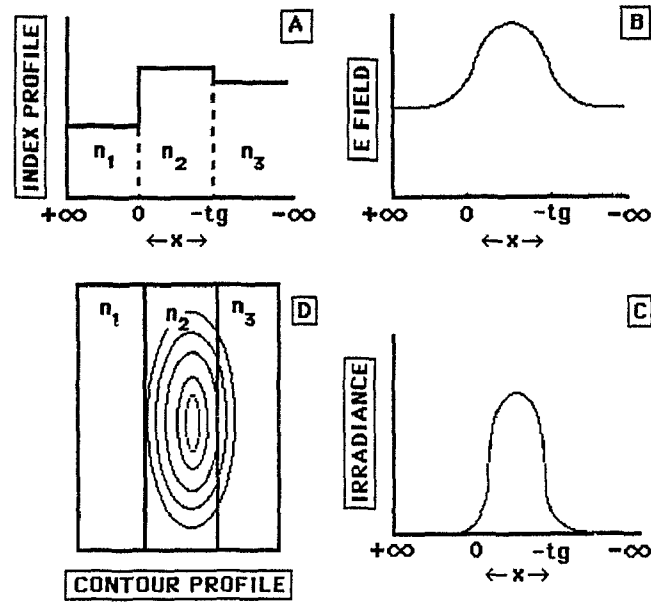
Figure 3.6: Lowest order TE mode in an asymmetrical slab waveguide, A - Index of refraction profile, B - Electric field profile, C - Irradiance pattern, D - Contour profile.
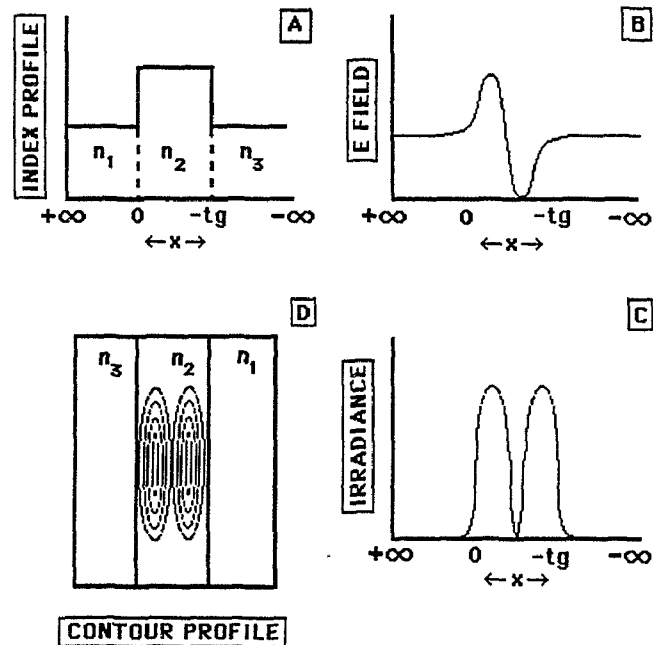
Figure 3.7: Second order TE mode in a symmetrical slab waveguide, A - Index of refraction profile, B - Electric field profile, C - Irradiance pattern, D - Contour profile.
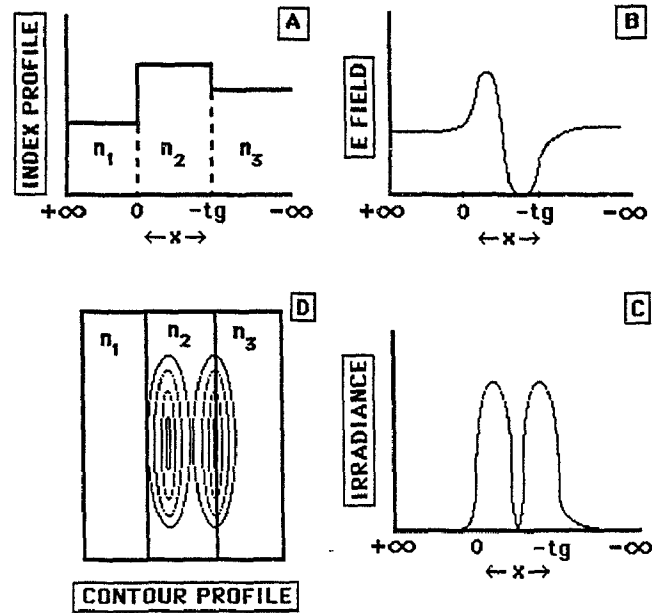
Figure 3.8: Second order TE mode in an asymmetrical slab waveguide, A - Index of refraction profile, B - Electric field profile, C - Irradiance pattern, D - Contour profile.

to provide valuable mode information.

The modal behaviour of the graded index guide can be understood in terms of the ray picture of figure 3.9. The ray will no longer propagate in a straight line in region II, but will suffer distributive refraction due to the graded profile and trace out a curved path. The total phase change along this path, between two points separated by one period, is given by three terms, ϕ_p, ϕ_1 and ϕ_2. Consider for instance, the ray labeled 2 in the diagram, the phase change along the curved path can be expressed as:

$$\phi_p = 2k_o \int_{x_{t1}}^{x_{t2}} \sqrt{n_x^2 - n_{eff}^2}\, dx \tag{3.40}$$

At the point labeled x_{t1} the ray suffers total internal reflection and an associated phase change (ϕ_1) results:
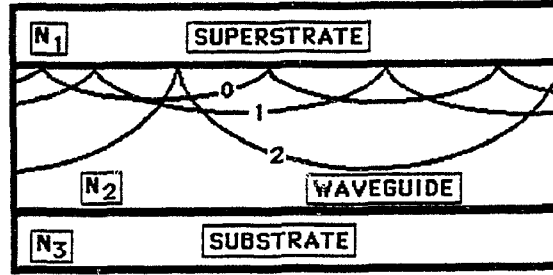
Figure 3.9: Modal behaviour in graded index waveguide, 0 - Lowest order mode, 1 - Second order mode, 2 -Third order mode.

$$\phi_1 = -2tan^{-1}(\frac{\gamma\sqrt{n_{eff}^2 - n_1^2}}{\sqrt{n_2^2 - n_{eff}^2}}) \qquad (3.41)$$

where $\gamma = 1$ for TE modes and $\gamma = (\frac{n_2}{n_1})^2$ for TM modes.

At the point labeled x_{t2}, the ray approaches grazing incidence and the index discontinuity approaches zero. The ray turning back upwards can be regarded as a reflection where the phase change is given by the limiting case of an expression similar to ϕ_1, except that the indices n_1 and n_2 are equal. The phase change for this reflection is $-\pi/2$.

The fundamental requirement of a guided mode in the ray picture is that the sum of the phase change along the path is an integral multiple of 2π. This property can be expressed as the dispersion equation[19-22]:

$$2k_o \int_{x_{t1}}^{x_{t2}} \sqrt{n_x^2 - n_{eff}^2}\, dx + \phi_1 + \phi_2 = 2m\pi \qquad (3.42)$$

where m represents the order which differentiates between the various modes. This approximate technique can provide valuable waveguide information on the number of modes, effective indices of each mode, and propagation constants.

To obtain the propagation constant (β) values, the mode order (m) is chosen; then, knowing that β must lie between n_2 and $\max(n_1:n_3)$, a trial value is used to

evaluate (3.42). The right hand side is first calculated. The integral on the left hand side is solved numerically for several trial values of the turning points x_{t1} and x_{t2} (x_{t1} is 0 if the maximum index occurs at the I-II interface). If the R.H.S. does not equal the L.H.S. then another pair of turning points is chosen and the integral is re-evaluated. Once all possible pairs have been tried, and if no match has been observed, another β value is chosen and the integral re-evaluated once again. This process continues in a systematic fashion until all the possible values of β have been tried. If a match between the L.H.S. and R.H.S. is observed at any stage of the calculations, the test value of β is a valid waveguide propagation constant for the mode order (m) chosen. The values of x_{t1} and x_{t2} represent the physical extent of the waveguide for the mode. The values of the electric field beyond the turning points correspond to the evanescent tails. If on the other hand no match was found, then the mode order (m) is not guided by the structure.

The values of β obtained using this numerical technique agree remarkably well with those obtained by solving the wave equation exactly[16]. The advantage of using this technique lies in the little work required to obtain the values of β since a computer program can be used. The allowed values of the propagation constant, β, can be used to obtain approximate functional forms for the electric field profiles[8]. The number of modes can easily be obtained using this technique by setting $\beta = n_3$ and x_{t2} to ∞. The largest integer value of (m) obtained from the dispersion equation represents the highest mode order that can be guided. This is useful when designing a single mode graded index waveguide since several parameters can be chosen.

Figure 3.10 shows an index of refraction profile that contains a graded guiding layer. Also shown in the figure is the intepretation of the effective waveguide width and how it is linked to the normalized propagation constant, β. The discussions for β of the step index slab waveguide are also valid for the graded index slab waveguide, provided the curved nature of the ray's trajectory in the graded layer is
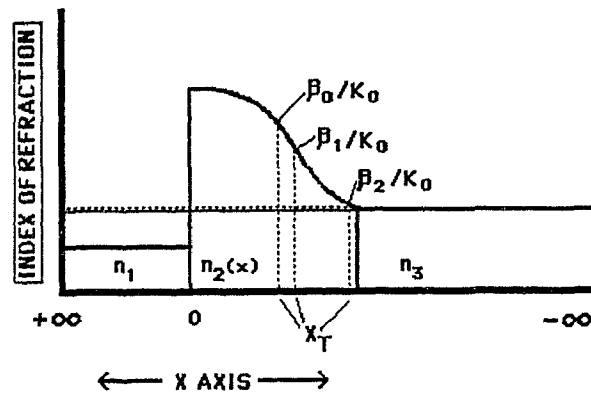
Figure 3.10: Index of refraction profile for graded waveguide. The effective indices and turning points of the guided modes are also shown.

included.

3.4 Two Dimensional Waveguides

If the dielectric structure of figure 3.1 is altered such that the index of refraction is allowed to vary along the y axis also, then light may be confined in two dimensions in the region of higher index of refraction. The wave equation of (3.15) would now have to include the spatial variations along the y axis to be complete. Two possible situations can exist for the index of refraction profile: a step index profile and a graded index profile.

3.4.1 Step Index Profile

The step index channel has not found much practical use in $LiNbO_3$-based integrated-optic waveguides, since the channels obtained are of the graded nature. In many situations, however, it is simpler to approximate the channel as a step

profile in order to obtain a first order approximation to a proposed design, or to facilitate the explanation of experimental observations. The channel waveguide will be of greater use in GaAs based waveguide designs, where channel etching and redeposition of an alternate material can form waveguides with step variations in the index of refraction profile. Semiconductor diode lasers and MQW based devices are good examples of rectangular channel waveguides.

Analysis of the waveguide modes can proceed by many different approaches. A cornerstone paper in 1969 by Marcatili[23] marked perhaps the start of the modern integrated-optic era by analysing the step channel optical waveguide. The analysis proceeds by supposing that the channel can be decomposed into two slab waveguides oriented at 90 degrees to each other, intersecting in the guiding region, a technique now known as the effective index method of analysis. Figure 3.11 A shows a cross-sectional view of the rectangular waveguide structure, while B shows the index of refraction profile.

The shaded region has not been considered and as a result the analysis works well when the modes are far from cut-off, or equivalently when most of the power is confined in the core region. The method used to analyse the step index slab waveguide structure above can be used here, since the decomposition of the wave equation into two independent profiles enables the separation of the variables to be possible in solving the wave equation (3.15). Computer generated profiles, using exact theoretical analysis[24], which agree well with Marcatili's results, are shown in figure 3.12. In A, the near field profile for the lowest order mode (TE_{00}) is plotted as would be observed from the end of the waveguide. There are no minima in the profile along the X or Y axes, thus the enumeration (00) is given to this mode. Comparing this mode profile with that of the lowest order mode in the step index slab waveguide, shows that the light which previously spread out in the y direction is now confined to the channel. In (B), the TE_{11} mode is plotted as would be observed from the end of the waveguide. A single minima along the X and Y axes is
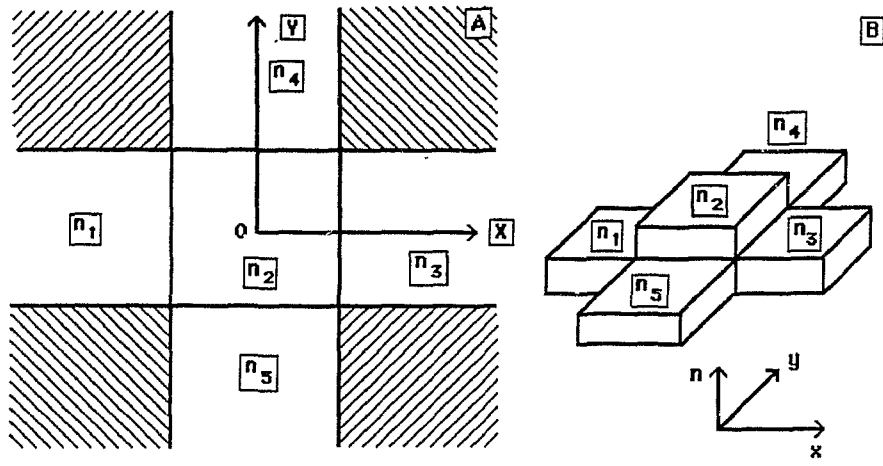
Figure 3.11: A - Cross-sectional view of rectangular waveguide, B - Index of refraction profile.

Figure 3.12: Two modes of the rectangular waveguide A - TE_{00} and B - TE_{11}.
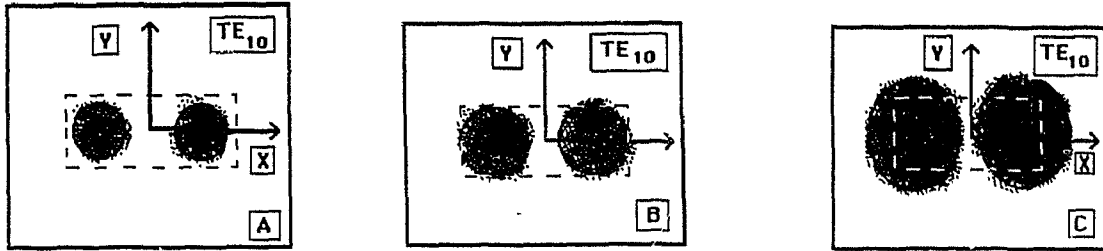
Figure 3.13: Effect of approaching cut off for the TE_{10} mode.

observed, thus the subscript (11) is given to this mode. This results in four bright regions symmetrically located in the guiding region. Notice that at the centre of the waveguide no light is present. The effects of approaching cut-off for the TE_{10} mode are shown through the sequence of figures in 3.13 A, B and C. As cut-off is approached, the field amplitude extends further into the substrate region, a similar result to that discussed when treating the slab waveguide structure.

3.4.2 Graded Index Profile

A graded index channel waveguide is similar to the rectangular channel waveguide, except that the central guiding layer is graded in one or both directions with the maximum of the dielectric structure occurring in the guiding region. The wave equation (3.15) must now be solved with the graded nature of the index of refraction profile included. When the index of refraction profile can be modelled to fit an analytical function, approximate techniques can be used to extract the propagation constants and mode profile information. When the X and Y dependencies of the index of refraction profile can be separated, the effective index method can be employed to simplify the theoretical treatment of the waveguide structure[25].

In most situations, the index of refraction profile cannot be treated simply and one must rely on numerical methods[26-31] to solve the wave equation. In this

research, the two dimensional graded waveguide structure was not solved since all the desired waveguide information could be obtained experimentally.

CHAPTER 4. THE MAKING OF INTEGRATED-OPTIC DEVICES

4.1 Introduction

A typical integrated-optic device is shown in figure 4.1. The waveguide is used to confine the electromagnetic radiation into the channel. This channel can have a width in the order of micrometers and lengths in excess of 3 centimeters. Electrodes are placed in close proximity to the waveguide such that through the electro-optic effect, the guiding properties of the waveguide are altered in such a way as to produce a measurable change to the output light of the channel. This chapter discusses the many steps involved in obtaining a waveguide and electrodes on the crystal.

4.2 The Masks

Integrated-optic devices are commonly fabricated using photolithographic techniques. The devices depend highly on the quality of the mask used which contains a scaled replica of the waveguide or electrode pattern desired. A laser writing technique[32-38] is one method of generating the patterns and has been used to produce the masks required for the major part of this research. The masks are written in a few simple steps, and the designs can be easily altered at any stage of production. The laser writing system shown in figure 4.2 can be divided into three subsystems: beam guiding, sample positioning and computer interfacing.

Beam guiding: A 5 mW He-Cd laser (442 μm wavelength) or a 35 mW Ar$^+$ laser (488 μm wavelength) has sufficient intensity to rapidly expose both positive
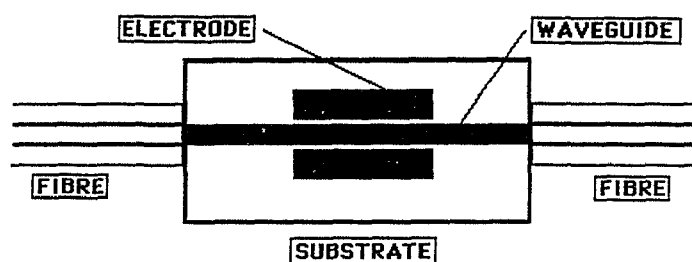
Figure 4.1: Typical integrated-optic device.

and negative photoresists. A shutter placed next to the exit aperture of the laser controls the on off state of the writing beam, while an acousto-optic deflector-modulator controls the laser beam intensity. A single slit allows the beam deflected by the modulator to pass on to the sample, while removing the central beam. A beam expander is used to enlarge the laser beam to several millimeters in diameter, and a front surfaced mirror deflects the beam 90 degrees onto a standard microscope objective lens (10X or 20X) which focuses onto the sample. The combination of objective lens and beam expander can produce a diffraction limited spot in the order of a micron. Back scattered light originating from the sample is separated by a beam splitter from the main light path and observed on a screen. Fine adjustment in the writing beam focus is accomplished by adjusting the height of the lens with respect to the sample and confirmed in the image quality on the screen.

Positioning: A rotational stage, sandwiched between two linear stages, allows for non-cartesian motions of the sample with respect to the fixed laser beam which enables the writing of lines, arcs and circles. Each stage is equipped with a computer controlled D. C. motor which provides 0.1 μm resolution in linear position or 1 second of arc in angular resolution. The backlash in these motors produces a constant deviation of several micrometers in the positioning, depending on the motor speed, and is corrected for by software when writing the masks. The sample, when exposed, is held firmly to the translational stages by a vacuum holder which can easily accommodate square samples up to 5 cm on edge. In this arrangement

LASER

SHUTTER

ACOUSTIC
OPTIC
MODULATOR

SCREEN

INTERFACE
BOARD

SLIT

BEAM SPLITTER

BEAM EXPANDER

MIRROR

COMPUTER IBM

X STAGE
AND
MOTOR

LENS

SAMPLE

HOLDER

Θ STAGE
AND MOTOR

Y STAGE AND MOTOR
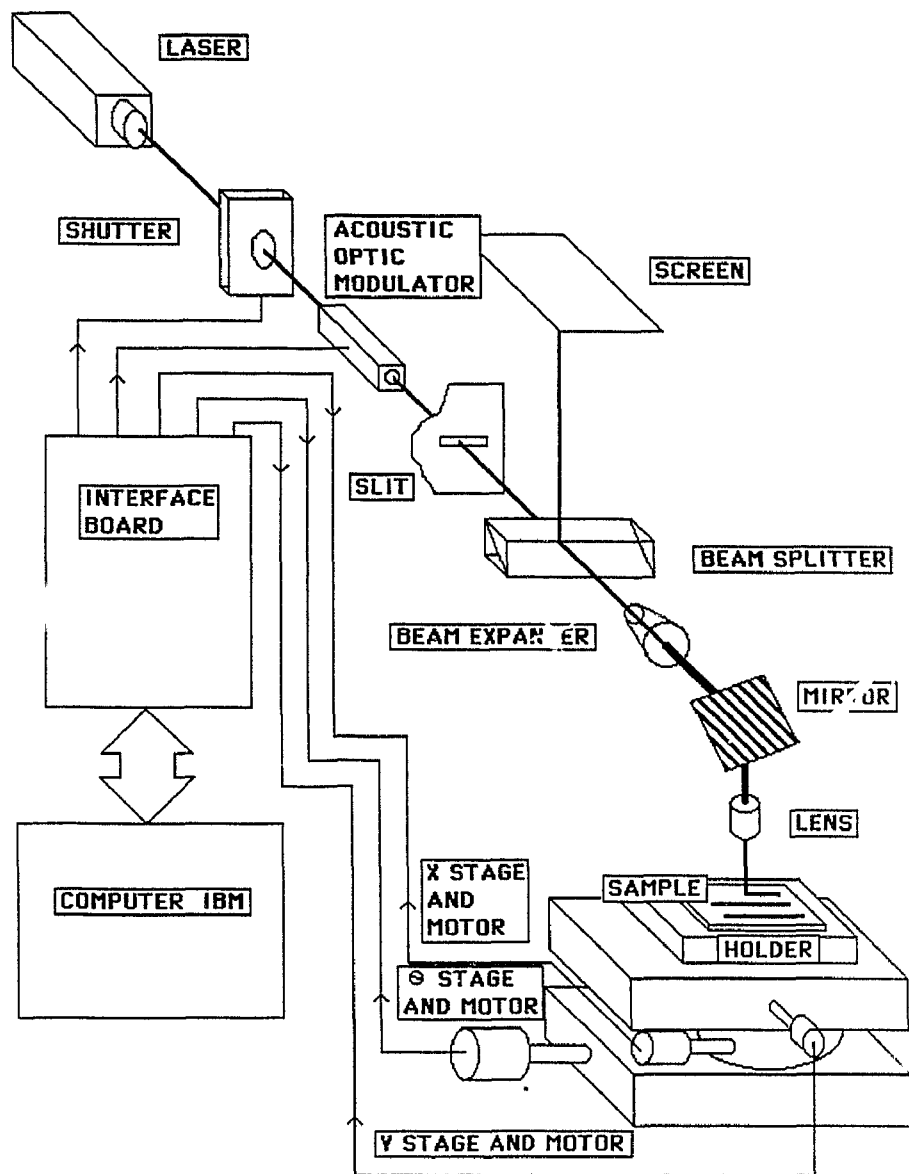
Figure 4.2: Laser writing system.

the sample is maintained to within ± 1 μm of the focusing lens, ensuring that the line width is held to within 0.25 μm.

Computer interfacing: Computerized operation is achieved using an IBM PC fitted with a Techmar Labmaster controller. Three of the output channels are used to control the D. C. motors; one channel is used to control the acousto-optic modulator, while another controls the shutter. Three input channels read the linear position and direction of rotation of the D. C. motors, while another monitors the laser beam intensity.

For the laser sources, the laser writing is limited by the speed of the motors not by exposure time or the IBM's controlling software. The supervisory program is therefore written in BASIC for easy customization and maintenance. All interface driving routines are written in machine language and linked to BASIC with subroutine calls. Modular programming concepts, figure 4.3, ensure that even complicated mask patterns can be readily accommodated.

A typical pattern to be written must first be broken down into a sequence of steps, where each step represents the motion of one or more motors, the control of the acousto-optic modulator, or the activation of the shutter. A subroutine within the main program allows the rapid entry of each step and builds the command execution file. Patterns containing repetitive features can be written into a separate BASIC program, then merged with the main program and run to generate the command execution file. For more complicated designs, a CAD system can be used to generate a drawing file which is recognized by the main program. Execution files are permanently stored on disc to form a library of patterns. In many situations, new designs require only slight changes and an editor can be accessed which allows the addition, deletion, or alteration of an element in an existing execution file. Alphanumeric characters, 40 μm high and based on a 20 segment pattern, can be written to the mask pattern for identification purposes. In figure 4.4, a typical line pattern shows two waveguides with a gap in their centre. The numbers represent
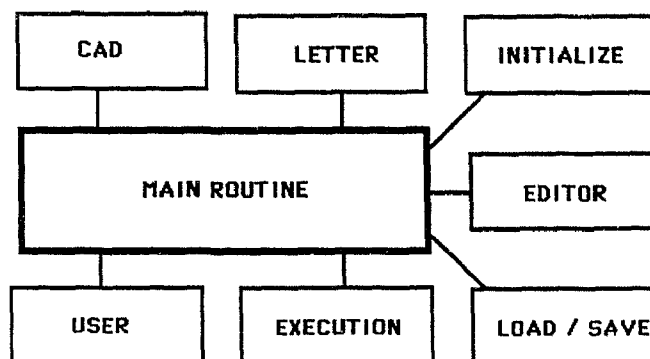
Figure 4.3: Structure of the laser writing BASIC program.

the sequence of execution commands. The (x,y) coordinate system represents the direction of positive motion of the two linear stages.

At position 1, the system instructs the shutter to open, but only after the x motor has travelled 10 μm. This ensures that the motor is up to speed before the writing begins and that a constant line width will be produced. The speed and direction of the x motor are chosen and set to run for 5 mm. This motion, combined with the opening of the shutter, generates the first segment of the line. Also at this time the shutter is instructed to close at the end of the 5 mm line, minimizing the overexposure at the end of the line since, if the motor stops and the shutter remains open, an enlarged spot will result. The remainder of the execution file can easily be read from the figure. Due to the structure of the supervisory program the second line can be generated by rewriting the first line but reversing the x direction and offsetting the written line using the y motor.

This implementation of the laser writing system can expose lines down to 2 μm in width and 24 mm in length. Thinner lines can be written but the lengths must be kept short due to focusing problems. For electrode applications, lines up to 30 μm in width can be written by changing the acousto-optic modulator's amplitude.

Calibration of the laser writing system is required before any masks can be written. In order to determine the settings that expose a line of desired width,
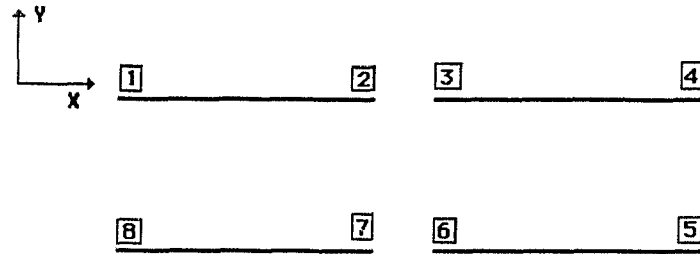
Figure 4.4: Typical laser written line pattern.
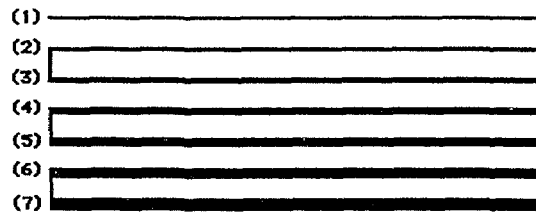
Figure 4.5: Reproduction of a typical line pattern of a calibration run. Line widths are altered by changing the laser power.

several straight lines are written and the system's parameters adjusted. The motors used can provide a linear velocity between 0 to 0.25 mm/sec, but are typically run at 90 percent and the exposure rate is controlled by adjusting the laser beam intensity. The reflectivity of the sample must also be considered, since any light which is not absorbed by the photoresist may be reflected from the bottom and expose adjacent areas. This would result in a overexposure of the channel edge and can lead to poorly defined channel walls. Figure 4.5 shows a reproduction of a typical calibration run. The laser power is adjusted by controlling the amplitude of the acousto-optic modulator. By measuring the line width of the etched metal using a calibrated microscope the system can be calibrated for one motor speed. This type of calibration run must be executed before each laser writing section in
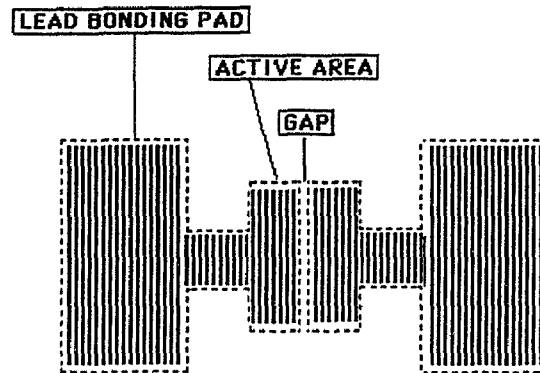
Figure 4.7: Laser writing sequence used to generate the electrode masks. Increasing the power causes the pattern to be solid and defined by the dashed line.

2) Acetone

3) Isopropanol

4) Distilled water

They are then blown dry in a nitrogen jet, placed in a clean storage container and transported to the evaporator where they are coated with a 500 to 1000 $\mathring{A}$ layer of aluminum.

Two types of photoresist can be used in the mask making process. A positive photoresist (Shipley 1350J) will result in an exposed photoresist, due to the writing laser beam, which can be removed upon developing. A negative photoresist (Kodak KFTR) has the opposite effect and leaves the photoresist wherever it was exposed. The steps involved in using these photoresists are given below:

1) Spin a drop of either photoresist at 5000 RPM for 30 seconds to produce a submicron layer.

2) Prebake at 80°C for five minutes to remove the water and rubberize the film.

3) Expose the desired pattern using the laser writing system.

4) Develop the photoresists:

    - for positive photoresist, immerse in the 1350J developer for 2 minutes

while stirring;

     - for negative photoresist, immerse and stir in the KFTR developer which has been thinned 5:1 with the KFTR thinner.

5) Rinse the photoresists:

     - for positive photoresist use distilled water;

     - for negative photoresist use N-butyl-acetate.

6) For negative photoresist, prebaking at 140°C for 20 minutes is necessary to fix the photoresist.

   When the cleaning and photoresist steps are followed exactly the exposed aluminum reproduces the design written by the laser writing system. At this time the exposed metal can be removed using commercial KTI aluminum etchant. To complete the mask making process the remaining photoresist is disolved leaving only the aluminum pattern on glass.

4.3 Waveguide Making

   Two processes, titanium in-diffusion and proton exchange have been used to produce the waveguides in the $LiNbO_3$ crystal substrates. Both systems required to implement the process were setup in the laboratories of the National Research Council of Canada in Ottawa. At a later stage in the research a proton exchange system was setup at Dalhousie University and several slab waveguides produced. A discussion of each process and a description of the required apparatus follows below.

4.3.1 Ti In-Diffusion

   The $LiNbO_3$ substrate surfaces are cleaned following the steps outlined for glass slides. Using a sputtering system or electron beam evaporator a layer of titanium 400 $\mathring{A}$ thick is deposited onto the optical grade surface of the crystal. A positive photoresist is spun onto the surface finalizing the preparation of the

substrate. To obtain the desired waveguide pattern a mask is carefully aligned with the crystal's principal axis. This is achieved by aligning the mask with one edge of the crystal since these substrates are cut along the principal axes. Following photolithographic steps, the waveguide pattern is exposed and developed and the titanium metal etched. The remaining photoresist is then stripped off leaving the bare metal on the crystal ready for in-diffusion.

In-diffusion takes place in a three stage Lindberg oven. The temperature is gradually increased by $100°C$ per hour until $1000°C$ is reached and is then maintained for a predetermined period of time allowing for the diffusion process to take place. Afterwards the oven is set to cool down at $100°C$ per hour until room temperature is reached. During the entire cycle, water vapour is passed through the oven suppressing the out-diffusion of Li_2O. Diffusion theory can be used to predict the index of refraction profile starting with Fick's law[39] and knowing the source profile (Ti strip) and diffusion constant for the temperature of the oven. The functional forms which model many profiles[40-43] are the Gaussian, error function, exponential, and $\cos^R(\theta)$. When the crystals are removed from the oven they contain the waveguides.

4.3.2 Proton-Exchange

The technique of making waveguides using proton exchange is based on the removal of lithium from the crystal and filling the vacated site with hydrogen (proton), forming a hydroxyl group. The laboratory setup is shown in figure 4.8.

A variety of proton sources can be used but in this research benzoic acid with 2 percent of lithium benzoate which becomes liquid at $200°C$ have been employed. The bath is contained in a 7 cm diameter pyrex tube, 2 feet in height, closed at one end. A brass heat sink is used around the base of the tube to stabilize the temperature of the exchange bath. The crystal is suspended from a hook fastened to an insulating cover disk which facilitates the lowering of the crystal into the bath
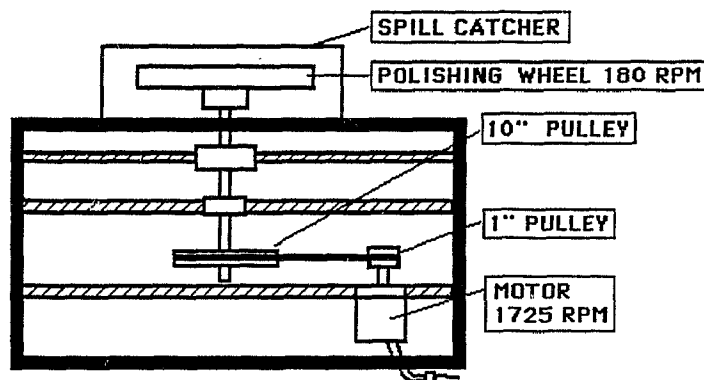
Figure 4.9: Mechanical polishing apparatus.

can be polished at the same time using this holder.

The principle involved in polishing is as follows. First, start with a coarse compound (600 grit) and grind the crystal flush with the face of the C clamp. Then, using a finer grit, scratches produced by the 600 grit are removed and replaced with smaller, shallower scratches. This process of exchanging scratches proceeds through the 9 μm, 6 μm, 3 μm and 1 μm diamond grinding compounds as well. The final polishing stage is mechano-chemical using a liquid suspension of SYTON^{TM}, after which no scratches can be seen on the ends of the crystals. The entire polishing process is slow and requires about 4 hours to complete. During the polishing exercise care must be taken to keep the work area clean since any dirt on the wheels may cause deep scratches in the crystals which are very difficult to remove. Once the crystals are polished, they are removed from the block, separated using acetone, and cleaned once again. Optical fibres can then be aligned and the waveguides analyzed.
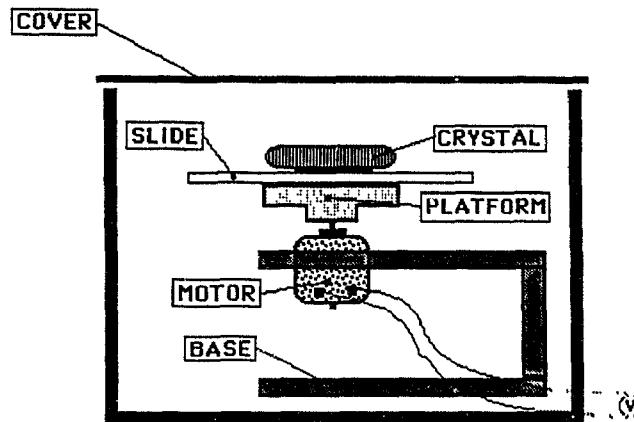
Figure 4.13: Spinner design.

The vacuum system is used to secure the crystal and masks to the moving components of the aligner. It is also used to evacuate the region between the mask and crystal once alignment is achieved, forming a tight contact between the two surfaces. This reduces the effects of diffraction during the exposure stage and enables high quality replicas of the mask to be achieved.

The electrode patterns generated using the laser writing system must be further processed before they can be employed in the mask aligner. This requires that the electrode pattern be cut out of the glass slide and mounted, as shown in figure 4.12. A transparent plastic border secures the mask to the aligning system while foil protects adjacent areas of the crystal during the exposure stage.

For electrode masking, the cleaned waveguide containing crystals is prepared by evaporating 800 $\mathring{A}$ of SiO_2 followed by 1000 $\mathring{A}$ of aluminum. To these layers a coating of photoresist is spun using the spinner of figure 4.13.

Following the alignment and standard lithography steps, the pattern of electrodes can be etched out of the aluminum in close proximity to the waveguide. Permanent electrical contacts to the electrodes can be made by securing thin wires to the lead bonding pads using nickel print (a conducting glue) and enclosing the
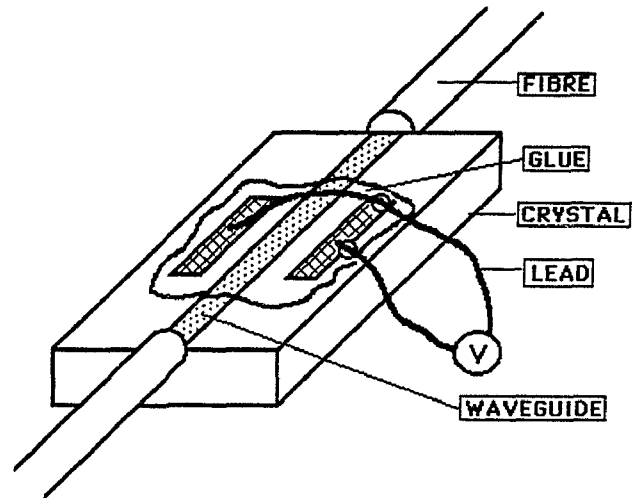
Figure 4.14: Completed integrated-optic device.

assembly in an epoxy for mechanical support. Figure 4.14 shows a completed device with electrodes, bonding leads and optical fibres.

CHAPTER 5. EXPERIMENTAL SETUP

5.1 Introduction

This chapter describes the tools and method of manipulation required in order to perform measurements on slab and channel integrated-optic waveguides. There are two optical measuring setups, prism coupling and fibre coupling, and one electrical contact setup, that were used intensively in this research to analyze the waveguides and devices.

5.2 Prism Coupling System

The prism coupling setup is ideally suited to the analysis of slab integrated-optic waveguides. In this research these waveguides have been manufactured directly beneath the optical grade surface of the substrate and have a graded index of refraction profile. For the waveguide geometry of figure 3.9, the superstrate and substrate are identified as the air and the $LiNbO_3$ crystal layers respectively.

The theory of prism coupling is best described using figure 5.1. A prism of index of refraction n_p is pressed down onto the slab waveguide optimizing the air gap separation.

A beam of light is directed onto the base of the prism where it suffers total internal reflection at the n_p/n_1 interface, setting up a standing wave mode in the prism. This mode is stationary in the x direction but moves in the z direction with phase velocity β_p where $\beta_p = k_o n_p \sin(\theta_m)$. In the waveguide, various guided modes can exist propagating in the z direction with phase constant β_m. All of these

51

Figure 5.4: Enlargement of the prism and waveguide holder.

lines are written in such a way that at high powers the next line overlaps the previous line. Repetition of this action exposes an area instead of just a line. In the centre between the two active areas of the electrodes the x stage is offset just enough to leave a line which is not exposed. This unexposed line is chosen to have a width of several micrometers.

The substrates used to form the masks are prepared from flame polished microscope glass slides coated with aluminum and photoresist. The use of ultra clean slides is of utmost importance since any dirt or film remaining on the surface may lead to defects in the mask. The uncoated glass slides are cleaned ultrasonically for five minutes in baths of each of the following solvents:

1) Trichloroethylene
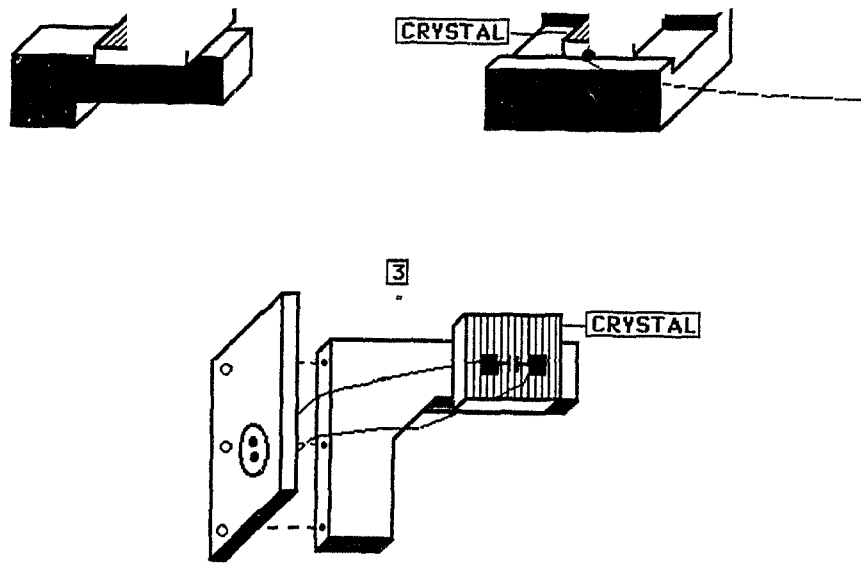
Figure 5.8: Design of three types of crystal holders, 1. Standard crystal holder, 2. Crystal and fibre holder, 3. Electrical lead and crystal holder.

process to be completed at 250°C is in the order of 20 minutes for single mode waveguides and slightly longer for multimode waveguides. This process has been used for making slab waveguides only, and therefore no lithography is required.

4.3.3 Waveguide Termination

End-fire coupling to the integrated-optic waveguides using optical fibres requires that the ends of the integrated-optic waveguides be terminated flat, a task best accomplished by polishing the edge of the crystal. The polishing apparatus is shown in figure 4.9. It consists of a 1725 RPM motor geared down to provide a turning shaft of 180 RPM. Several brass discs with polishing compounds on the upper surface can be fitted to the slowed shaft. Polishing of the crystal edge requires that the crystal be mounted in the C clamp as shown in figure 4.10. Two crystals

have been written and merged to the commercial software enabling the image to be transferred through the serial port to an IBM PC. There the image files can be processed and plotted. For example, one plotting progam calculates the normalized power of the image by summing the individual byte values above a predetermined threshold, and outputs a 3-D intensity plot on the Roland (x,y) plotter. The block diagram of the complete video system from camera lens to plotter is shown below in figure 5.10.

5.4 Electrical Contact Setup

During the experimental analysis of integrated-optic components a means of providing electrical signals to the electrodes is required. This is achieved using a rounded conducting point which can be touched to one of the lead bonding pads using a micromanipulator positioner. A second point can also be manipulated to

to the crystals. Since this work was performed exclusively at Dalhousie University, a mask aligner, photoresist spinner and safe light area were assembled. The design of the mask aligner is shown in figure 4.11, and can be broken down into three systems: positioning, illumination and vacuum.

In the positioning system, one set of translational stages (x_1, y_1) is used to align the mask with the waveguides contained in the crystal. The other set of stages (x_2, y_2, θ_2) moves the crystal and mask into the field of view of the microscope.

The illumination system has two functions. The first is to provide a long wavelength source of light which does not expose the photoresist and is used to illuminate the mask and crystal during the alignment steps. The second is a short wavelength source (Norland Opticure Light Gun, 0.1 W per cm^2 of power for 0.35 to 0.38 μm wavelength range) which is turned on for 10 seconds after the alignment is completed and exposes the photoresist through the mask.
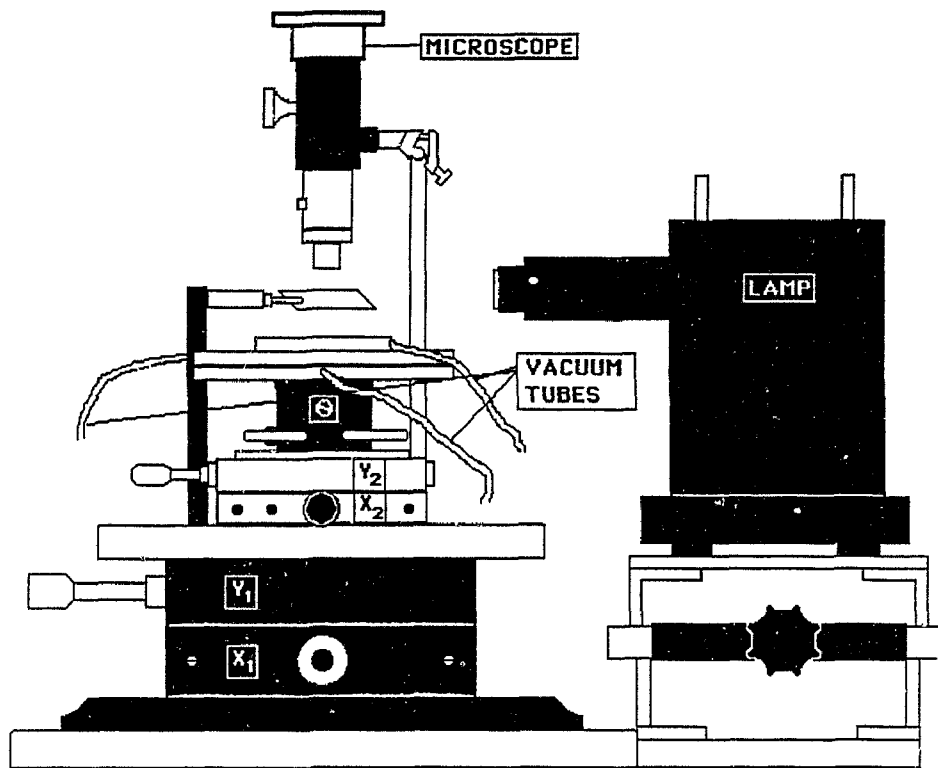
Figure 4.11: Mask aligner design.
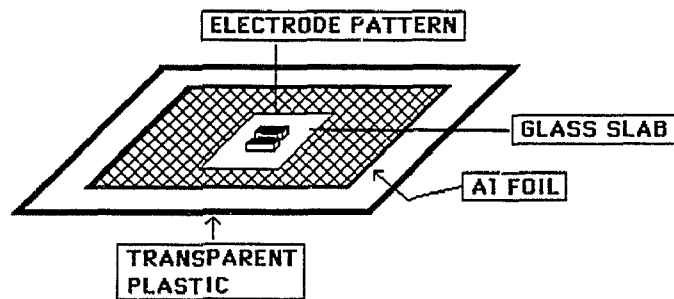
Figure 4.12: Completed electrode mask.
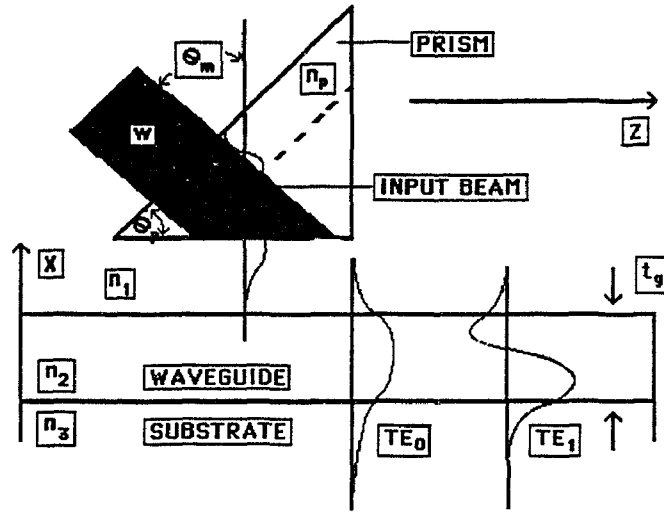
Figure 5.1: Prism coupling arrangement.

guided modes have an evanescent tail extending slightly beyond the n_1/n_2 interface as expressed explicitly in equation 3.17a. If the prism waveguide air gap is of the order of a wavelength, the evanescent tails of the waveguide modes may overlap with the evanescent tail of the prism mode. Then coherent coupling of energy from the prism mode to the mth waveguide mode will occur when θ_m is chosen such that $\beta_p = \beta_m$. The condition for matching the propagation constants can be expressed as:

$$\frac{2\pi n_p}{\lambda_o} sin(\theta_m) = \beta_m \tag{5.1}$$

Although θ_m must be carefully chosen in order to couple to a given mode, a single prism can be used to couple to many different modes by simply changing the angle of incidence of the optical beam. When the beam is not incident perpendicular to the prism interface, a refraction at the input interface will occur and equation (5.1) must be modified accordingly. When performing prism coupling experiments it is more convenient to measure the angle of incidence that the beam forms with the normal to the prism input face. The usable form of the phase matching condition
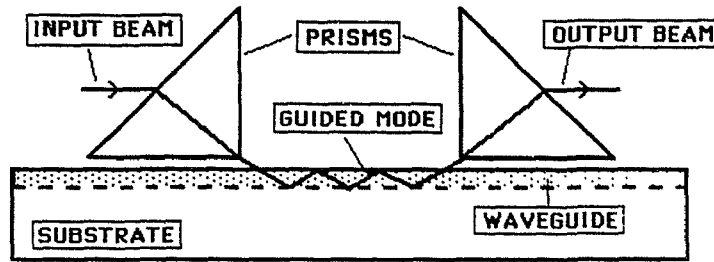
Figure 5.2: Input and output prism coupling orientations.

can be written as:

$$n_1 sin(\phi) = n_p sin(sin^{-1}(\frac{\beta_m \lambda_o}{2\pi n_p}) - \theta_p)$$ (5.2)

where θ_p is the base angle of the prism.

Measuring the propagation constants for a waveguide structure can provide information on the index of refraction profile, depth of waveguide, number of modes and the anisotropy if used with the dispersion equation (3.29).

Guided modes can also be coupled out of the waveguide using a similar prism due to the reversible nature of light waves. The principle requires once again the overlapping of the evanescent tails of the modes in the gap region. The guided power will couple into the prism where it is free to refract from the prism's inclined surface into the air and generate a well defined light beam. The angle of exit for this beam with respect to the prism's endface depends on the propagation constant of the guided mode, as can be seen from equation (5.2). Modes with different propagation constants will exit the prism at different angles.

The geometrical arrangement of the input and output prisms in position above the slab waveguide is shown in figure 5.2. Optimal coupling occurs when the incident beam strikes the back base edge of the prism as shown in the figure.

The experimental setup required to accomplish prism coupling waveguide analysis is shown in figure 5.3 and 5.4. The setup is isolated from vibration by
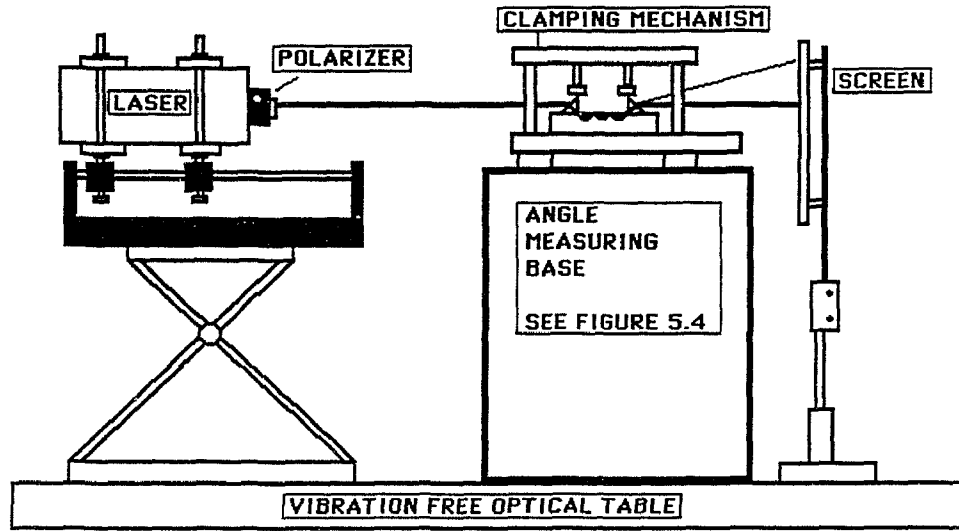
Figure 5.3: Experimental setup for prism coupling measurements.

mounting all the components onto a vibration-free air suspension table. To facilitate description of the system, the laser beam is traced through the setup. This is a natural way to proceed since each component is adjusted in that sequence. The source consists of 1 mW He-Ne, 0.6328 μm laser. It has a 1.2 mm output beam diameter with a divergence angle of 1.5 milliradians. A rotatable polarizer located next to the exit aperture can be used to select either the TE or the TM waveguide polarization. The polarized beam then propagates into the coupling prism positioned above the waveguide mounted to the measuring base. An enlargement of this piece of apparatus is shown in figure 5.4. The clamping mechanism applies a gentle force to the prism and waveguide containing substrate, minimizing the air gap between these components. Several translational and rotational stages facilitate the positioning of the prism and crystal with respect to the polarized laser beam. Two of the translational stages serve to align the input prism's back edge with the central rotation axis of the spectrometer base. The smaller rotational stage adjusts the angle between laser, prism and waveguide, such that all three components are
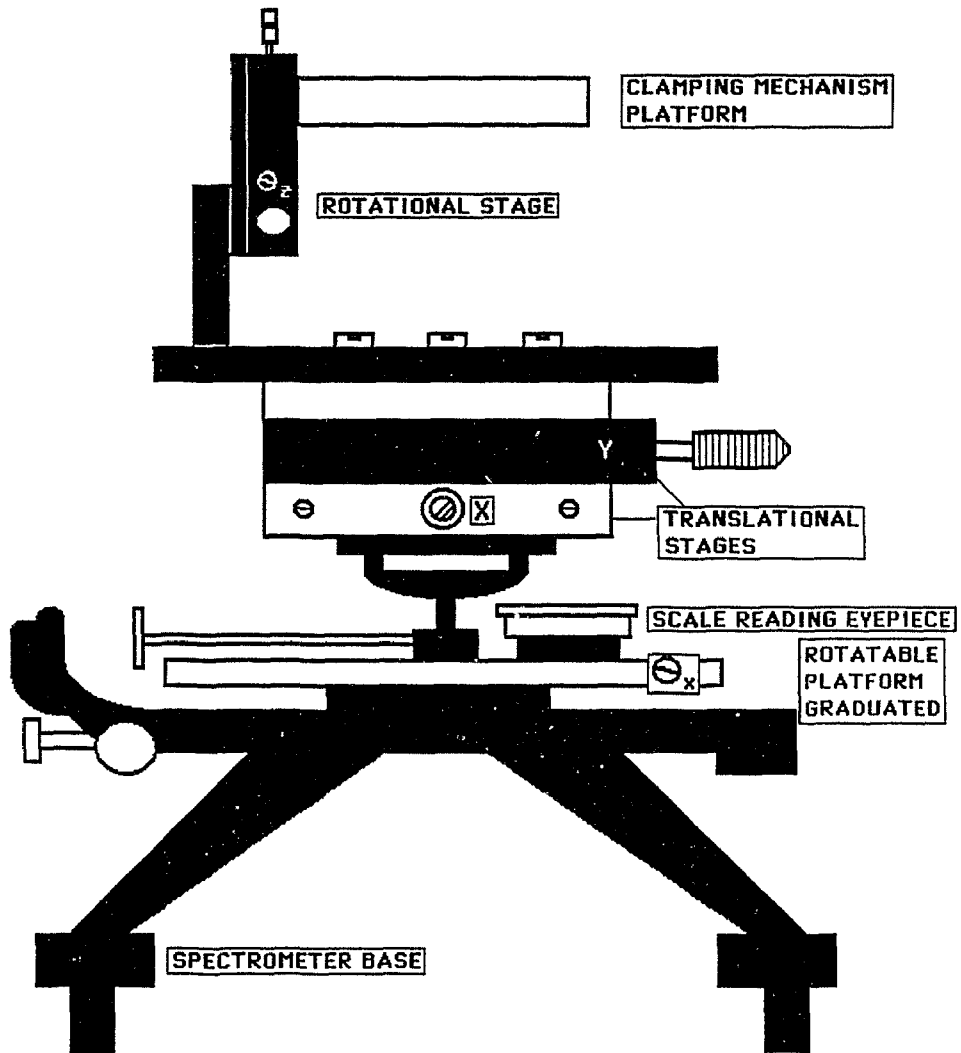
Figure 5.4: Enlargement of the prism and waveguide holder.

colinear and the laser beam remains in the horizontal plane as it passes through the components. This combination of stages enables measurement of the coupling angles for the various modes.

Light which is coupled to one of the modes of the waveguide will propagate, as it is guided in the structure, until it encounters the second prism. There it is coupled out of the waveguide into the prism and finally refracts into the air. A screen located in the exit path of the beam will show a well defined high intensity spot corresponding to the guided mode. Due to the lack of lateral confinement in the slab waveguide, light on both sides of the bright spot will also be observed. If the waveguide can support other modes not excited by the input prism, a low intensity line for each of these modes will also be observed on the screen. These weak lines, along with the principal excitation line, are known as m lines and are the subject of analysis when using the prism coupling technique.

5.3 Fibre Coupling Setup

This setup is best suited to the analysis of channel integrated-optic waveguides. To excite the guided modes, light from a cylindrically symmetric fibre is coupled to a waveguide of rectangular symmetry. Analysis of the waveguide properties proceeds by observing the output mode profile from the exit end of the guiding structure.

The first stage of the fibre coupling setup is shown in figure 5.5. As in the case of the prism coupling setup, the components will be discussed as they are encountered by the laser beam.

A 15 mW He-Ne laser operating at a wavelength of 0.6328 μm is used as the light source. A neutral density filter (Ealing number 22-8957), positioned next to the exit aperture of the laser, enables variations of the beam's intensity (0-24 dB). The transmitted beam is then polarized (rotatable polarizer) and centered onto a 100X microscope objective lens. The centering is accomplished using the x and
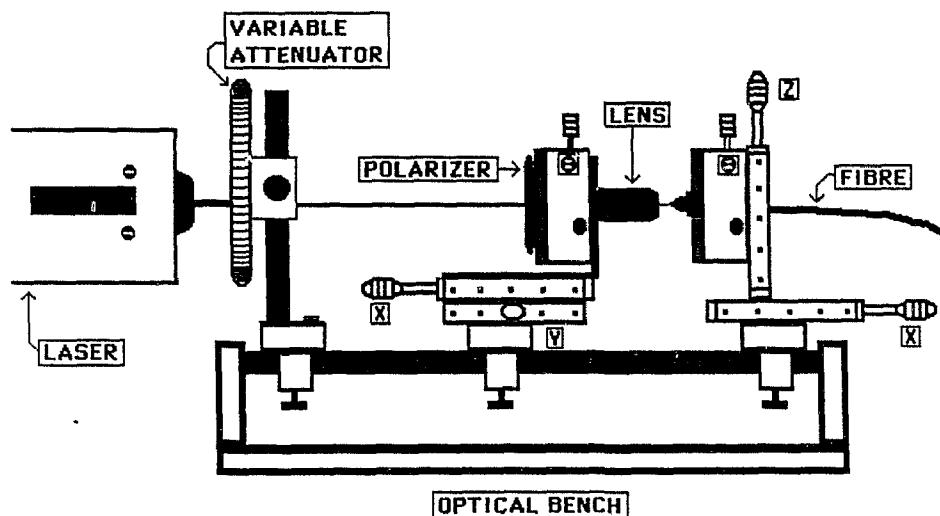
Figure 5.5: Laser to fibre coupling.

y translational stages and observing the transmitted light pattern of the circular aperture on a small screen.

A pair of translational stages (x and z) position the endface of a polarization preserving fibre (PPF) in the focused laser beam. The rotational stage is used to align the preferred axis of the fibre with the polarized laser beam. For stability the combination of neutral density filter, polarizer, microscope lens and polarization preserving fibre are mounted on a single optical bench. This bench is mounted onto the same triangular bench that supports the laser and maintains the overall alignment.

The second stage of the fibre coupling setup is shown in figure 5.6. In this setup the fibre is aligned with the waveguide and the output guided light is analysed. This apparatus can be divided into three parts: fibre alignment, waveguide alignment and video camera. For stability during measurements these assemblies are mounted onto a vibration free air suspended table.

Fibre Alignment: The end of the polarization preserving fibre is mounted onto the platform of the three-axis translational stage configuration shown in figure
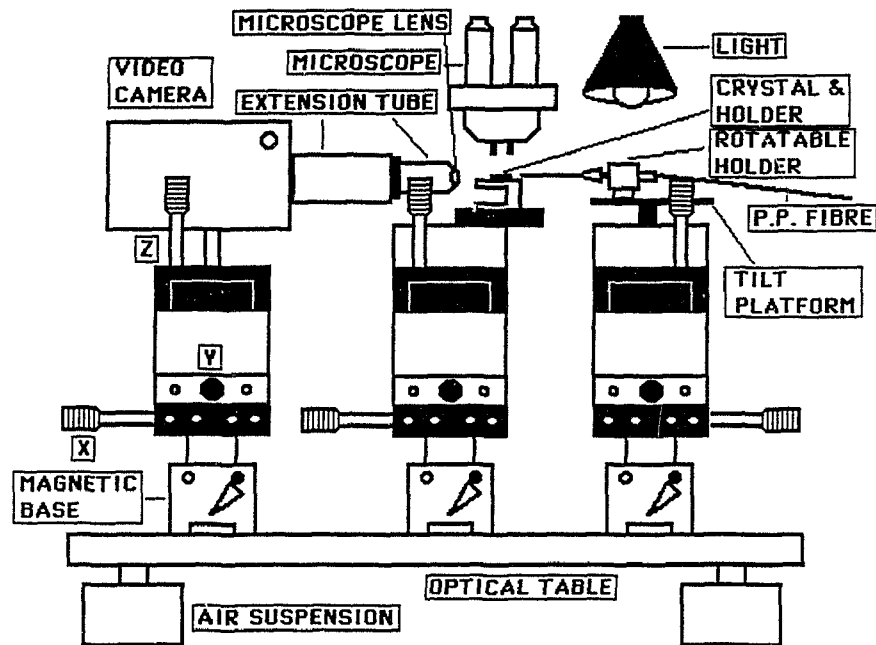
Figure 5.6: Fibre, waveguide and video setup.

5.7. These stages provide the necessary degrees of freedom to enable alignment of the fibre with the integrated-optic waveguide. A tilt adjustable stage is located on the platform and this enables the removal of any angular offsets between the waveguides. The fibre is held in place in a rotatable holder which facilitates the selection of the input polarization to the integrated optic waveguide.

Waveguide Alignment: The crystal to be analyzed is mounted on a similar three-axis translational stage positioner as above except that the tilt and rotational holder have been replaced by one of the crystal holders of figure 5.8.

Holder 1 is used in general analysis of the waveguides. The crystal is mounted as shown such that the input and output ends of the waveguide overhang the edges of the holder.

Holder 2 is used when optical fibres are to be secured to the waveguide. As shown in the figure, the crystal is positioned in the depressed region with waveguides
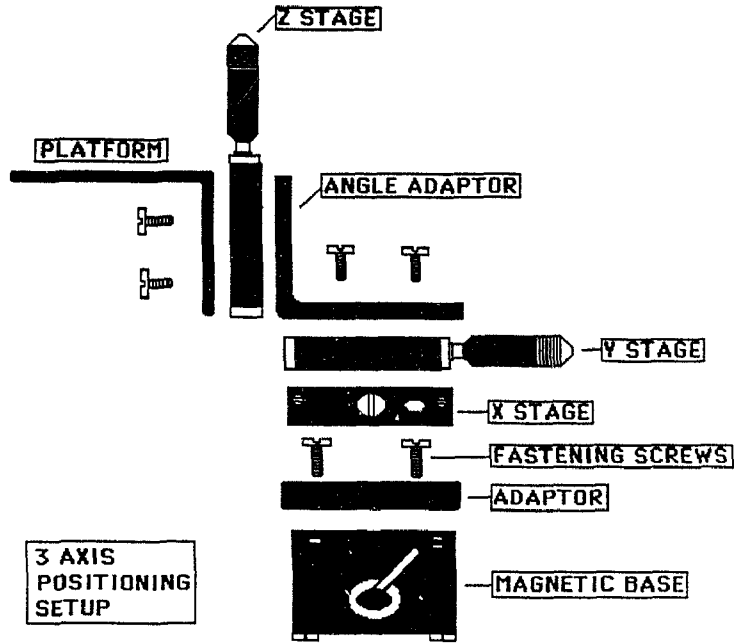
Figure 5.7: Three-axis positioning configuration.
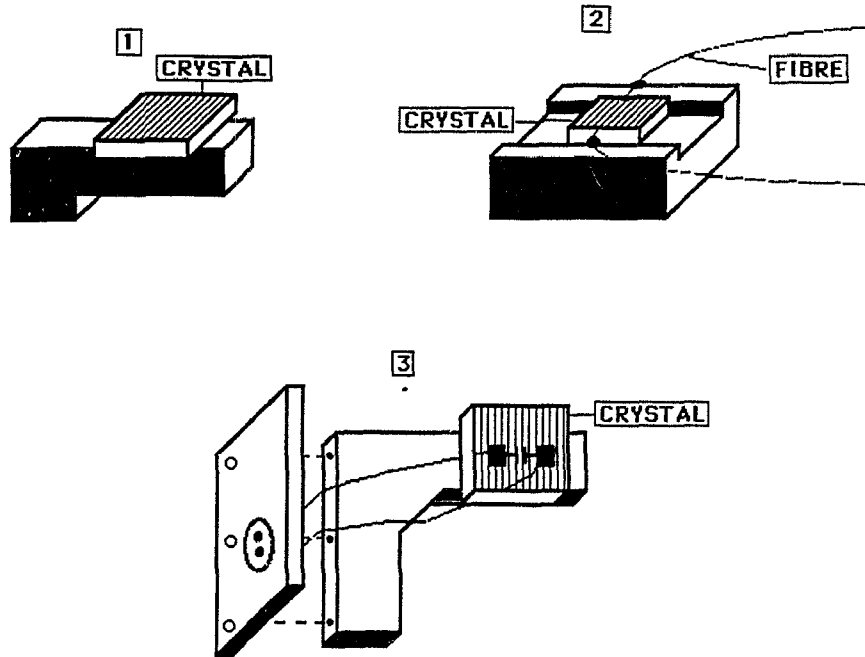
Figure 5.8: Design of three types of crystal holders, 1. Standard crystal holder, 2. Crystal and fibre holder, 3. Electrical lead and crystal holder.
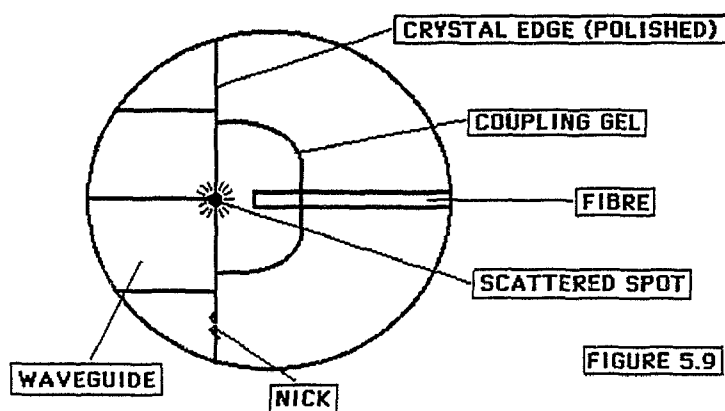
Figure 5.9: Field of view and optimal coupling to waveguide.

oriented across the holder. The fibres are aligned with the waveguides and secured to the raised ledge for mechanical support using U. V. cured epoxy.

Holder 3 is used when electrical leads are to be secured to the electrodes etched on the crystal. The crystal is positioned with waveguide ends overhanging the narrow neck of the holder, as shown.

To facilitate alignment of the optical fibre to one of the waveguides of the crystal, a low power microscope is focused onto the crystal's waveguide containing surface. An area of approximately 3 mm in diameter can be viewed at any time. Focusing on the edge of the crystal and waveguide, the fibre can be translated into position. Best coupling to the integrated-optic waveguide occurs when light launched by the fibre scatters off the edge of the crystal where the waveguide is terminated, as shown in figure 5.9. When the coupled power to the waveguide is large, scattered light along the length of the integrated-optic waveguide can also be seen through the microscope. Fine tuning of the power coupling is accomplished by observing the output light from the other end of the crystal's waveguide using a video camera.

Video camera: This subsystem consists of a low light level video camera

fitted with either a 10X, 40X or 100X microscope objective lens and a black and white monitor for direct viewing of the image. A 15 cm extension tube between the lens and camera serves to further magnify the images. Inside this tube can be placed a rotatable polarizer for studying the polarization states of the images, or a beam splitter which diverts a fraction of the optical power onto an optical fibre for measurement purposes. The camera and assembly are also mounted on a similar three-axis translational stage configuration as above. These stages enable focusing of the microscope lens onto the end of the crystal and waveguide forming a near field image of the guided mode pattern which can be viewed on the monitor. Fine adjustment of the position of the input fibre can enhance the coupling of light to the waveguide and be confirmed as a brighter image on the monitor.

Permanent storage and processing of observed images is accomplished by sending the video signals into an Apple II+ fitted with a video card. In addition, each pixel is digitized on a 256 gray scale. A full 64 kilobytes of memory (256 rows x 256 columns) is required to store and display one image. Additional routines have been written and merged to the commercial software enabling the image to be transferred through the serial port to an IBM PC. There the image files can be processed and plotted. For example, one plotting progam calculates the normalized power of the image by summing the individual byte values above a predetermined threshold, and outputs a 3-D intensity plot on the Roland (x,y) plotter. The block diagram of the complete video system from camera lens to plotter is shown below in figure 5.10.

5.4 Electrical Contact Setup

During the experimental analysis of integrated-optic components a means of providing electrical signals to the electrodes is required. This is achieved using a rounded conducting point which can be touched to one of the lead bonding pads using a micromanipulator positioner. A second point can also be manipulated to

Figure 5.10: Block diagram of the video system.

the other pad completing the device's electrical requirements at the crystal. One of the micromanipulators with point contact attached is shown in figure 5.11. Due to their design they can be used with both the prism coupling and fibre coupling setups.

The applied voltages can be either DC or AC, depending on the analysis desired. For DC applications, the apparatus shown in figure 5.12 A is employed. A 400 volt power source is connected through a reversing switch to the BNC connector of the pair of point contacts and monitored on a voltmeter. For AC applications the voltage source of figure 5.12 A is replaced by a function generator and amplifier capable of producing signals up to 400 volts peak to peak. The voltmeter is replaced by an oscilloscope for both observing and mea~ring the modulating signal. For the low frequency modulation experiments, AC signals with frequencies of 30 Hz were used.
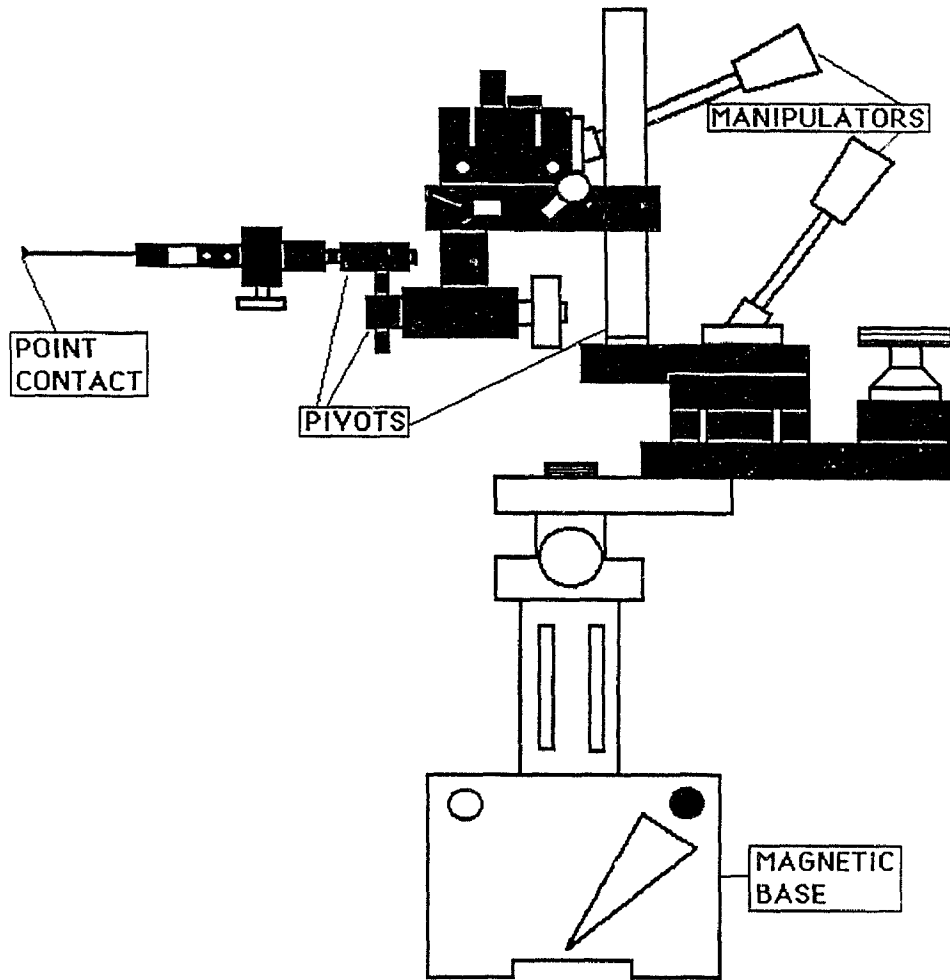
Figure 5.11: Micromanipulator and point contact.
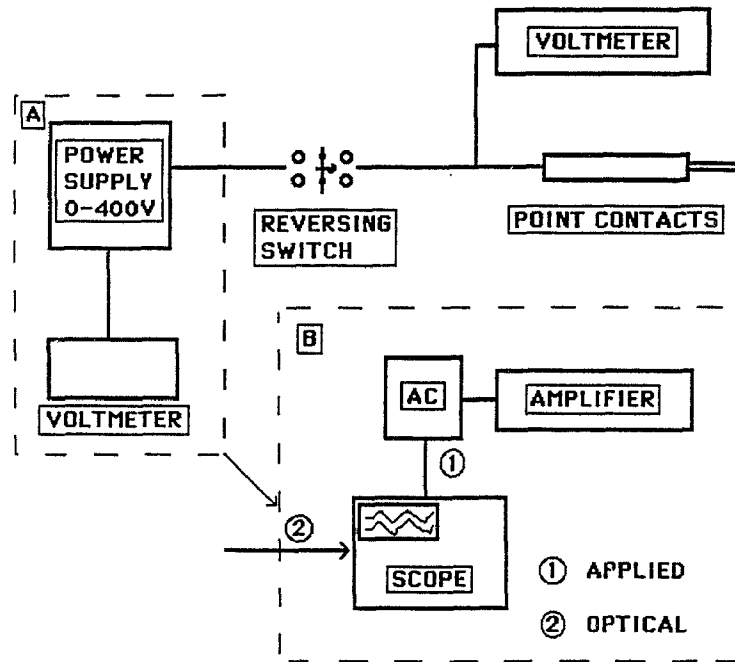
Figure 5.12: A - DC electrical system, B - AC electrical systems.

CHAPTER 6.   CLADDINGS ON INTEGRATED-OPTIC WAVEGUIDES

6.1 Introduction

The propagation of two mutually orthogonal modes, TE and TM, in a waveguide structure has been discussed in section 3.1. During the designing stages one can adjust the diffusion or exchange parameters (time, temperature, source availability) to achieve single (TE, TM) mode operation in the waveguide. As shown in figure 3.5, it is difficult to obtain a single TE mode or TM mode waveguide since the propagation constant (β) for each pair of modes is almost equal. Some integrated-optic devices are polarization sensitive[44], hence the proper selection of the input polarization is crucial. For instance, the electro-optic effect in $LiNbO_3$ has its strongest coefficient (r_{33}) along the Z axis and, as a result, an applied electric field can cause an appreciable change to the extraordinary index of the waveguide structure while leaving the ordinary index unchanged. If a mode is polarized with its E field oriented along the z axis, it will experience the extraordinary index which can be altered by an applied electric field. A mode polarized along the X or Y axis will encounter the ordinary index and propagation will be unaffected even when the external fields are applied. It is therefore desirable to design around a particular pair of modes (TE_o, TM_o) and then remove the unwanted mode by some means. Thus control of the input polarization to the active elements of a device is required and, as a result, polarizers and polarizing devices become important.

One method of selecting which polarized mode is excited in the integrated-optic waveguide is to utilize an input polarization preserving fibre (ppf) coupled to the waveguide (figure 6.1). The preferred axis of the fibre is aligned with either of

65
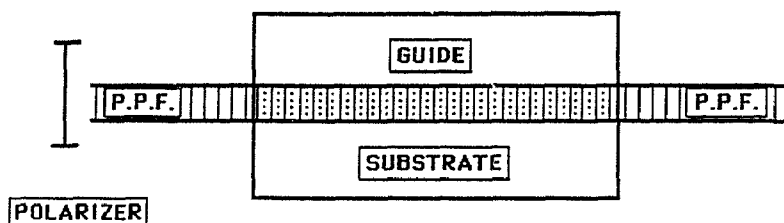
Figure 6.1: Prepolarization technique using polarization preserving fibres.

the transverse axes of the crystal's waveguide. Polarized light in the fibre parallel or perpendicular to the preferred axis enables either of the TE or TM modes of the waveguide to be selected. This requires that the light be polarized prior to entrance to the fibre or that fibre optic polarizers be employed[45]. The use of the relatively highly priced polarization preserving fibre and the need for a polarizing device makes this technique mainly suitable for laboratory prototyping or short distance applications.

A more desirable technique is to polarize the light at the entry of the crystal waveguide before the active elements of a device are encountered. Relatively inexpensive single mode fibres can then be utilized to couple the light into the integrated-optic waveguide in this configuration. The total losses are comparable to those using polarization preserving fibres since the number of transmitted components remains the same. The more common techniques for selecting the polarization state of the mode in integrated optic devices are discussed below.

6.1.1 Anisotropic Crystal

The principle involved is to filter out one of the polarizations by introducing a cover layer with a refractive index larger than that of the waveguide for one polarization and smaller than the waveguide for the other polarization[46,47].

As shown in figure 6.2, if the waveguides are fabricated on Z-cut $LiNbO_3$
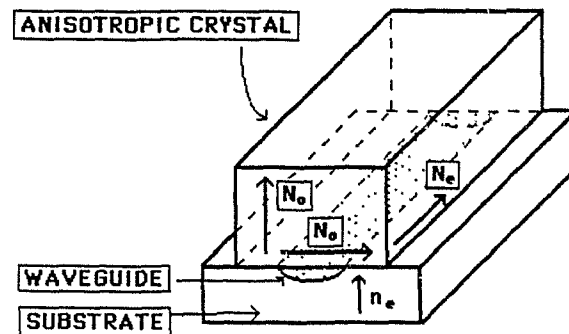
Figure 6.2: Polarizer using anisotropic crystal superstrate.

substrate, the TE and TM modes interact with the ordinary and extraordinary indices respectively. A superstrate of either X-cut cut or Y-cut LiNbO$_3$, oriented with the extraordinary index directed parallel to the crystal interface will pass the TE polarized light unaltered while the power of the TM light is coupled into the superstrate, since $n_o > n_e$. The index of refraction profiles for each waveguide mode are shown in figure 6.3. The success of this technique depends highly on the quality of the contact between superstrate and substrate. Experimental observations by T. Findakly et. al.[46] have measured extinction ratios between TE and TM modes as high as 30 dB for a superstrate length of only 2.5 mm without any measured increase in loss for the TE modes.

6.1.2 Metallic Cladding

The principle here is to place a metallic cladding above the waveguide, as shown in figure 6.4, in order to introduce a differential loss between the TE and TM modes[48-52].

The metal is characterised by an imaginary as well as a real component to the dielectric constant and thus the index of refraction also has an imaginary component. The wave equation for the waveguide structure with the metal present
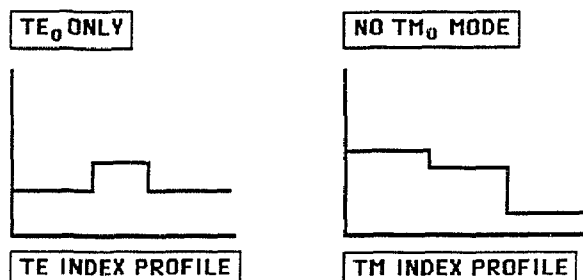
Figure 6.3: Index of refraction profiles as seen by the TE and TM modes.

must consider both contributions. Depending on the waveguide profile, the solutions to the wave equation may be obtained and is best described by introducing an imaginary part to the propagation constant $(\beta = \beta_r - i\beta_i)$[48-52].

The propagation factor, β_i, now introduces a new exponential decay factor, $e^{-2\beta_i x}$, in the propagation direction. It is this exponential factor which leads to attenuation of the guided light. These polarizers are absorptive in contrast to the leaky loss of the superstrate-substrate combination.

The absorption of the TM polarized waveguide mode is due to a coupling of surface plasmons in the metal layer. Figure 6.5 shows the mode profiles for the lowest TE and TM modes before and after a metal cladding is introduced to a slab waveguide structure. For the TE mode, the effect of the metal is to push the mode's profile slightly towards the substrate leaving a small component present at the metal-waveguide interface. The TM mode on the other hand is severely disrupted by the presence of the metal and has a large component present at the metal-waveguide interface. The TM mode suffers the highest attenuation[52] since it has the larger component at the interface and attenuation ratios from ten to several hundreds between the TM and TE modes have been reported[51]. It has been shown by various authors[51,53-55] that the TM mode losses can be increased by introducing a buffer layer between the waveguide and the metal layer, while reducing
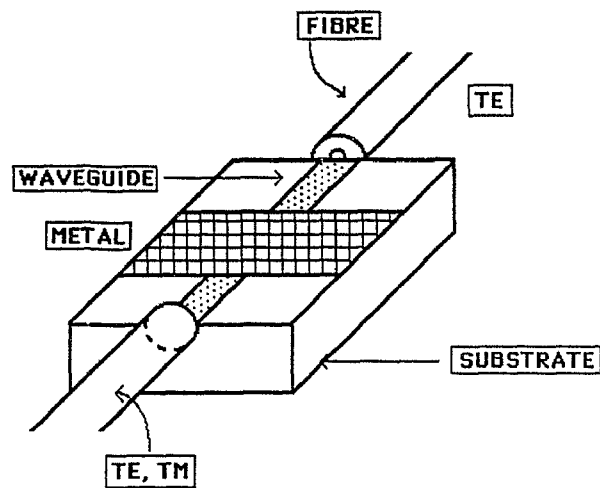
Figure 6.4: Metallic cladding integrated-optic polarizer.

the losses of the TE modes. The effect of the metallic cladding is also of interest in electrode designs since the metal plates may be positioned in close proximity to the waveguide and thus altering the waveguiding properties and seriously affecting the device's output characteristics.

6.2 Experimental Investigation of Metallic Claddings

A metal cladding integrated-optic polarizer was fabricated by sputtering a 400 $\mathring{A}$ layer of titanium metal onto the optical grade surface of an X-cut LiNbO$_3$ crystal. From this film strips of 4, 6, 8, 10 and 12 μm in width were etched directed along the Y axis and then in-diffused. The waveguide ends were carefully polished and the modes excited using 0.6328 μm light delivered by a single mode fibre. Investigation of the waveguides showed that by translating the fibre laterally, several modes could be excited.

A 3 mm length of 300 $\mathring{A}$ thick aluminum was evaporated onto the waveguide containing surface of the crystal. The bulk properties of the metallic cladding were investigated by launching a prepolarized beam into the waveguide and observing
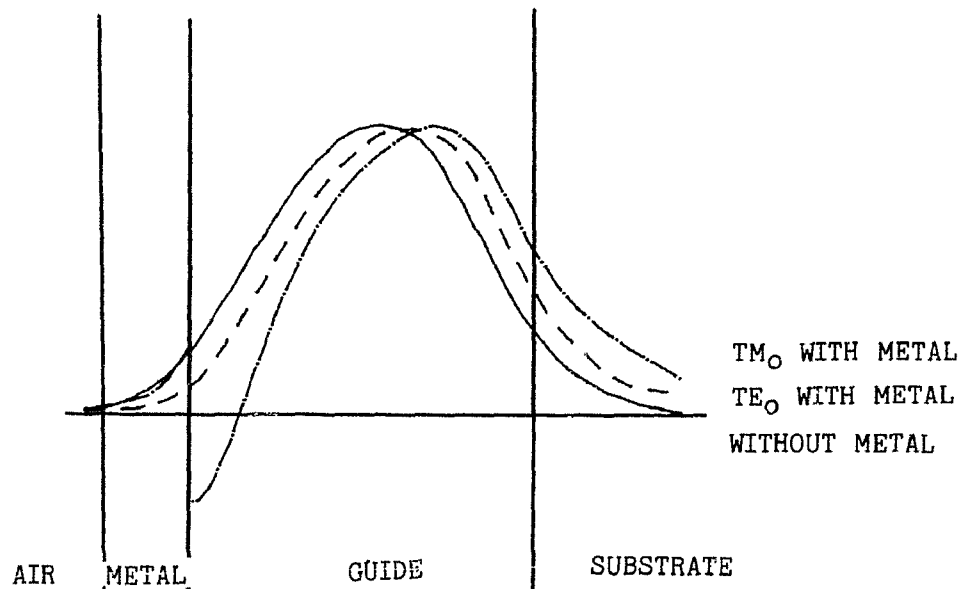
Figure 6.5: TE and TM mode profiles before and after the metal is introduced.

the scattered light from above the guide. When TE polarized light was launched into the waveguide (figure 6.6 A) scattered light could be observed on both sides of the aluminum cladding confirming the passage of this component under the metal. The TM polarized input light (figure 6.6 B) showed scattering from the waveguide on the side prior to the metal cladding and no scattering from the waveguide after the metal. These observations were also confirmed by monitoring the output light level from the exit end of the waveguide using the video display system.

A prepolarized beam rotated at an angle with respect to the waveguide's transverse axis (T_E plane) was input into the 8 μm channel. Figure 6.7 shows a single video raster line through the center of the second order mode profiles for input polarization angles of 0, 30, 45, 60 and 80 degrees. Table 6.1 shows the excellent agreement that exists between the peak height of the profiles at the various angles and Malus's law, when the nonlinearity of the detector is included. This data confirms that only the TE component of the input light is guided and demonstrates the polarization properties of the metal cladding.
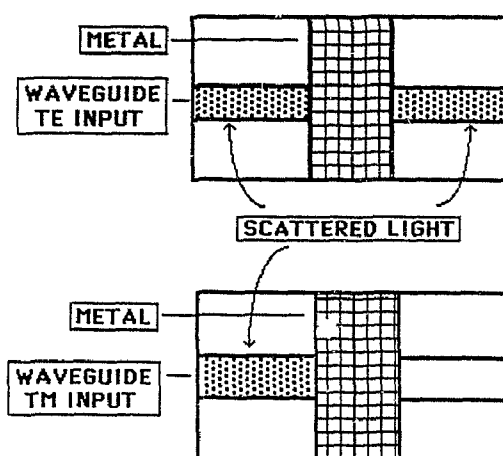
Figure 6.6: Scattered light as observed from above the waveguide, A. TE input polarized light, B. TM input polarized light.

Integrated optic devices which require TE polarized light input to the active elements can be accommodated with this type of polarizer. Once the metal is placed on the surface of the crystal, the polarization properties are fixed and cannot be changed. This may be undesirable in certain system configurations requiring the flexibility of polarization selection during operation. To accommodate these systems, a variable polarizer would be desirable. Such a polarizer, using mercury as the metallic cladding, and its applications are the subject of the remaining sections of this chapter.

Table 6.1

angle	V_{max}	$V_o(cos(\theta))^2$
0	23	23
30	20	20
45	18	16
60	12	12
80	6	4
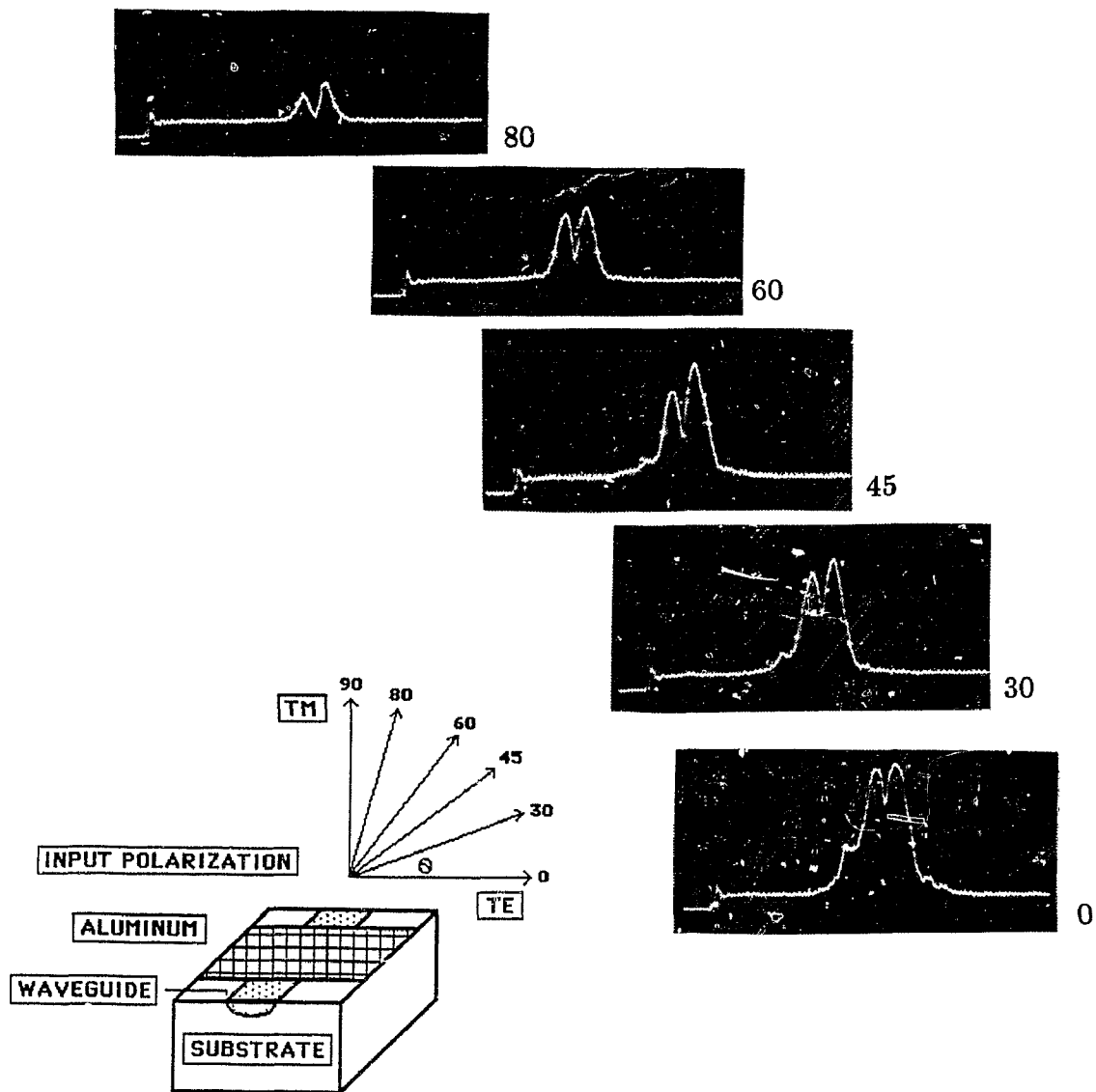
Figure 6.7: Raster line through the mode profile for various input polarization angles.
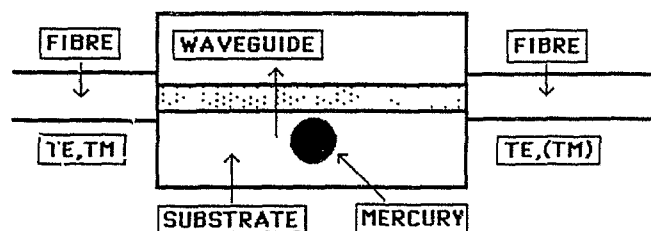
Figure 6.8: Design of the mercury polarizer.

6.3 Mercury Polarizer

The design of the polarizer using mercury as the metallic cladding is shown in figure 6.8. The waveguide was formed from a 4 μm wide titanium strip in-diffused into a Z-cut crystal. The mercury drop of 2.2 mm in diameter, shown as a black disc, is positioned on top of the crystal and close to the waveguide. Liquid mercury is an ideal choice for the cladding since it does not wet the surface of the crystal, forms a good contact with the waveguide, surface tension restores the shape of the drop, and it can be manipulated on and off the waveguide easily. The pair of single mode fibres shown are used to couple light to and from the waveguide. Mercury has been used as a probe to sample device performance such as measuring waveguide losses[57,59,60] and the effects of buffer layers between metal claddings and waveguides. In fact we have used mercury[61] as a technique for testing the alignment of integrated optic components with optical fibres.

Figure 6.9 shows the experimental data of the output power level as the mercury drop is translated across the waveguide, initially propagating both polarization components which are equally excited. A recent paper[59] has reported results of translating a mercury drop laterally across an ion- exchanged waveguide in glass and obtained a curve, similar to ours, of output power versus the lateral position of the mercury drop.

In the figure 6.9 a difference of 3 dB in output power was observed when the drop is on and off the waveguide. From the results of the metal cladding ex-
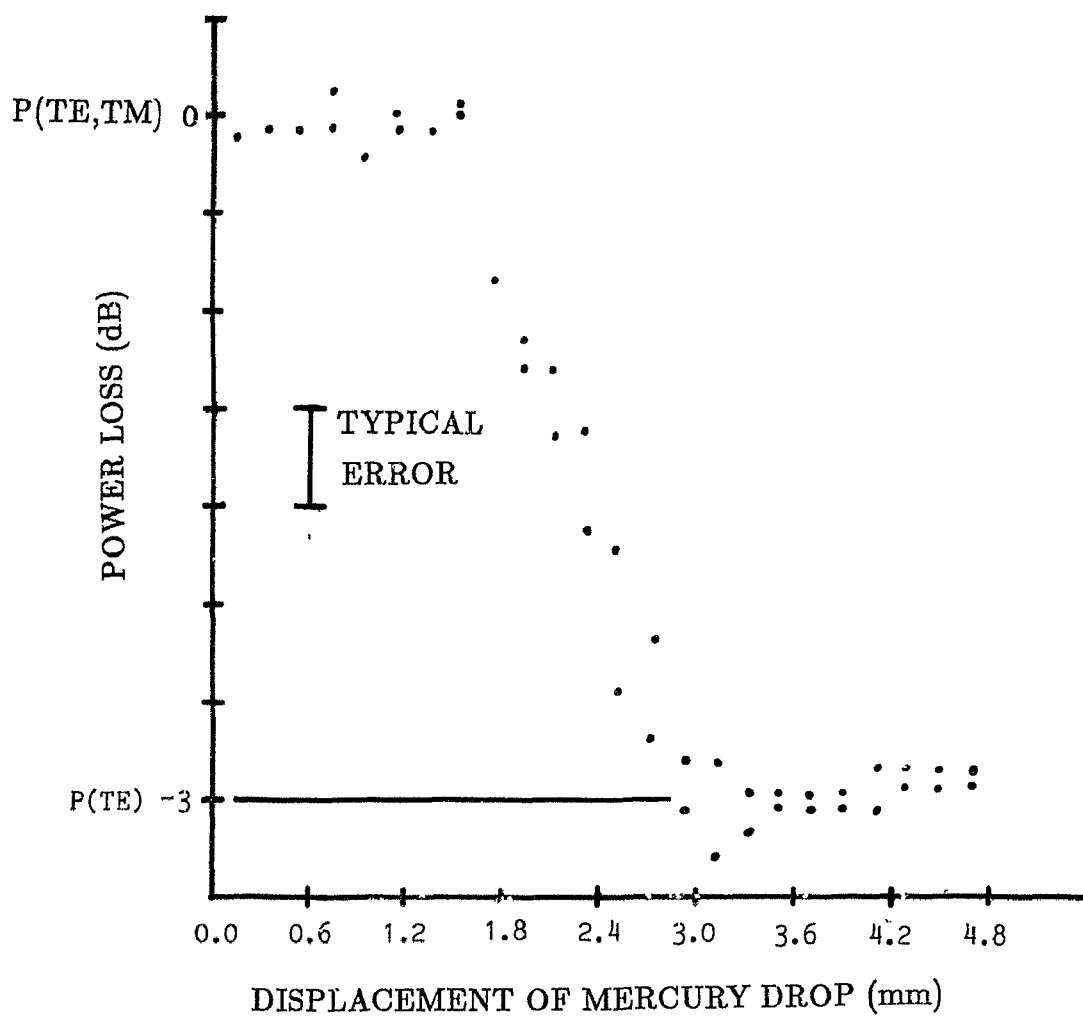
Figure 6.9: Output power versus mercury position.
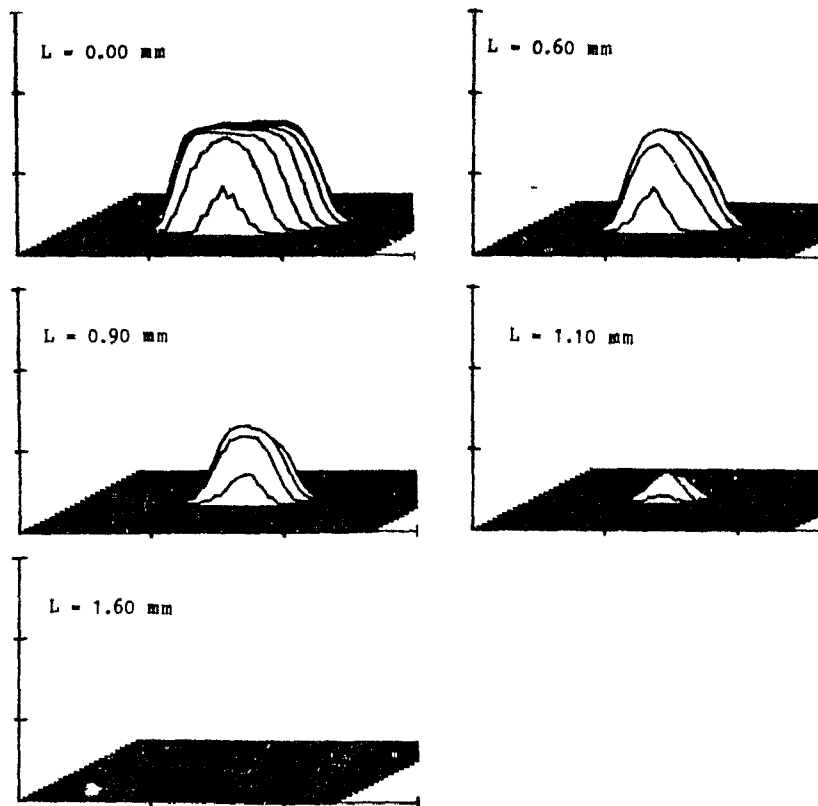
Figure 6.10: Mode profile attenuation as the Hg drop is translated onto the waveguide.

periments it was expected that the TM component should be attenuated producing the observed power decrease. The origin of the power decrease was investigated by replacing the input fibre with a polarization preserving fibre, removing the output fibre and viewing the end of the waveguide with the video camera and monitor. TM polarized light was launched into the waveguide and the output mode profiles were examined as the drop was translated across the waveguide. Figure 6.10 shows the output modes for the interaction lengths indicated and shows no power exits the waveguide for a mercury cover length of 1.6 mm. The mode profiles for TE polarized light were also examined but showed no change as the drop was translated across the waveguide. These observations confirm that the TM component caused the power loss displayed in figure 6.9.
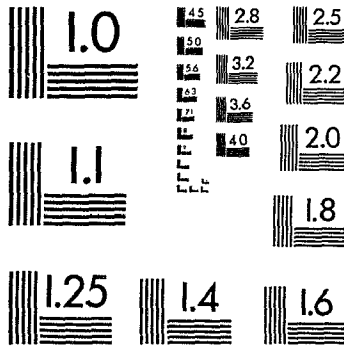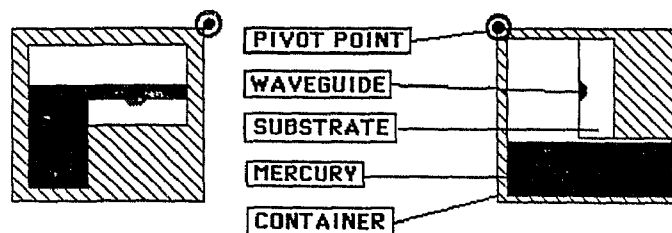
Figure 6.11: Design of the liquid level sensor.

A computer program was written to theoretically model the output characteristics of this polarizer, by plotting the power attenuation factor, $e^{-2\beta_i L}$, as a function of the interaction length L, for the circular mercury drop, 2.2 mm in diameter. The attenuation coefficient $(2\beta_i)$ which best fit the recorded data is 24 cm^{-1} which represents a loss of 104 dB/cm. From the features of the graph in figure 6.9 and the mode profiles of figure 6.10, several integrated-optic devices can be designed using mercury as the metallic cladding. Discussed here is a liquid level sensor, displacement sensor and electro-wetting integrated-optic switching element.

6.3.1 Liquid Level Sensor

The design of the integrated-optic liquid level sensor is shown in figure 6.11. It is analogous to the electrical liquid level sensor using a mercury drop to make the electrical contact.

The sensor consists of a hollowed cube containing mercury in a small reservoir. An integrated optic waveguide with fibres attached is fastened to the ledge in the reservoir so that, in the upright position, no mercury covers the crystal. When rotated through 90 degrees, the mercury will cover the waveguide forming a metallic cladding and attenuate the guided TM components.
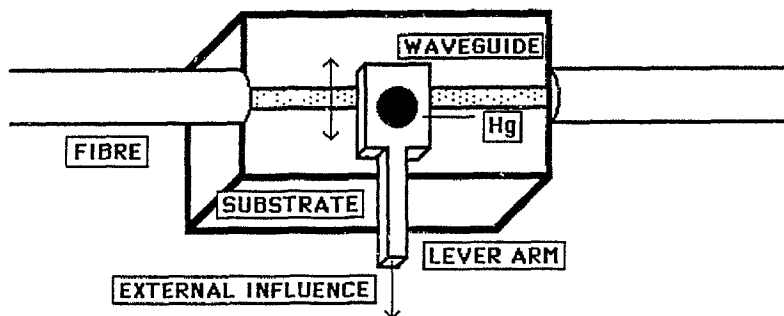
Figure 6.12: Design of the displacement sensor.

The change in signal of 3 dB between the two orientations will be recorded for an arbitrarily polarized input fibre power. The lack of electrical components in the sensor enables this design to be utilized in liquids which, for example, may be flammable.

6.3.2 Displacement Sensor

The basic design of this sensor is shown in figure 6.12. A mercury drop is placed onto the surface of the crystal and positioned using a holder which is linked to an external influence through a lever arm.

Movement in the lever arm is translated into a displacement of the mercury drop above the waveguide. The drop is prepositioned above the waveguide such that the relatively linear region of the graph in figure 6.9 is utilized. A maximum travel of 0.7 mm, for the 2.2 mm drop, would be allowed with a typical resolution of 50 μm in mercury position. External influences may include temperature through thermal expansion, displacement and vibration through motion of the lever directly, pressure by connecting the lever to a diaphragm, stress, strain and many others.
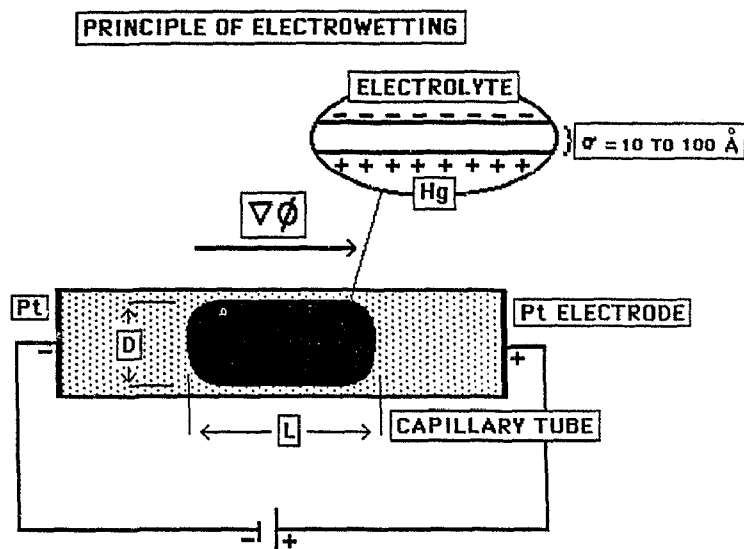
Figure 6.13: Principle of electro-wetting.

6.3.3 Electro-Optic Switch

An electro-optic switch can be designed using the principles of the mercury polarizer and the relatively new technique of electro-wetting[62-64] to move the liquid metal drop onto and off the waveguide. Electro-wetting effects are surface tension effects caused by shear forces tangential to the interface of two fluids. The wetting force is produced by surface tension variations along the interface. The principle of how the mercury drop's position is changed is best discussed using figure 6.13.

A capillary tube is filled with a liquid electrolyte and a small slug of mercury, the ends are sealed and contact is made to the electrolyte via platinum electrodes. Because a small gap separates the slug from the capillary walls, the electrolyte trapped in the gap has high electrical resistance. When a voltage is applied to the electrodes a voltage gradient appears across the trapped electrolyte in the gap even though the metal (Hg) is present. This can be explained by examining the mercury electrolyte interface more closely when no voltage is applied.

The insert of figure 6.13 shows that a positive charge has been absorbed by the mercury from the electrolyte and is counterbalanced by an equal negative

charge located between 10 and 100 $\overset{\circ}{A}$ away. The double layer of charge present at this interface allows the visualizaton of the interface as a parallel plate capacitor. The electrolyte is chosen so that the mercury- electrolyte interface is perfectly polarizable, thus no charge can migrate across the interface in the voltage range of interest. This effectively shields the electrolyte from the mercury.

When the voltage is applied and a potential gradient is present, the double layer of charge redistributes itself along the mercury-electrolyte interface. In a one dimensional model the voltage drop between the charge distribution at a particular location on the interface can be expressed as:

$$V(x) = \phi(x) - <\phi> -\phi_q \qquad (6.1)$$

where

$$<\phi> = \frac{1}{L} \int \phi(x) dx \qquad (6.2)$$

is the average potential on the mercury surface and $\phi_q = $ q/C, q being the charge per unit area present at the interface in the absence of an applied potential $\phi(x)$, and C is the double layer capacitance per unit area. In this model the surface tension is given by the integrated Lippman[65] equation:

$$\gamma(V) = \gamma_o - \frac{1}{2}CV^2 \qquad (6.3)$$

A surface tension gradient is established along the interface since V varies from point to point along the interface. Since the liquid has a tendency to minimize its free energy it would attempt to move towards the region of lower surface tension. The ends of the tube being sealed restrict the electrolyte's motion and therefore a force is applied to the Hg drop causing it to move towards the negative electrode. The voltage difference between electrodes requi ed to move the drop is in the order of a volt, which is well below the breakdown voltage of the electrolyte.
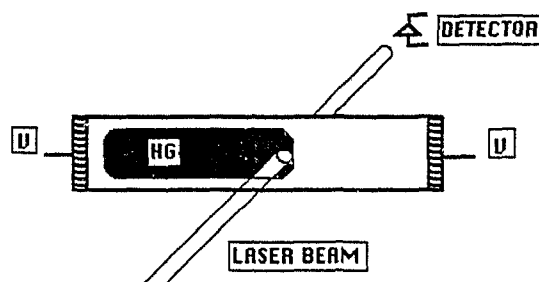
Figure 6.14: Orientation of the laser beam with respect to the mercury drop.

To study the performance of the electro-wetting principle, a capillary tube of 2 mm internal diameter was filled with a 0.1 molar H_2SO_4 solution. A small drop of mercury was inserted into the tube such that it was 3 mm in length. The ends of the tube were fitted with electrodes, sealed with silicon sealant and a laser beam was directed onto one edge of the mercury drop, as shown in figure 6.14.

A 10 Hz sinusoidal voltage, of 2 volts P-P amplitude, was applied to the electrodes and is shown in the upper trace of figure 6.15; the lower trace shows the recorded signal of the laser beam passing by the drop. The phase of the sinusoidal voltage was adjusted so that the beam was initially blocked.

The electro-optic switch using the electro-wetting principle to move the mercury drop is shown in figure 6.16. In this design the electrolyte-slug container is formed from a semicircular cutout of the capillary tube glued to the surface of the crystal using a silicon seal. The semicircular tube was manufactured by grinding off one side of a capillary tube, using the crystal polisher.

In the device design orientation, shown in figure 6.16, the mercury rests on the surface of the crystal and can interact with the waveguide when positioned above the guide. Optical fibres are used to couple light into and out of the waveguide enabling it to be interfaced to existing optical systems.

The operation of this device has been demonstrated in the lab by observing, on the monitor, the output light of the waveguide as the drop of mercury moved on
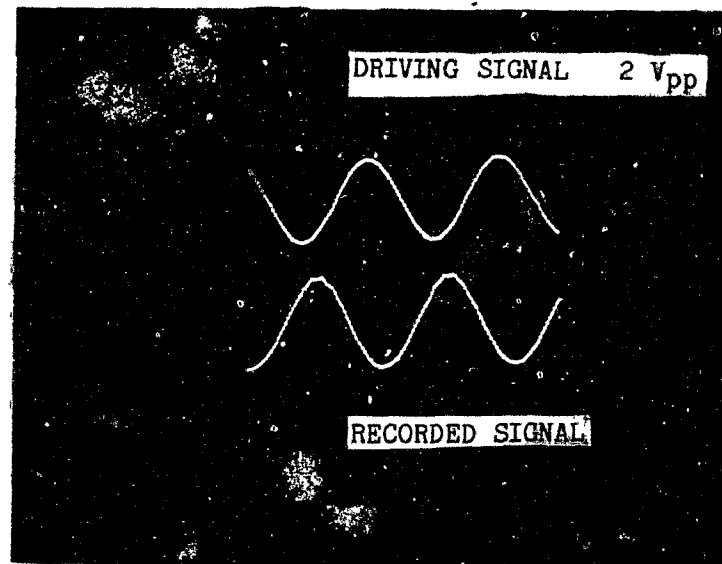
Figure 6.15: Electro-wetting principle verified, Upper trace - Applied signal, Lower trace - Modulated signal.

and off the waveguide through electro-wetting. The output power was observed to decrease when the drop was positioned above the waveguide and to increase again, returning to its original level, when the drop moved off.

Several problems have been identified which must be addressed before the device can find long term application in optical systems. After a few seconds of operation the drop has a tendency to migrate towards one of the electrodes, short out and no longer move. The proper design of the electrolyte tube would have to restrict the motion of the drop to the vicinity of the waveguide. Another problem encountered is contamination of the crystal and mercury surfaces when a voltage is applied to the electrodes causing electrolysis to take place. These areas were not investigated here since the clean room facilities required to work with mercury were not available.
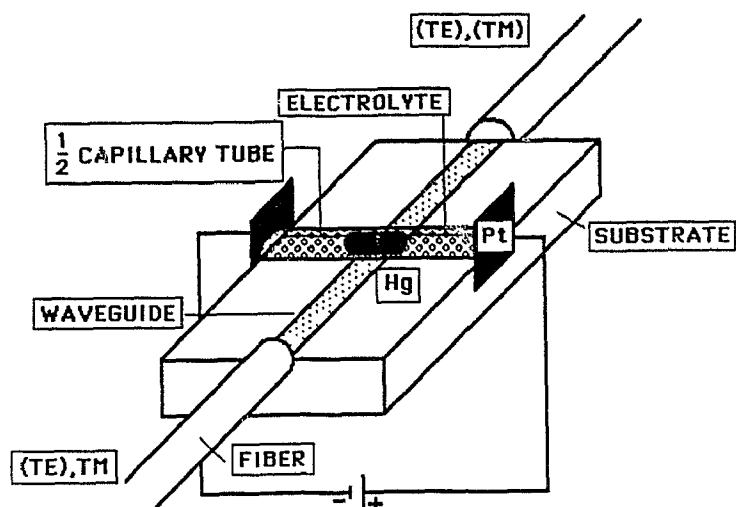
Figure 6.16: Voltage controlled integrated-optic polarizer switch.

6.4 Summary

In this chapter several methods of introducing polarized light into the active elements of integrated-optic devices have been discussed. In particular the effects of a metal layer of aluminum in contact with the waveguide has been investigated experimentally. The polarization properties of this configuration showed that the TM component is highly attenuated by the presence of the metal while the TE component is unaffected. Interactions of metal claddings with the waveguides are of particular interest in integrated-optics since the controlling metal electrodes must be placed close to the waveguide to ensure efficient device operation. As demonstrated here the electrodes may affect the waveguide propagation properties, introducing higher attenuations as well as polarizing the guided light. The metal claddings on the waveguides have fixed attenuation and polarization properties which cannot be altered interactively with device operation.

The use of mercury on the waveguide has been investigated experimentally and shown to possess the polarization and attenuation properties of the standard

evaporated metal cladding. Liquid mercury is an ideal choice for the cladding since it does not wet the crystal surface, forms a good contact with the waveguide, surface tension restores the drop shape on the crystal and it can be manipulated on and off the waveguide easily. These properties make the design suitable for applications where variable polarization and attenuation are required. Linking the position of the mercury drop to external mechanisms enables the basic properties of the polarizer to be employed in a number of sensor configurations. In particular, the designs of devices capable of liquid level and displacement measurements has been discussed.

In the final part of the chapter a novel electro-optic electro-wetting based attenuator/switch using mercury acting as a variable length cladding has been discussed. It was shown that only a few volts were required to translate the drop in the capillary tube. This design is TTL compatible and can serve to interface optical and electrical systems.

CHAPTER 7. ANISOTROPIC OFF-AXIS PROPAGATION

7.1 Introduction

The lithium niobate crystal substrate is anisotropic and contains a single optical axis where the ordinary and extraordinary indices of refraction are equal. As shown in appendix A, the propagation properties of guided modes in wave guide formed in this substrate depend on the angle of propagation with respect to the optical axis and that the modes are hybrid and contain both polarization components. An interesting property which is the emphasis of this chapter is the differential loss that exists between the ordinary and extraordinary modes which is a function of the angle of propagation with respect to the optical axis. Waveguides produced by titanium in-diffusion and the proton exchange process are investigated experimentally and the loss properties of the modes as they propagate off-axis are presented.

7.2 Investigation of Titanium In-Diffused Slab Waveguide

A graded index of refraction slab waveguide has been in-diffused from a 400 $\mathring{A}$ thick titanium layer into the optical grade surface of an X-cut crystal. This particular crystal cut is chosen so that off-diagonal elements will be present in the dielectric tensor and wave equation matrix for propagations at an angle ($\theta \neq 0, 90$ degrees) to the optical axis. These crystals are longer along the Z direction than the Y direction for orientation purposes and are cut along the principal axis to an accuracy of 3 seconds of arc.
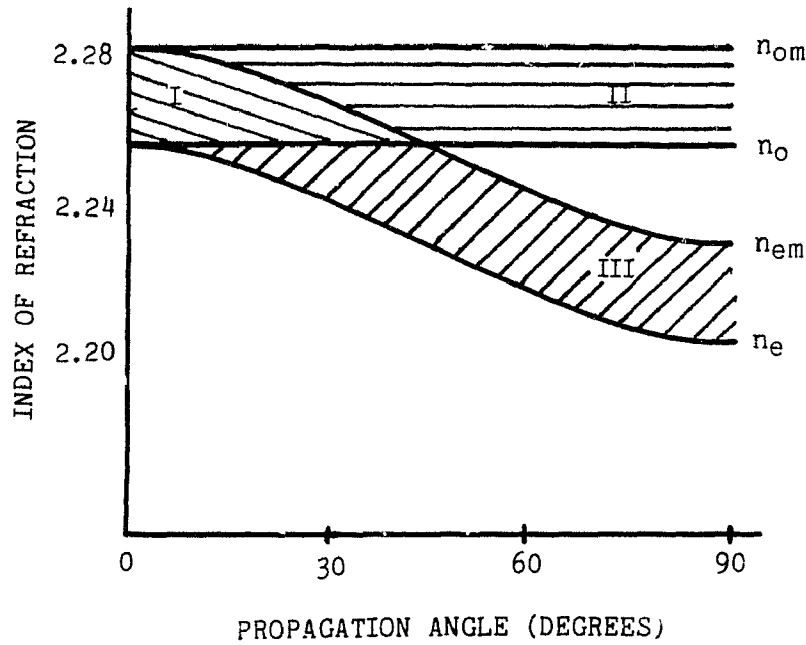
Figure 7.1: Index of refraction curves for the ordinary and extraordinary indices of the substrate and waveguides.

To begin the analysis of the above mentioned waveguide the substrate indices of refraction as a function of propagation angle for the ordinary and extraordinary profiles (n_o, n_e) are plotted in figure 7.1. Also shown in the figure are the profiles for the maximum of the ordinary and extraordinary graded waveguides $(n_{om}$ and $n_{em})$. The real component of the normalized propagation constants $(\frac{\beta}{k_o} = n_{eff})$ for the ordinary modes will lie between n_o and n_{om} while those of the extraordinary modes will lie between n_e and n_{em}. The ordinary and extraordinary modes are composed of TE (extraordinary) waves and TM (ordinary) waves due to the hybrid nature. As expected the extraordinary index curves of the substrate and waveguide vary as a function of the propagation angle and are expressed as:

$$n_{e(m)}(\theta) = \frac{n_{e(m)}n_o}{\sqrt{n_o^2 sin^2(\theta) + n_{e(m)}^2 cos^2(\theta)}} \tag{7.1}$$

In figure 7.1 three propagation regions have been indicated by (I, II, III)[66,67]. In region I the effective index for guided modes will be greater than both the or-

Figure 7.2: Ray optic model of modes in regions I, II and III.

dinary and extraordinary indices of the substrate. The components of such modes may be represented in the ray optic model of figure 7.2a. Both the ordinary and extraordinary waves are coupled at the interface thus satisfying the boundary conditions. In this region of propagation the rays travel a maximum distance in the waveguide given by x_{te} and x_{to} before turning back towards the top surface.

In region II, only the ordinary mode is guided and its ordinary wave component follows a path similar to that in region I. The extraordinary wave component on the other hand is evanescently coupled to the upper interface and is required to satisfy the boundary conditions.

In region III, the extraordinary mode is guided by the waveguide and its extraordinary wave component follows a path similar to the extraordinary wave in region I. The ordinary wave, however, is phase matched to a substrate mode and the component generated at the interface, due to boundary requirements, will refract away from the guide region and couple into a leaky substrate mode.

Analysis[69,70] have shown that the size of the ordinary wave component generated for a propagating extraordinary mode in region III depends on the angle of propagation and waveguide parameters. The field amplitude ratio describing the conversion from an upward propagating extraordinary wave $(E_{ye}^{+}(0))$ to a downward

propagating ordinary $(E_{yo}^-(0))$ wave is:

$$\frac{E_{ye}^+(0)}{E_{yo}^-(0)} = 2\sqrt{\frac{\gamma_o}{\gamma_e}}(1 + \frac{k_o^2 n_o^2 tan^2(\theta)}{\gamma_o \gamma_e})^{-1} \qquad (7.2)$$

where γ_o and $\gamma_\cdot$ are given by equations (A.8a) and (A.8b) respectively. Since the downward propagating ordinary wave does not return to the top surface, a new component must be generated each time the extraordinary wave returns to the top surface. Leakage of the ordinary wave into the substrate bleeds power from the guided mode, attenuating the extraordinary mode.

The leaky mode loss coefficient is defined analogously to the optical absorption coefficient $[P = P_o\, e^{-\alpha z}]$. The power per unit length in z is identified with that power carried by the ordinary wave which leaks out of the bottom of the waveguide. The loss coefficient is expressed as[68-71]:

$$\alpha = \left(\frac{2\gamma_{os}\gamma_e^2}{k_o n_{eff}(x_{tc} + \frac{1}{\gamma_{es}})}\right)\left(\frac{\gamma_{os}^2 + k_o^2 n_o^2 tan^2(\theta)}{(\gamma_{os}^2 \gamma_e + k_o^2 n_o^2 tan^2(\theta))^2}\right) \qquad (7.3)$$

where

$$\gamma_{os} = k_o\sqrt{n_o^2 - n_e^2 - 2n_e(\theta)(n_{eff} - n_e(\theta))} \qquad (7.4)$$

$$\gamma_{es} = \frac{n_z}{n_o}k_o\sqrt{2(n_{eff} - n_e(\theta))n_e(\theta)} \qquad (7.5)$$

Identifying n_{eff} as the real part of the propagation constant and α as the attenuation coefficient, the propagation constant with both real and imaginary terms can be expressed as[69,72]:

$$\beta = k_o n_{eff} - \frac{i\alpha}{2} \qquad (7.6)$$

Figure 7.3 demonstrates an important effect for off-axis propagations. There exists a critical propagation angle, θ_c, where the loss coefficient increases dramatically $(\frac{d\alpha}{d\theta} \approx \frac{20}{cm\cdot rad})$. In figure 7.1 this corresponds to a point where the mode's effective index intersects the boundary between regions I and III. For propagation
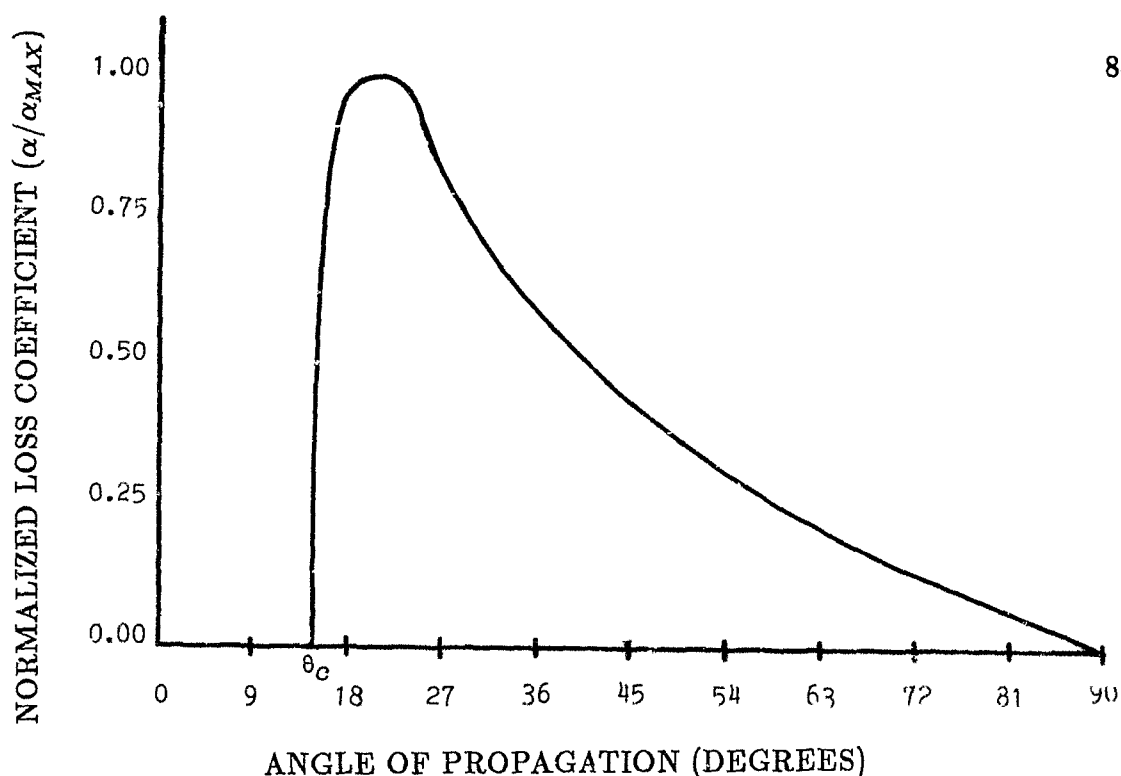
Figure 7.3: Loss coefficient as a function of propagation angle for extraordinary mode.

angles less than the critical angle the extraordinary mode does not lose power due to leakage since the ordinary wave returns to the surface fulfilling the boundary conditions as shown in figure 7.2a. For propagation angles less than the critical angle, the extraordinary mode does not lose power due to leakage since the ordinary wave returns to the top surface fulfilling the boundary conditions as shown in figure 7.2a. For angles of propagation slightly larger than the critical angle, losses increase very rapidly to maximum due to the leakage of the ordinary wave into the substrate. At even larger propagation angles, the required size of the ordinary wave at the interface, to satisfy the boundary condition, is smaller and as a result the leaked component to the substrate is reduced. In the figure this leads to a reduction in the size of the loss coefficient as the propagation angle is increased. At 90 degrees to the optical axis no loss is observed due to leakage since the ordinary wave is no longer required for an extraordinary mode.
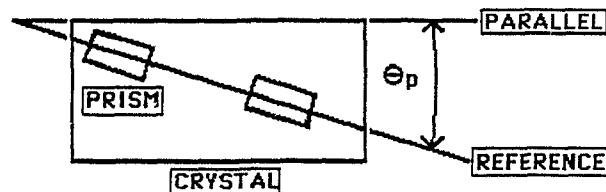
Figure 7.4: Propagation angle measuring geometry.

7.2.1 Experimental Investigation of the Dispersion Curves

Effective indices for the ordinary and extraordinary modes supported by the slab waveguide are measured using the prism coupling setup described in section 5.1. The input laser beam is polarized in the TE plane of the waveguide for extraordinary mode excitations, and in the TM plane for ordinary mode excitations. Prism coupling angles have been obtained by measuring the angle, the input beam forms with the normal to the prism's input surface. This requires two readings of the lower rotational stage. The first reading is the reference and consists of noting the micrometer value when the beam is reflected directly back onto itself from the input face of the prism. The second reading consists of launching the mode into the guide by rotating the prism and crystal and once again recording the micrometer value. The difference between these two values provides the coupling angle. The lower stage provides an accuracy of 1 minute of arc but due to the width of the laser beam, errors of 10 minutes of arc are typically observed.

Mode propagation angles, with respect to the optical axis, are obtained using a second rotational stage which allowes the crystal to be rotated in the plane of the slab waveguide. Figure 7.4 shows the geometrical arrangement for obtaining these readings.

The reference angle was obtained by reading the upper rotational stage when the laser beam was reflected back onto itself from the prism's input face. A second angle reading was taken by rotating the prism and crystal such that the laser beam

was directed parallel to one edge of the crystal. To obtain this reading accurately, the beam is divided in two. One beam is reflected from the crystals edge, generating a reflected spot on a screen, while the other is allowed to pass uninterrupted, generating a direct spot on the screen. Rotating the crystal such that the two spots coincide ensures that the beam propagates parallel to the edge of the crystal. The difference between the back reflected reference reading and the reading when the beam propagates parallel to the crystal edge provides the propagation angle of the guided mode.

The dispersion curves for the two observed extraordinary modes are calculated from the prism coupling data and plotted as a function of the propagation angle in figure 7.5. Also shown on this curve are the ordinary and extraordinary bulk indices of the substrate, measured by finding the coupling angle to the first substrate mode. At various coupling angles both TE and TM polarized output m lines are observed on the screen using an output prism in the arrangement of figure 5.2.

The extraordinary modes in the waveguide structure show the angle variation of the effective index and correspond to the modes which are guided modes in region I and the leaky modes in region III. The nature of the leaky modes should experience an angle dependent loss coefficient similar to that shown in figure 7.3. The nature of the guided and leaky modes is examined by observing the output light from the edge of the waveguide. A series of photographs of this light for various propagation angles is included with a loss curve in figure 7.6.

For propagation close to the critical angle, the TM component is photographed, since this component displays the leaky behaviour of the mode, while the TE component is too weak above θ_c. For a propagation angle of 16 degrees $(\theta \approx \theta_c)$, photograph A of figure 7.6, the TM component is guided in the slab waveguide as confirmed by the guided light observed at the crystal-air interface. Close examination of the photograph shows a low intensity streak directly below the guided light
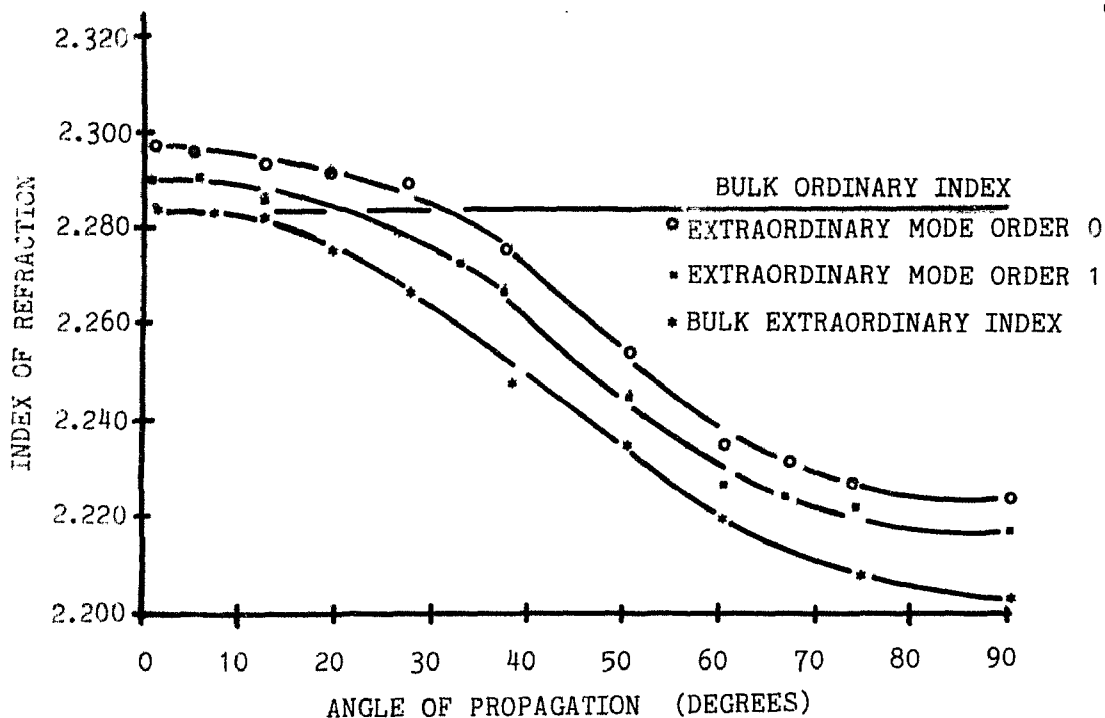
Figure 7.5: Dispersion curves for the observed extraordinary modes.

and corresponds to the leakage of TM light into the substrate.

For the propagation angle of 17 degrees, photograph B in figure 7.6 shows that the substrate coupled light has become stronger with a corresponding reduction in intensity of the guided light. In the loss curve figure, this propagation angle corresponds to a position on the rising edge of the loss curve.

For the propagation angle of 18.5 degrees, photograph C in figure 7.6 shows only leaky light in the substrate and no guided light. This propagation angle corresponds to a position higher up on the rising edge of the loss curve than in B due to the absence of guided light.

From the sequence of photographs it is observed that the position of maximum intensity of the substrate light moves further away from the top edge of the crystal with increased propagation angle. With the use of figure 7.7, the position of highest intensity can be geometrically related to the effective index of the leaky
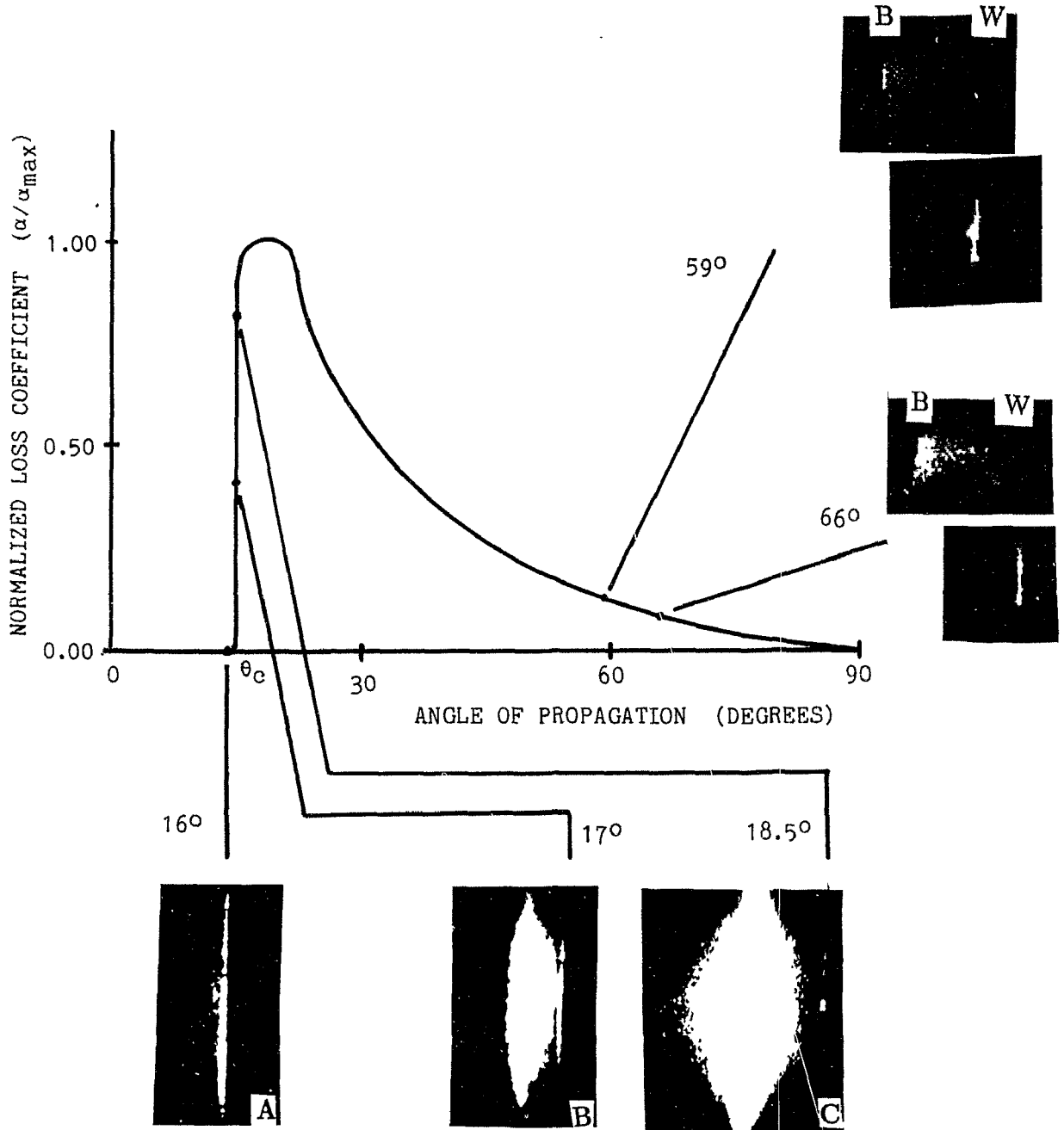
Figure 7.6: Experimental investigation of the extraordinary loss curve, W - waveguide edge, B - lower edge.
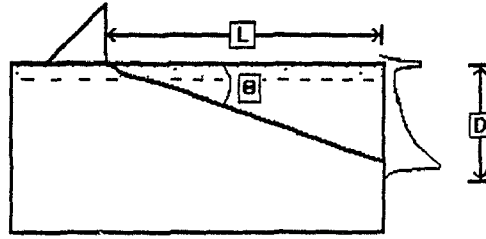
Figure 7.7: Phase matching between ordinary and substrate mode.

mode through:

$$n_{eff} = n_o cos(\theta) \tag{7.7}$$

This expression stresses the phase matching that occurs between the ordinary wave and the substrate mode. As the propagation angle is increased, the effective index for the extraordinary mode decreases and phase matches to a substrate mode of larger angle[71-73]. This results in the observed light on the end of the crystal moving away from the waveguide surface as the propagation angle is increased.

Photograph C shows that the loss coefficient for the 18.5 degree propagation angle can be obtained. From geometrical considerations the width of the pattern at the edge of the crystal (D) can be related to a leakage length (L), as shown in figure 7.7, by the expression D $tan(\theta) = $ L. The angle θ can be obtained from equation (7.7), since n_{eff} and n_o are known.

When taking this photograph, using the video camera with 40 dB dynamic range, the propagation angle was adjusted until no TM light from the waveguide was observable. Thus the ratio of the input power P to the output power P_o can be taken as 10^{-4}, and α can be evaluated from:

$$P = P_o e^{-\alpha L} \tag{7.8}$$

and upon rearrangement becomes:

$$\alpha = \frac{4}{D} tan(\theta) ln_e(10) \tag{7.9}$$
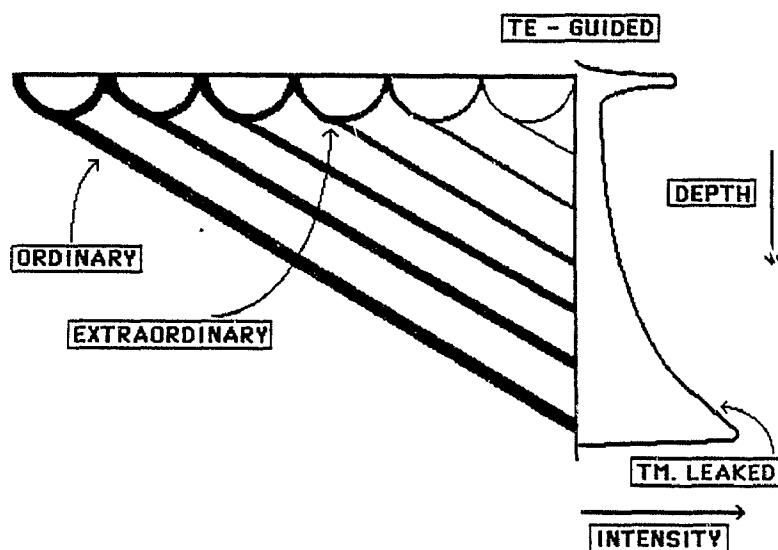
Figure 7.8: Nature of the leaked TM light.

Inserting the measured values for D = 3/5 mm and θ = 2 degrees, the attenuation constant is α = 5 cm^{-1}.

In the high angle regime of figure 7.6, the TE and TM output polarized components are photographed for propagation angles of 59 and 66 degrees. A TE component is now observed in the waveguide since the extraordinary to ordinary wave conversion at the interface diminishes and is smaller at these propagation angles. The two photographs of the TM component show that light is coupled to the substrate and the intensity increases with distance from the waveguide/air surface. This nature of TM light can be explained using figure 7.8. The further the light is observed from the top surface of the crystal, the closer to the input end of the waveguide the ordinary component is generated. Since the extraordinary wave is attenuated as it propagates, the ordinary component generated at the surface will decrease in strength as it is created further down the waveguide. This results in an increase in the TM component intensity with increased distance from the top surface.

We have seen in this section the nature of the extraordinary modes as they

propagate off-axially in titanium in-diffused waveguides and several interesting features have been shown experimentally. A new technique for producing waveguides, subject of the next section, makes use of the proton-exchange process and drastically alters the waveguide parameters discussed above for off-axis propagations.

7.3 Investigation of Proton Exchanged Single-Mode Slab Waveguide

Proton exchanged waveguides are produced by replacing lithium ions of the crystal with hydrogen ions present in a molten bath of benzoic acid. This process increases the extraordinary index while decreasing the ordinary index wherever the exchange takes place[74]. Slab waveguides have been produced in X-cut crystals following the steps outlined in chapter 4. The X-cut crystal is chosen for the substrate, as for the titanium in-diffused waveguides, so that off-diagonal elements will be present for propagations not along or perpendicular to the optical axis. The indices of refraction for the bulk LiNbO$_3$ and maximums of the exchanged layers are shown in figure 7.9.

The ordinary indices of refraction are angle independent and are displayed by the horizontal dashed lines in the figure. Ordinary modes cannot be supported in this structure since the maximum of the exchanged layer is less than the bulk ordinary index. For the extraordinary bulk index the angular dependence is given by equation (7.1). The proton-exchanged maximum of the extraordinary index follows a curve given by:

$$n_{em}(\theta) = \frac{n_{em}n_{om}}{\sqrt{n_{om}^2 sin^2(\theta) + n_{em}^2 cos^2(\theta)}} \qquad (7.10)$$

This expression is similar in appearance to equation (7.1) with n_o replaced by n_{om}. This substitution can be accounted for by redrawing the index ellipsoid of figure 2.2, with n_{om} and n_{em} replacing n_o and n_e respectively.

In figure 7.9 three region have been identified. Regions I and III are similar
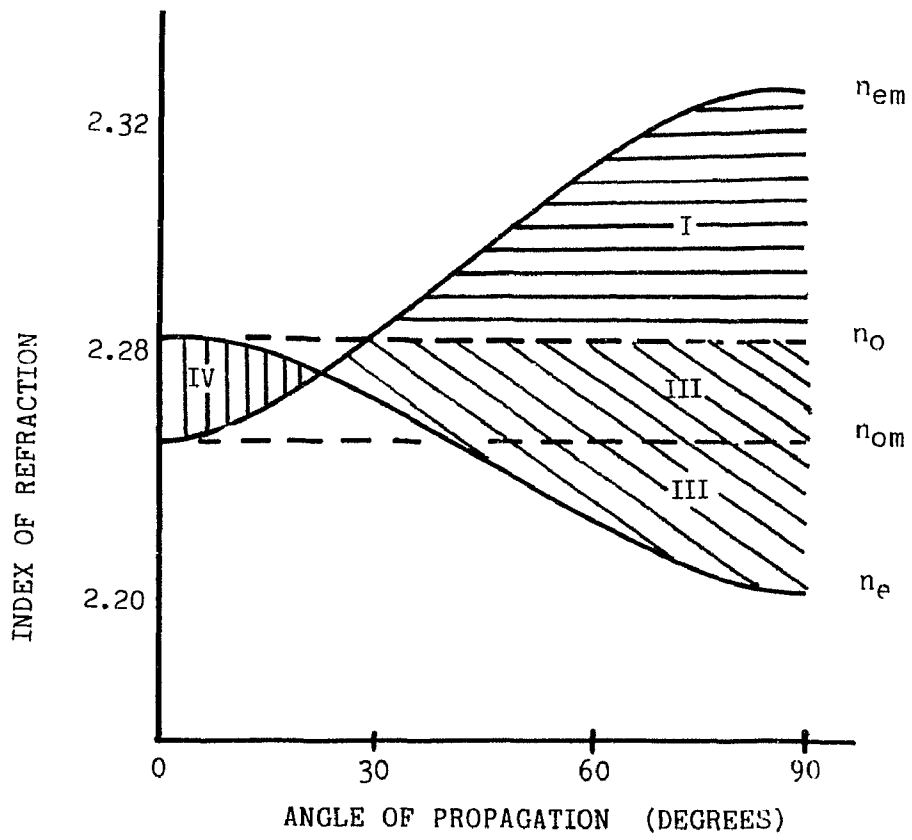
Figure 7.9: Angular dependence of bulk and maximum indices for the exchange process.

to those of the titanium in-diffused waveguide (figure 7.1) for extraordinary modes only. The previous discussion of guided and leaky modes is also valid in these regions for the proton exchange waveguides. For these waveguides the leaky mode loss coefficient has been recalculated[74] and is shown to be similar to that shown in figure 7.3. For these waveguides the critical angle, θ_c, can be increased considerably approaching 90 degrees for the lowest order mode when the waveguide parameters are carefully chosen. Below the critical angle the waveguide is cut off[74] and the attenuation coefficient is regarded as infinite since the extraordinary mode also leaks away. There is no region II since ordinary modes are not guided. The additional region IV stresses the fact that modes cannot be guided at small angles to the optical axis.

The proton exchanged slab waveguide is investigated using the prism coupling setup described in chapter 5. The input polarization of the He-Ne laser is set along the TE plane of the waveguide since only the extraordinary modes are guided. Through prism coupling observations the slab is found to be single mode. The effective index versus coupling angle curve for the lone mode is shown in figure 7.10. The data points marked with a circle represent experimentally calculated points from prism coupling data. The lower line is the angular dependence of the extraordinary bulk substrate index and points marked by stars are calculated by measuring the angle that excites the first extraordinary substrate mode.

For the propagation direction perpendicular to the optical axis, $\theta = 90$ degrees, the mode is confined to the slab waveguide and no leaky light is observed. At this particular angle the extraordinary and ordinary waves are uncoupled since there are no off-diagonal elements in the dielectric tensor. This completely relaxes the requirement of an ordinary wave to satisfy the boundary condition and as a result no leaky component is generated.

For angles of propagation other than 90 degrees, but greater than 83 degrees, losses of guided light have been observed to increase rapidly with the decrease in
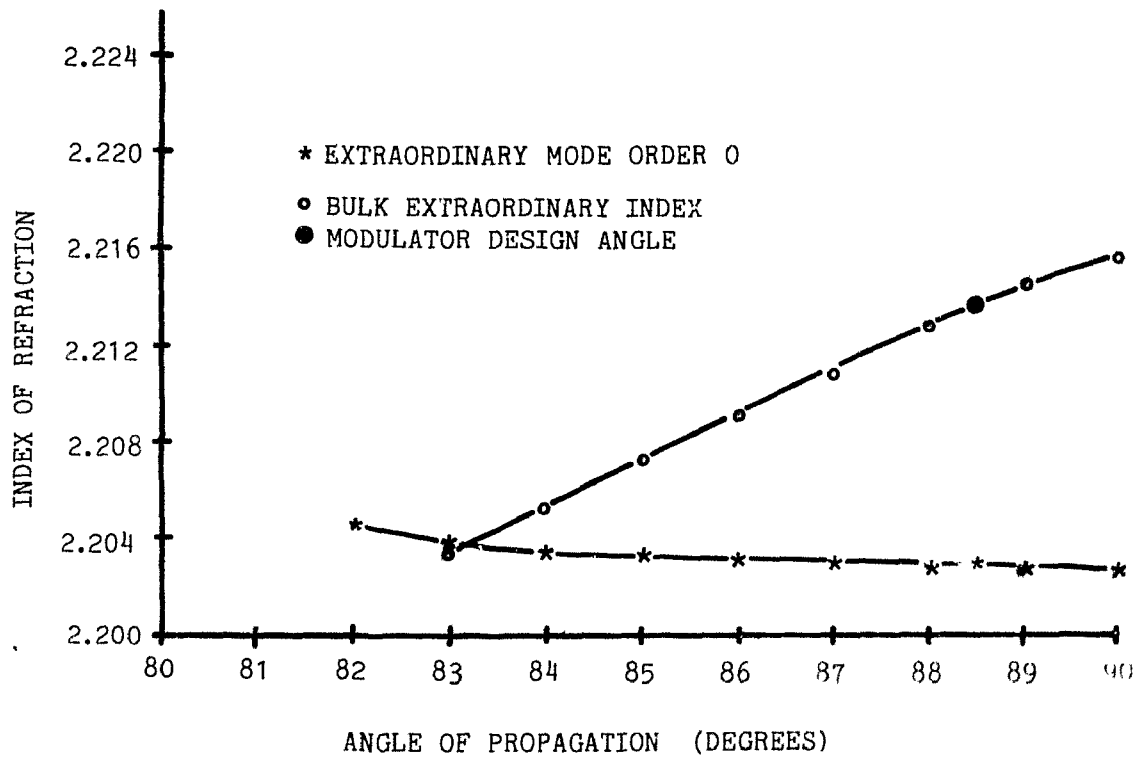
Figure 7.10: Effective index versus propagation angle for observed extraordinary mode.
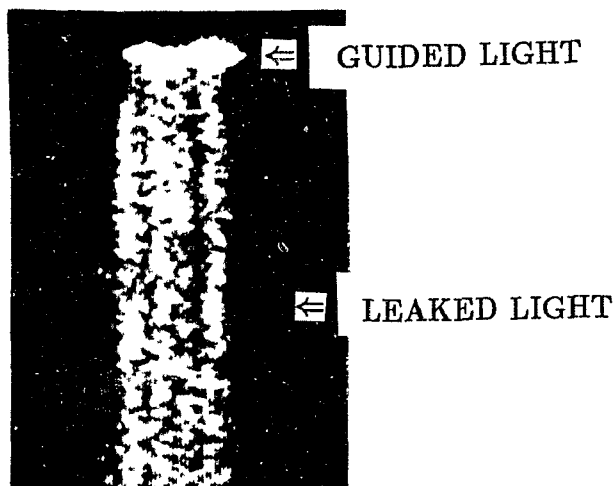
Figure 7.11: Guided and leaked light of the proton exchanged slab waveguide.

propagation angle. This observation is made by recording the strength of the leaked light and guided light from the end of the crystal. Figure 7.11, shows a photograph of both the TE and TM components observed at $\theta = 88.5$ degrees with the output coupling prism removed. The bright line across the top edge corresponds to the guided light of the slab while the light under that edge is the leaky component. As the propagation angle is increased or decreased so is the intensity of the guided light, with the opposite effect observed for leaky light.

For angles less than 83 degrees, no guided or leaky light was observed and the waveguide mode could no longer be excited. The sudden decrease in the loss coefficient close to the critical angle does appear to follow the theoretically predicted curve of figure 7.3 with $\theta_c = 83$ degrees, provided that only the strength of the leaky light is observed. Observing the attenuations of the guided light, on the other hand, produces a loss curve that shoots to infinity at θ_c since the extraordinary wave is coupled to substrate modes and leaks away before any ordinary component is generated.

In this section we have seen that the critical angle can be drastically increased and that only extraordinary modes can be guided in proton-exchanged waveguides.

These properties, combined with those of titanium in-diffused waveguides, can be used as a basis for a number of integrated-optic devices.

7.4 Device Applications of the Off-Axis Propagations

Several passive and active devices can be designed around the peculiar behaviour of the off-axis propagation of the modes in the anisotropic waveguides. A description of several passive devices is given below along with the design and experimental observations of the active devices. The complementary device design nature of the two waveguide forming techniques are highlighted by showing that devices which seem impractical using one technology are practical using the other.

7.4.1 Mode Selector

Devices of this type make use of the propagation constant β and the nature of the waveguide profile. To select only the ordinary modes an in-diffused waveguide can be formed in the X-cut crystal. By launching the light at an angle to the optical axis such that the extraordinary mode leaks into the substrate, only the ordinary modes will exit and guide with low losses. Contrarily, to select only the extraordinary modes a proton-exchanged waveguide can be used since this supports only the extraordinary modes. In this waveguide the propagation angle and exchange parameters can be chosen such that the extraordinary mode is guided without any leaky losses.

7.4.2 Polarizer and Polarization Rotator

Devices of this type are possible due to the presence of the off-diagonal elements in the dielectric tensor. To convert light in the TE plane to the TM plane of the waveguide, a titanium in-diffused or proton-exchanged waveguide can be used.

Launching the extraordinary mode slightly above the critical angle, θ_c, will result in TM polarized light in the substrate which can be monitored and manipulated further if required. To convert light from the TM plane to the TE plane of the waveguide requires the use of a titanium in diffused waveguide where the ordinary mode is launched. Since this mode contains both polarization states for $\theta \neq 0$ or 90 degrees, an output prism can be used to separate the polarizations. Of course, any device which can separate polarizations can also be used as a polarizer.

7.4.3 Modulator/Attenuator/Switch

For these devices the propagation constant, $\beta = \beta_r + i\beta_i$, and electro-optic effect are exploited in the device design. Based on the loss curve of figure 7.3 and the similar curve for the proton exchange waveguide, devices can be designed about the low angles, where $\theta \approx \theta_c$, and at higher angles to the optical axis, where the loss curve has a negative slope.

Design about θ_c for Titanium In-Diffused Waveguides:

In this angle region and waveguide making technique, the following design features must be considered:

- Small changes in angle can cause large changes in the loss coefficient, $\frac{\gamma\alpha}{\gamma\theta}$ is large and given by the slope of the loss curve.

- The device can have a relatively low inherent loss by choosing $\theta \leq \theta_c$.

- The electro-optic effect is reduced since $\sin(\theta) \approx 0.1, 0.2$.

- Angular alignment of the electrodes must be within .5 of a degree in order to guarantee the operation position on the loss curve.

- The critical angle is highly dependent upon waveguide parameters and mode order, thus in-diffusion variations from waveguide to waveguide will result in device reproducibility difficulties.

Devices have been designed to operate about θ_c based on various waveguide models[75,76] by treating the electro-optic effect as a perturbation on the waveguide.

Results indicate that applied electric fields of ±3 to ±5 volts/μm would be required to achieve a 90% modulation depth for a cm interaction length, where modulation depth is defined as:

$$modulation \quad depth = (1 - P_{min}/P_{max})X100\% \qquad (7.11)$$

A device reported by Yamamoto[75] was shown operating in this region with an 80% depth of modulation for 2 volts/μm applied electric field.

Design about θ_c for Proton-Exchanged Waveguides:

For waveguides formed from the proton exchange process, designing and operating devices about the critical angle is impractical. For propagation angles below the critical angle, the extraordinary mode is not guided. At or slightly above the critical angle the losses are very high due to the strong coupling of power into the ordinary wave which leaks away.

High Angle Region, Titanium In-Diffused Waveguides:

For devices based on the titanium in-diffused waveguides, the following design considerations can be deduced from the loss coefficient curve:

- Large changes in the angle of propagation are required to cause an appreciable change in the loss coefficient.

- Devices will always contain losses due to the leaky mode component generated in this region of propagation.

- The electro-optic effect is relatively strong since $\sin(\theta) \approx 0.8, 0.9$.

- Careful alignment of the electrodes with the desired propagation direction is relaxed somewhat since the slope of the loss curve is not as steep as that about the critical angle, θ_c.

- Waveguide parameter fluctuations caused during manufacture have less effect on the shape of the loss curve at these high angles of propagation. As a result, device reproducibility will be better than that of devices built about the

critical angle.

Devices can be designed in this region for titanium in-diffused waveguides, but the relatively small change in loss coefficient with large changes in angle will make such a device inefficient. In this region of propagation it is better to design devices based on the proton exchange waveguides which have shown experimentally that large increases in the loss coefficient for small changes in angle are possible. Such a device has been designed, built and tested using a proton exchange waveguide and is discussed in the remainder of this chapter.

High Angle Region, Proton-Exchange Waveguide:

The completed device, shown in figure 7.12, is built from the X-cut crystal with proton-exchanged single mode waveguide discussed in section 7.3. In order to minimize the inherent losses of the propagation, a direction of 88.5 degrees to the optical axis is chosen. Electrodes have been formed by carefully orienting a 100 μm diameter wire parallel to the chosen propagation direction and then evaporating a film of aluminum onto the exposed surface of the crystal. Removal of the wire results in a pair of electrodes with a 100 μm separation extending over the full length of the crystal. To accommodate the input and output coupling prisms, the aluminum is etched down to 1 cm in length in the centre of the 3 cm long crystal. The input and propagation angles of the TE polarized laser beam with respect to the waveguide and prism's input face are adjusted until the guided light propagates between the electrodes; this is confirmed visually.

To evaluate the behaviour of the device qualitatively, a video camera fitted with a 40 X microscope lens is focused onto the waveguide edge of the crystal. As the applied voltage to the electrodes is increased, the guided light decreasesd in intensity, corresponding to a translation of the loss curve towards higher angles. It is also observed that the accompanying leaky-mode light streak, located directly below the guided light, increases in intensity confirming that the guided-to-leaky-mode conversion has increased. The opposite effect is observed when the voltage
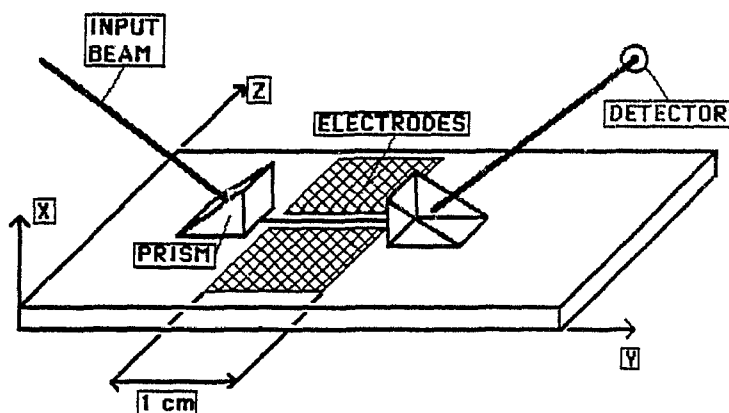
Figure 7.12: Design of the proton-exchanged leaky mode modulator.

was returned to zero. Quantitative measurements on the device have been made using a 0 to 150 volt A.C. signal (D.C. offset by 75 volts) applied to the electrodes and the light from the output prism measured using a photodetector at slow speed ($<$ 10 Hz). Figure 7.13, shows the modulating input potential (upper trace) and the modulated light level (lower trace). The 8 dB change in output optical power for this applied voltage signal translates into a modulation depth of 84 %.

7.5 Summary

In this chapter the presence of the dielectric anisotropy of the crystal substrate has been observed to completely alter the propagation properties of the waveguide modes. The off-diagonal elements in the wave equation, generated by the dielectric tensor, produce a coupling between the two polarization states and the waveguide modes are no longer simply TE and TM in nature but contain both components. For propagation directions along the principal axis, or in the (X,Y) plane, the modes can be pure TE and TM and the treatment of isotropic waveguide can be employed.

Cross coupling of the two polarizations, for off-axial propagations leads to

DRIVING SIGNAL ($150\ V_{pp}$)

RECORDED SIGNAL (8 dB CHANGE)
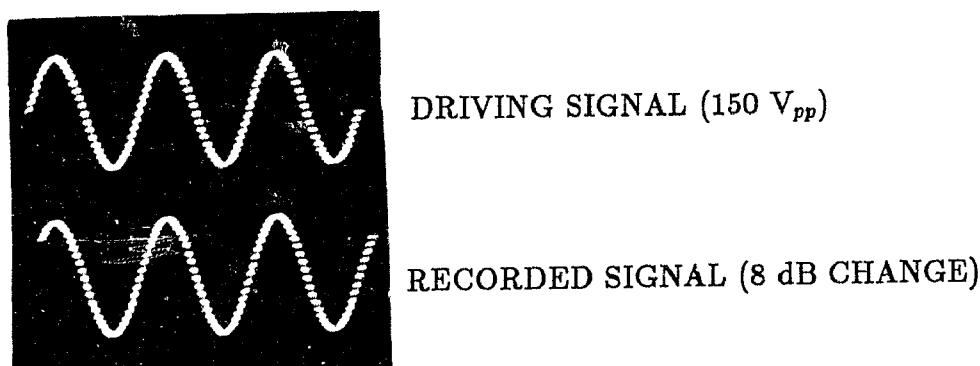
Figure 7.13: Output characteristics of the device at 10 Hz.

losses for the extraordinary mode when the effective index of the mode drops below the bulk ordinary index of the substrate. For titanium in-diffused waveguides it is predicted theoretically and observed experimentally that the loss coefficient increases very rapidly at the critical angle. For small increases in the angle about the critical angle, the guided output power drops rapidly and the attenuation coefficient can be as high as $100\ cm^{-1}$. In the high angle region the loss decreases with increased propagation angle and has been confirmed by observing both TE and TM polarized light from the end of the waveguide. For the single mode proton-exchange waveguide the losses of the guided mode are observed to increase very rapidly as the propagation angle is reduced from 90 degrees to the optical axis. It is observed that at the critical angle the leaked ordinary component reduces in power as predicted theoretically but occurs only because the extraordinary mode is no longer guided and coupled to a substrate mode. For both types of waveguides, titanium in-diffused and proton-exchanged, the leaky light is TM polarized in nature while the remaining guided light is TE, as expected for the ordinary and extraordinary waves of the anisotropic substrate.

The single mode proton-exchange waveguide has been configured into a modulator design by orienting electrodes at an angle of 88.5 degrees to the optical axis.

Input and output prisms are used to couple light to and from the waveguide. Orienting the electrodes at such an angle enables full use of the electro-optic effect and a depth of modulation of 84 % is observed for a field of 1.5 V/μm.

CHAPTER 8. GAPS IN WAVEGUIDES

8.1 Introduction

This chapter examines the lowest order mode power coupling properties of fi-
bre to integrated-optic waveguides and gaps in otherwise continuous channel waveg-
uides in LiNbO$_3$. Situations such as this may occur when waveguide interconnec-
tions are attempted[1] or when the results of the photolithography are imperfect and
produce broken waveguides. In the first part of this chapter, details of the radiation
mode based power coupling theory and the developed expression of Appendix C are
presented. The complexity of the expressions require a large number of calculations
for a single set of waveguide parameters to generate the power coupling informa-
tion. An alternate, simplified model has therefore been developed and is found
to generate power coupling versus gap length information which agrees well with
experimental results. In the next section the power coupling results from a launch
fibre into an integrated-optic waveguide are discussed. Afterwards, experimental
results on power coupling across gaps in LiNbO$_3$ waveguides are presented. The
integrated-optic device design of appendix D is built from the LiNbO$_3$ waveguides
and is shown to alter the power coupling across the gap.

8.2 Radiation Modes - Coupling Theory Results for Gaps

In a detailed treatment of radiated power from the ends of waveguides, con-
ventional methods using Kirchhoff's integral, based on the scalar wave equation, are

---

[1]Interconnections between single mode fibres, fibre to integrated-optic waveguides and
semiconductor lasers.
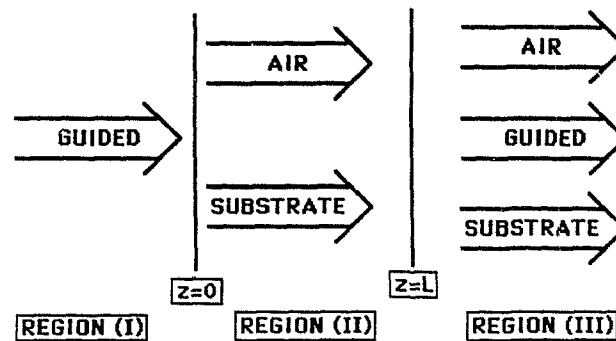
Figure 8.1: Modes considered in each region.

not applicable since the widths of the waveguide channels are comparable to the wavelength of light and the propagating modes can be formed from coupled polarized components[77]. There are, however, two general methods for solving Maxwell's equations for the total radiated fields from small waveguides: the Green's function method and the modal eigenfunction method[78]. The Green's function method is best suited for obtaining far field radiation information, while the modal method determines the radiation field everywhere in the structure. For the short gaps in waveguides studied here the modal field method must be employed. Full development of the coupling theory based on radiation modes can be found in Appendix C; a summary is given here.

Figure 8.1 illustrates the various modes that can propagate in each region and are considered in developing the power coupling expression. In region (I) guided modes only are treated, while in region (II) air and substrate modes are of interest. In region (III) guided, substrate and air modes may be present.

In the input waveguide segment, region (I), the wave mode propagates towards the (I)-(II) interface at $z = 0$. There it radiates into the gap region (II) where it encounters the (II)-(III) interface and is partially reconverted into guided modes. The interface between regions (I)-(II) and regions (II)-(III) determines to a large extent the coupling into and out of various modes in region (II) and the transmis-

sion of power through the structure. The power coupled into the same launch mode of region (I), in region (III), is expressible as:

$$P = G_m G_m^*$$ (8.1)

The $G_m G_m^*$ term is a normalized transfer function due to the presence of the gap. The power coupled to the receiving waveguide can be expressed as four terms:

$$P = T_s + T_a + T_{sa} + T_{as}$$ (8.2)

The term T_s represents power from the input waveguide converted to substrate modes in the gap region and then coupled back to the same guided mode in region (III). The term T_a is the power term which represents power from the input waveguide converted to air modes and then coupled back to the guided mode in region (III). The terms T_{sa} and T_{as} represent interactions (phase interference) between the various modes [2]. When a mode of different order (n) is coupled to region (III) expression (C.12) can be used, provided G_m is replaced by G_n at its first occurrence.

In region (III), the possibility of exciting substrate and air modes across the gap also exists since any power not coupled to the guided modes must be accounted for. The coupling coefficients to the substrate and air modes can be expressed as G_s and G_a respectively and the power coupled expressions are of the form (C.12).

8.3 Simplified Coupling Theory Across Gaps

Figure 8.2 shows the geometrical arrangement of the waveguides with a gap present and is used to develop a simplified coupling model.

The waveguide segment of region (I) acts as a source and radiates power into gap region (II). The radiated power profile of region (II) is modeled here to

---

[2] The full expansion of each T_i term is included in Appendix C.
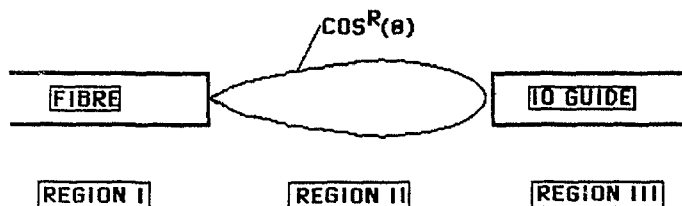
Figure 8.2: Simplified coupling model for fibre and integrated-optic waveguide.

a $\cos(\theta)$ function raised to the Rth power. The exponent, R, reflects the degree of directionality of the source's radiated power and is obtained from the numerical aperture using the following relations:

$$I(\theta_m) = 0.05I_o = I_o cos^R(\theta_m) \qquad (8.3)$$

and

$$NA = sin(\theta_m) \qquad (8.4)$$

The power coupled to the receiving waveguide of region (III) is calculated from the geometrical intersection of the waveguide's entrance aperture and the radiation profile of the source.

For waveguides contained in the LiNbO$_3$ substrate, an interface in region (II) is included in the coupling model as shown in figure 8.3.

The crystal-air interface is taken into account by reflecting the source waveguide, imaging[79,80], across the interface as shown. The power radiated by this image waveguide is opposite in sign when compared to the original source. The justification for change of sign rest in treating the original guide and image guide as one waveguide with twice the width and the interface removed. The mode guided in this total waveguide must be such that when the interface is reinserted and the
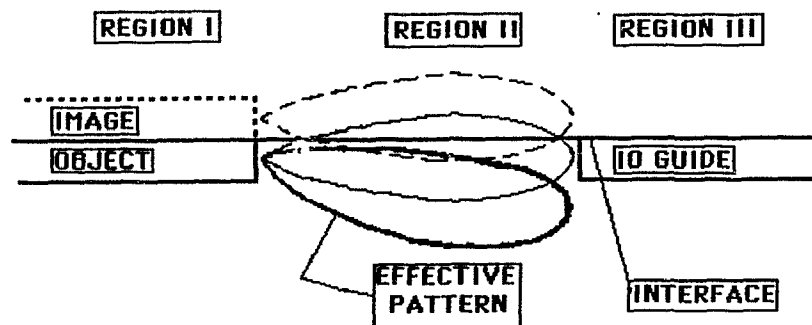
Figure 8.3: Integrated-optic LiNbO$_3$ gap geometry.

image guide removed the electric field profile remaining in the original source guide with gap resembles the original mode excited. The power coupled to the receiving waveguide can then be calculated from the new radiation profile. When the radiation profiles of the two source waveguides are added together the net radiation profile in the substrate has its maximum pushed away from the crystal-air interface, figure 8.3.

8.4 Coupling from Input Fibre to Integrated-Optic Waveguide

Coupling to integrated-optic channel waveguides is best achieved using a single mode or polarization preserving fibre with a core size similar to that of the integrated-optic waveguide. As discussed in chapter 5, the cleaved fibre is carefully aligned to the polished end of the integrated-optic waveguide using translational and tilt stages. For this geometry a fibre with cylindrical symmetry radiates light into a short gap of air or coupling gel before the light encounters the integrated-optic waveguide and substrate. Various linear misalignment mechanisms between fibre and waveguide can exist and are discussed here.

8.4.1 Horizontal "Transverse" Misalignments

During the alignment steps the gap length between fibre and integrated optic waveguide is minimized to achieve maximum coupling and the mode pattern of the fibre is present at the entrance aperture of the integrated-optic waveguide. For this geometry the coupling theory results of Appendix C can be employed with region (II) removed, thus simplifying the coupling expression.

The integrated-optic waveguide modes form a discrete set and the overlap integral representing the power coupled to the mth mode can be obtained by setting $G_m G_m^*$ equal to 1 in (C.12), and is written as:

$$P_m = |\frac{\frac{\beta_m}{k_o}}{2\sqrt{\frac{\mu_o}{\epsilon_o}}} \int_{-\infty}^{\infty} \int_{-\infty}^{\infty} \psi_f(x,y)\psi_m^*(x,y)dxdy|^2 \tag{8.5}$$

where $\psi_f(x,y)$ and $\psi_m(x,y)$ represent the normalized electric field profiles for the fibre and the integrated optic waveguide respectively. If the fibre had the same mode profile as the integrated-optic waveguide, P_m would equal unity as using equation (8.1). The total power coupled is expressed as a sum over all the integrated-optic waveguide's modes:

$$P_{tot} = \sum_{m=0}^{N} P_m \tag{8.6}$$

Figure 8.4 shows a slice along the central axis of the electric field profile for the optical fibre, having Gaussian profile, and the four lowest order modes that can be propagated in an integrated-optic waveguide.

With these profiles, the expression in equation (8.5) can be evaluated numerically and the power coupled to each mode obtained.

When the fibre is in perfect alignment with the integrated-optic waveguide the maximum in the fibre's profile aligns with the maximum of the $m = 0$ mode profile and in this position the power coupled to this mode will be large. The power coupled to the $m = 1$ and $m = 3$ waveguide modes will be zero due to the
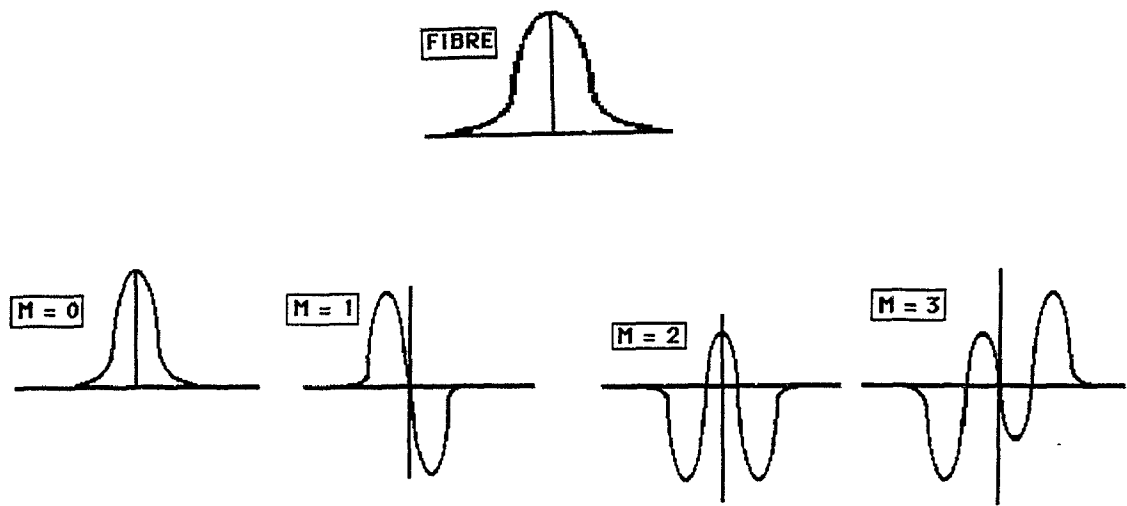
Figure 8.4: Transverse slice through the electric field profile for the optical fibre and 4 lowest order modes of the integrated-optic waveguide.

antisymmetric nature of the electric field profile about the central axis. The $m = 2$ mode will have contributions to the power coupling integral that cancel due to the presence of the side lobes which are opposite in sign to the central lobe. Thus when the fibre and integrated-optic waveguide are in perfect alignment only the lowest order mode will be highly excited. The other modes ($m = 1, 2$ and 3) can be excited by aligning the fibre's central maximum with either of the mode's larger side lobes. This has the effect of maximizing the overlap integral for that particular mode.

Experimentally, selective mode coupling is accomplished by moving the fibre transversely with respect to the integrated-optic waveguide, i.e., parallel to the crystal-air interface. Observation of the output end of the waveguide using the video monitoring system shows that the lowest order mode ($m = 0$) is excited for perfect alignment. As the fibre is translated further the output profile shifts continuously from $m = 0$ to $m = 1, 2$ and 3. Figure 8.5 shows the observed guided mode profiles as the fibre is translated across an integrated-optic waveguide formed by in-diffusing an 8 μm wide strip of titanium in a $LiNbO_3$ substrate. The offset

required to excite a particular mode is given in table 8.1 and it is interesting to note that a shift of 7 μm is required to excite the m = 3 mode. This reflects the fact that lateral diffusion of the titanium strip takes place thus broadening the waveguide width.

Table 8.1

Mode Order	Offset (μm $\pm.3$ μm)
0	0
1	2
2	4
3	7

In perfect alignment the optical power not converted into guided mode(s) of the integrated-optic waveguide due to modal mismatch must show up in the form of substrate and/or air modes if no other loss mechanisms are present. The power coupled to these modes is discussed in Appendix C and is accounted for by the G_s and G_a coupling coefficients which are similar in form to the G_m coefficient. For the above interconnection, substrate modes have been observed experimentally using the video system, manifesting themselves in the form of semicircular rings centered on the integrated optic waveguide and extending downward from the crystal air surface as shown in figure 8.6. In the ray picture the substrate light can be thought of as originating from a numerical aperture and/or waveguide core size mismatch between the waveguides. The light radiating outside the acceptance cone, and in the substrate of the integrated-optic waveguide, forms the substrate light.

The origin of the rings observed in the substrate has been confirmed experimentally by refitting the video camera with a long focal length lens and focusing through the crystal onto the fibre end which was aligned with one of the integrated-optic waveguides. The observed profile is shown in figure 8.7.

The central lobe is clipped due to local saturation in the video camera tube.

m = 0
OFFSET = 0 μm

m = 1
OFFSET = 2 μm

m = 2
OFFSET = 4 μm

m = 3
OFFSET = 7 μm
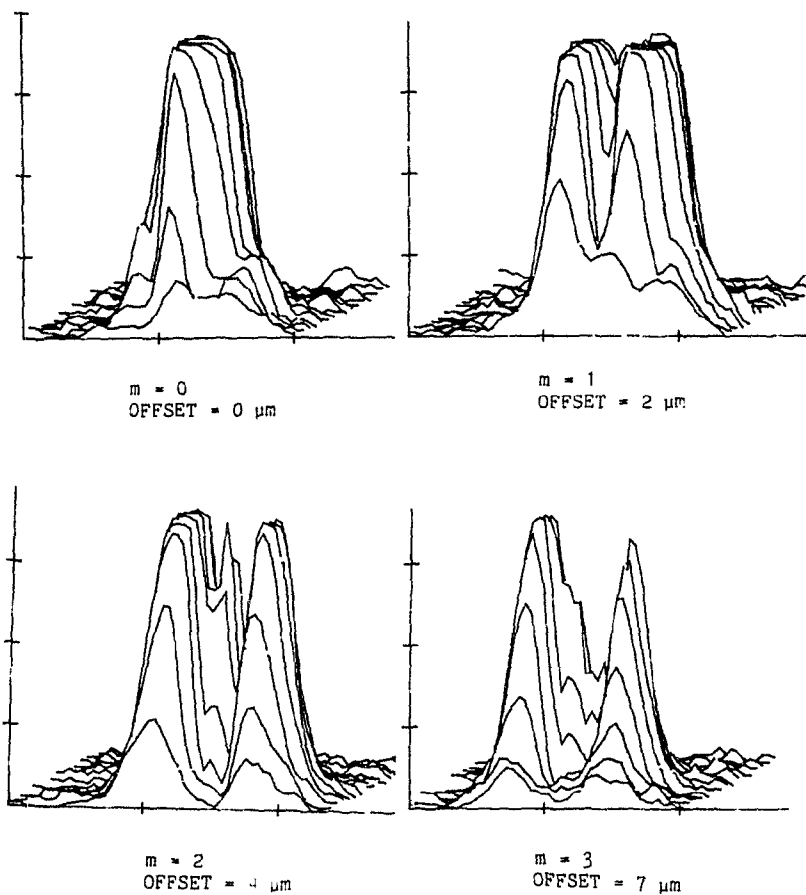
Figure 8.5: Mode profiles coupled by translating the fibre laterally.

CRYSTAL EDGE

GUIDED LIGHT

SUBSTRATE RINGS
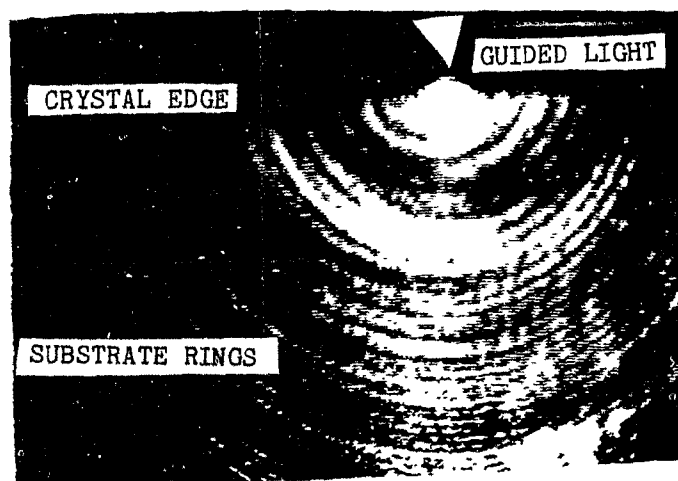
Figure 8.6: End view of the integrated optic waveguide.
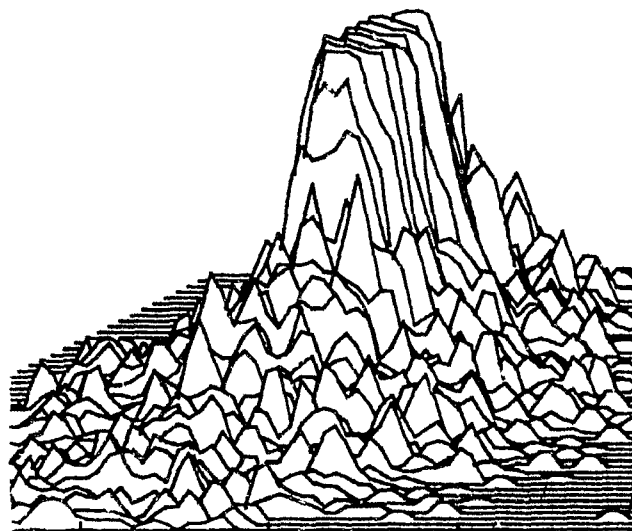
Figure 8.7: Radiation profile from the end of the fibre.

The camera and lens are then pulled back from the crystal while the light originating from the fibre end is observed. Two representative profiles of the observed light are shown in figure 8.8, taken 150 μm out of focus (A) and 200 μm out of focus (B). From these profiles individual rings can be observed and in (B) the rings are better defined and show further spreading into the substrate. When the camera and lens are pulled back further and focused onto the output edge of the integrated-optic waveguide, the ring pattern shows considerable spreading into the substrate and the guided light of the waveguide is observed in focus, as shown in figure 8.6, with the rings present.

8.4.2 Vertical "Depth" Misalignment

For a fibre and integrated-optic waveguide interconnection, the power coupled as the fibre is translated from above the crystal-air interface to below the crystal air interface, passing through perfect alignment, has been measured. To perform the measurement the fibre coupling setup is modified slightly from that discussed in chapter 5. At the laser to fibre coupling apparatus (figure 5.5) a beam splitter is inserted between the variable density filter and the rotatable polarizer. The reflected beam is measured using a Photodyne multimeter (22XLA) and serves
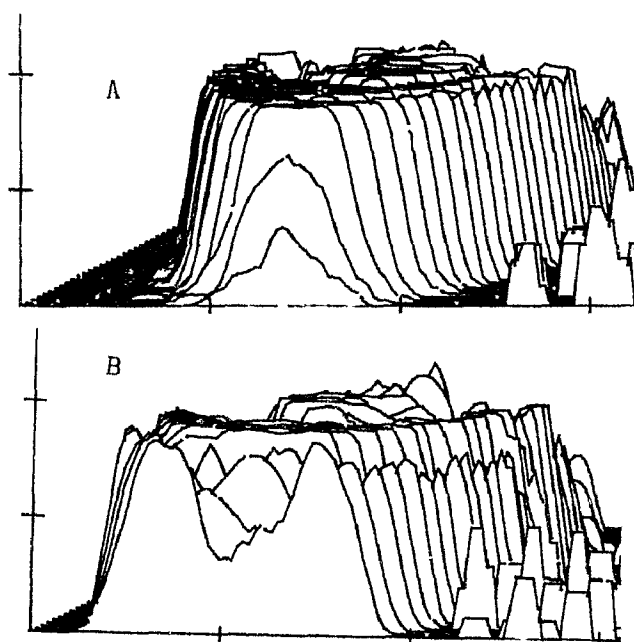
Figure 8.8: Ring profiles observed for: A - 150 μm out of focus and B - 200 μm out of focus.
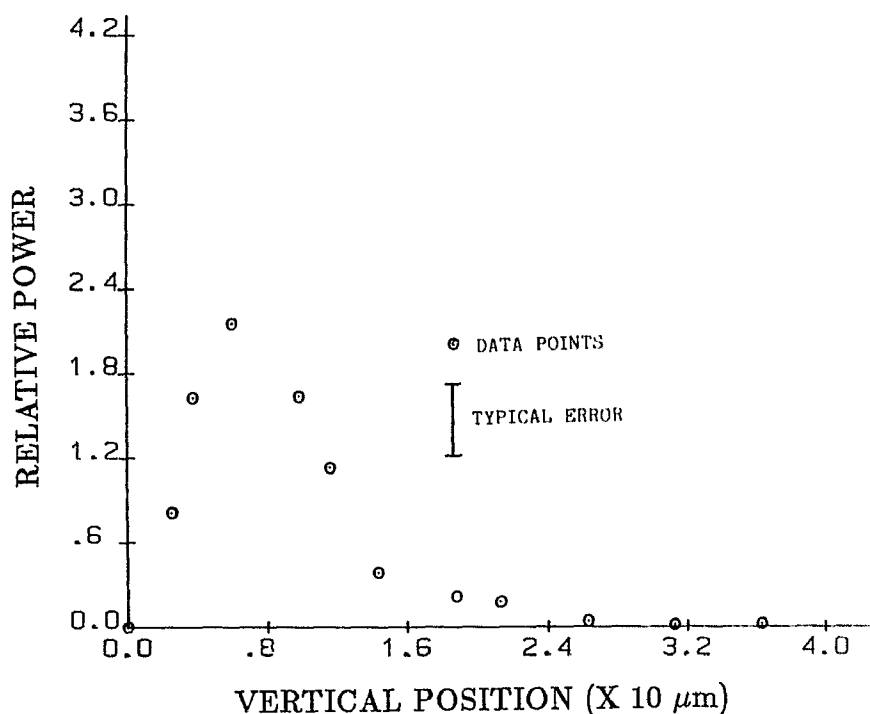
Figure 8.9: Power coupled to waveguide as a function of the fibre's vertical position.

as the reference level for the power coupled to the polarization preserving fibre. Figure 8.9 shows the power coupled to the waveguide versus fibre position.

Best coupling occurs when the fibre's power scatters strongly off the edge of the crystal at the entrance aperture of the waveguide as shown in figure 5.9. It is observed from the sharpness of the power coupled peak, that offsets in the order of microns can severely affect the power coupling efficiency.

It is observed experimentally that, by translating the fibre in this direction only, one depth mode order is excitable for the waveguides studied. Expression (8.5) can be used to evaluate the power coupled to the waveguide for the translation of the fibre performed here. In this case, the integrated-optic waveguide, only a single lobe in the profile and only one power coupling integral need be calculated.
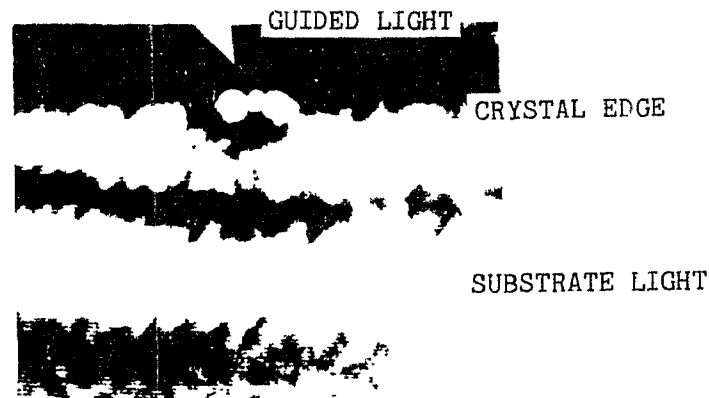
Figure 8.10: Substrate coupling to second order guided mode.

It is interesting to note from the figure that power is coupled to the waveguide when the fibre is located below the top surface of the crystal and that very little power is coupled when the fibre is positioned above the top surface of the crystal. With the fibre in the upper position the radiated power is reflected off the crystal's top surface since the angle of incidence is large with respect to the surface normal. On the other hand, when the fibre is positioned below the top surface of the crystal, light enters into the substrate at normal incidence to the crystal's endface. The waveguide having only a slightly larger index than the bulk material results in strong coupling between light propagated in the substrate and allowed waveguide modes. Thus light is transferred into the guided modes. Figure 8.10 shows the output of the crystal and waveguide when the fibre radiates its power into the substrate. The second order mode, characterized by three bright spots, is shown excited in this observation and clearly displays the existence of the T_s coupling coefficient of equation 8.2. The high intensity horizontal bands in the photograph are interference phenomena occurring when light arrives directly from the fibre and when it is reflected from the crystal-air interface.

8.4.3 Longitudinal "gap" Coupling

The effects on the coupled power due to the waveguide separation has been investig d using the fibre coupling and video system and the power monitoring modification discussed above. In steps of 50 microns the fibre is pulled back from an integrated-optic waveguide and the coupled power measured. Figure 8.11 shows the curve of power coupled versus end separation for integrated-optic waveguides formed from 4 and 6 μm in-diffused titanium strips.

The $\log_e$(power coupled) versus end separation is plotted in figure 8.12 for these waveguides. The linear nature of the curves strongly suggests that the power coupled follows an expression of the form:

$$P = P_o e^{-\alpha z} \tag{8.7}$$

where P_o is the initial power coupled when no gap is present, α is an attenuation coefficient related to the slope of the curve and z is the waveguide separation. From the slope of the curves of figure 8.12 the attenuation coefficient at He-Ne wavelength $\lambda = 0.6328$ μm for the 4 μm channel is:

$$\alpha_4 = 5.9E - 03\mu m^{-1} \tag{8.8}$$

and for the 6 μm waveguide:

$$\alpha_6 = 5.3E - 03\mu m^{-1} \tag{8.9}$$

By calculating maximum and minimum slopes through the data an error of $\pm$ 0.3 E-03 μm^{-1} can be expected in the readings.

In the previous chapters on cladding overlays and angle propagations (chapters 6 and 7) the attenuation coefficient (α) has been related to the imaginary component of the mode propagation constant, $\beta = \beta_r - i\alpha/2$. This relationship
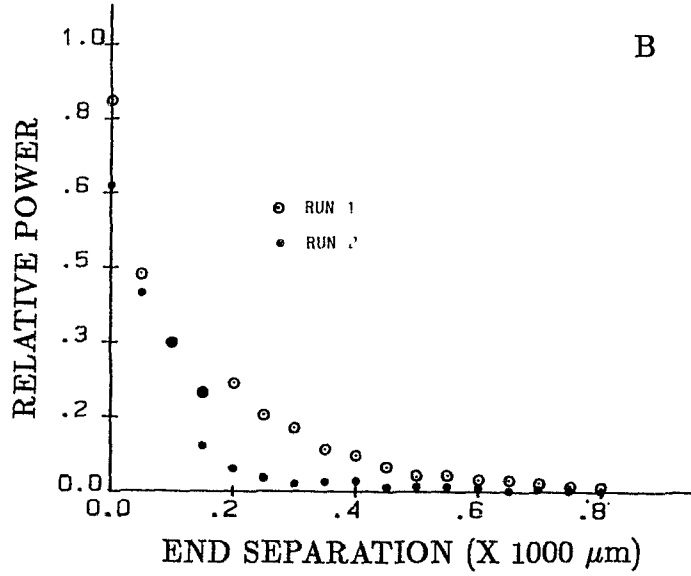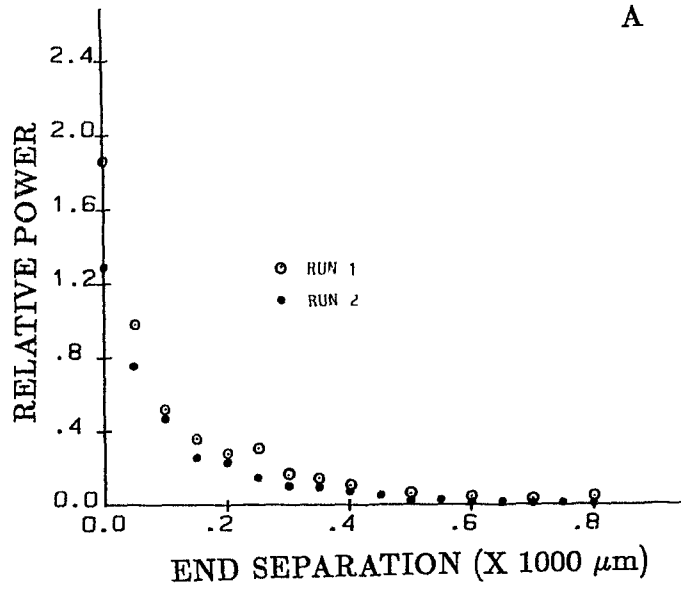
Figure 8.11: Relative power versus end separation for the 4 and 6 μm channel waveguides.
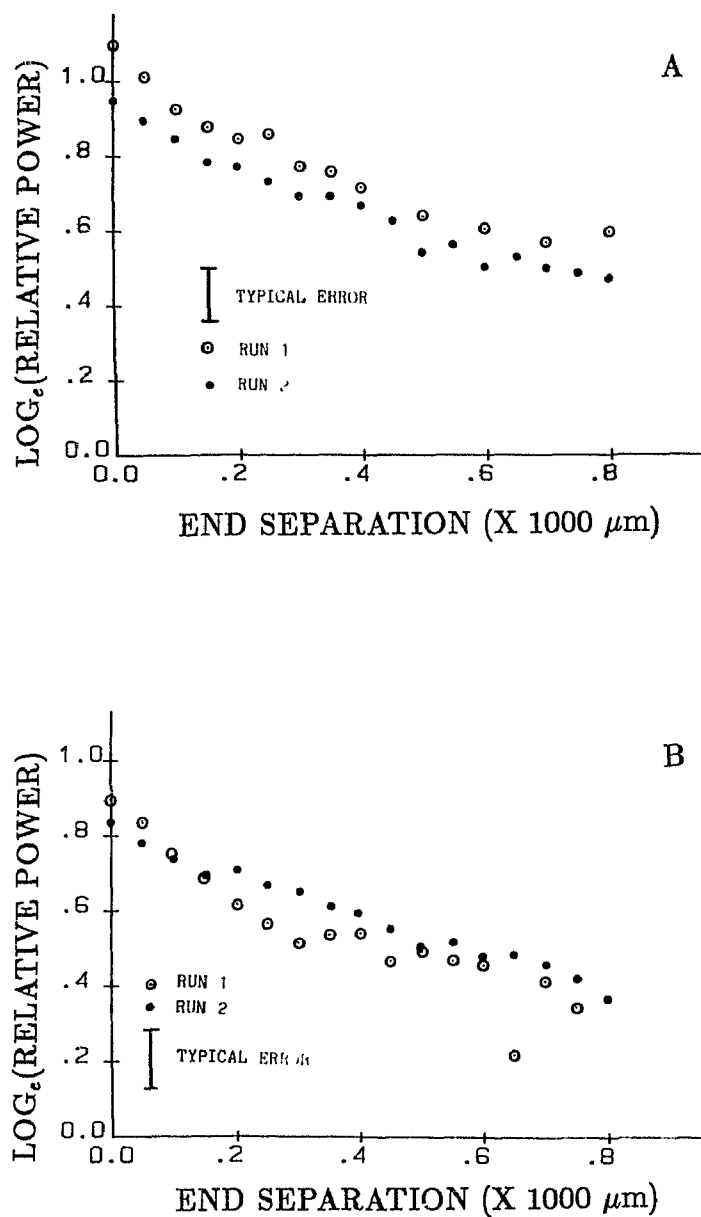
Figure 8.12: Log_e(power coupled) versus end separation for the 4 and 6 μm channels.

is also applicable here and the imaginary component to the propagation constant originates from the presence of the fibre integrated-optic waveguide separation.

The simplified coupling model has been evaluated for optical components as a function of gap length. The numerical aperture of the fibre of 0.17, taken from the data sheets, is used to calculate the exponent, R, from equations (8.3) and (8.4). By calculating the power coupled to the waveguide as a function of gap length the curve of $\log_e$(power coupled) versus gap length for the 4 and 6 μm channels was generated. From the slope of these curves, modeled to equation (8.7), the following attenuation coefficients are obtained:

$$\alpha_4 = 6.6E - 03\mu m^{-1} \qquad and \qquad \alpha_6 = 5.9E - 03\mu m^{-1} \qquad (8.10)$$

and are only slightly larger than the experimentally obtained values.

An analysis of single mode splice losses as a function of end separation[81,82] provides an expression which can be written in the form of an exponential decay when gap lengths are of the order studied here. The purpose of using our simple model rests in the fact that LiNbO$_3$ waveguides with a gap present can be easily treated, while their analysis is no longer applicable due to the asymmetry added by the crystal-air interface.

In this section we have seen the dependence on misalignments of the optical power coupling from fibre to integrated-optic waveguides. As shown, misalignments can highly influence coupling efficiency. For the integrated-optic LiNbO$_3$ waveguides to be presented, vertical alignment of the waveguides is dictated by the quality of the optical grade surface of the crystal. The waveguides being formed directly below this surface result in perfect vertical alignment ($\lambda/10$). Transverse alignments are governed by the linearity of the laser writing system used to make the mask patterns and are aligned transversely to an accuracy of .1 μm. Control over the above mentioned misalignments enables the effects of gaps in LiNbO$_3$ waveguides to be studied exclusively.
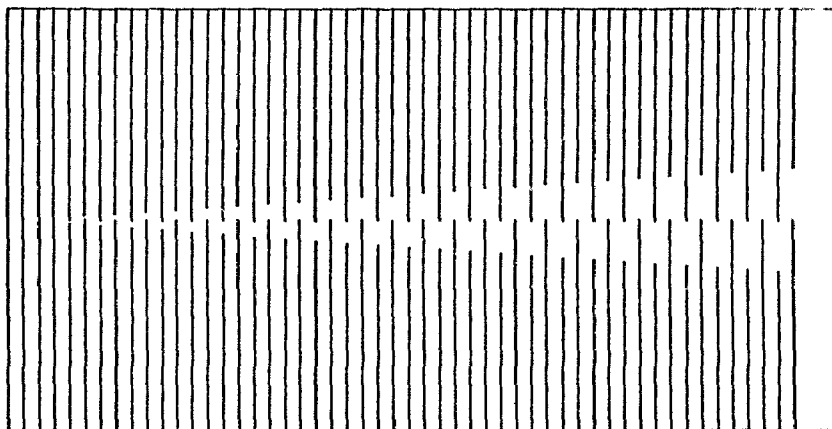
Figure 8.13: Waveguide pattern for generating gaps in waveguides.

8.5 Gaps in LiNbO₃ Integrated-Optic Waveguide

The mask line pattern used to create gaps in integrated-optic waveguides is shown in figure 8.13 and has been produced using the laser writing system[38]. Each line is separated from its neighbour by 200 μm.

The breaks range from 0 μm on the left and increase in 15 μm steps to a maximum of 750 μm on the right. This pattern is photolithographically transferred to X-cut crystals with titanium strips extending parallel to the Y axis. Subsequent in-diffusion of the metal and polishing of the crystal edges completes the waveguide preparation. The crystals can then be mounted onto the fibre coupling setup, delivering 0.6328 μm light. With the above power monitoring modification in place the output power of the waveguides is measured.

$\sqsupset$ waveguides formed from these crystals enable end gap separation effects to be studied for LiNbO₃ waveguides. The sets of log$_e$(power coupled) versus gap length for 4 and 6 μm waveguides are shown in figure 8.14 and the linear nature of the curves suggests the fitting of the data to equation 8.7. From the slope of each curve can be obtained the attenuation coefficient (α) and this is calculated as:

$$\alpha_6 = 1.09E - 2\mu m^{-1} \qquad and \qquad \alpha_4 = 1.3E - 2\mu m^{-1} \qquad (8.11)$$

Due to unavoidable power coupling variations from waveguide to waveguide, as discussed in appendix B, a large experimental error is present in the readings. By calculating maximum and minimum slopes an error of 0.6 E-3 μm^{-1} can be expected in the attenuation coefficients.

Using the coupling model with the effects of the interface included, the attenuation coefficients for the 4 and 6 μm channels as a function of gap length are calculated. The numerical aperture of 0.085 for the integrated-optic waveguides is obtained from an estimate of the propagation constant, β, and the ray picture of figure 3.2, to define the angle θ_m in equations (8.3) and (8.4).

The attenuation coefficients for the waveguides using the coupling model are:

$$\alpha_6 = 1.14E - 2\mu m^{-1} \qquad and \qquad \alpha_4 = 1.39E - 2\mu m^{-1} \qquad (8.12)$$

Relating the attenuation coefficient to the waveguide theory enables identification of an imaginary contribution to the guided modes propagation constant which leads to a power loss factor that depends on the interaction length, i.e., the gap length. This provides a simple method of treating the influence of gaps in waveguides in a theoretical analysis.

8.6 Gap Based Devices

Several integrated-optic devices based on the design of appendix D have been built on the 4 μm single TE mode waveguide with electrodes extending the length of the gap and 20 μm spacing. The TE mode is chosen since it has the electric field polarized along the extraordinary index axis for this waveguide geometry. The observations made on the devices required measurement of output power in the guided mode profile as the applied voltage to the electrodes varies from 200 volts to -200 volts. This results in electric fields from +10 to -10 V/μm directed between the electrodes. Figure 8.15 shows the output power changes for the applied positive and negative voltage maximums.
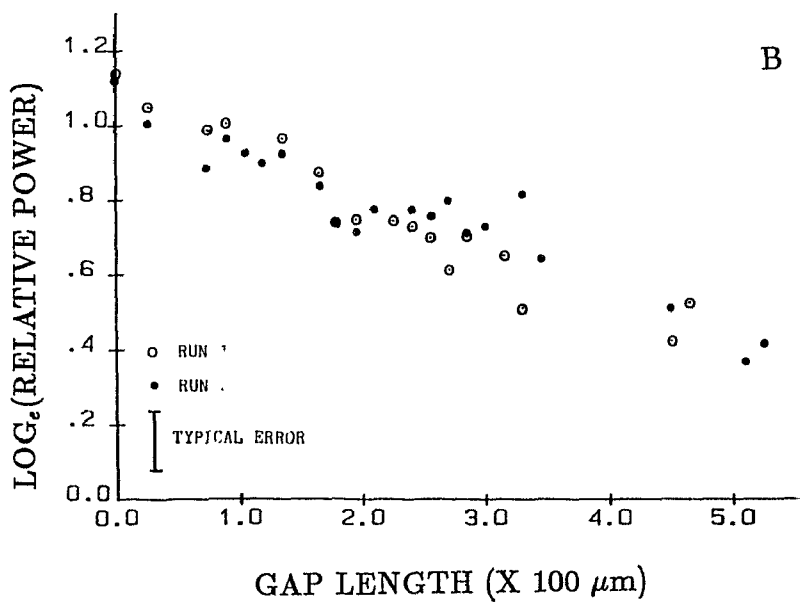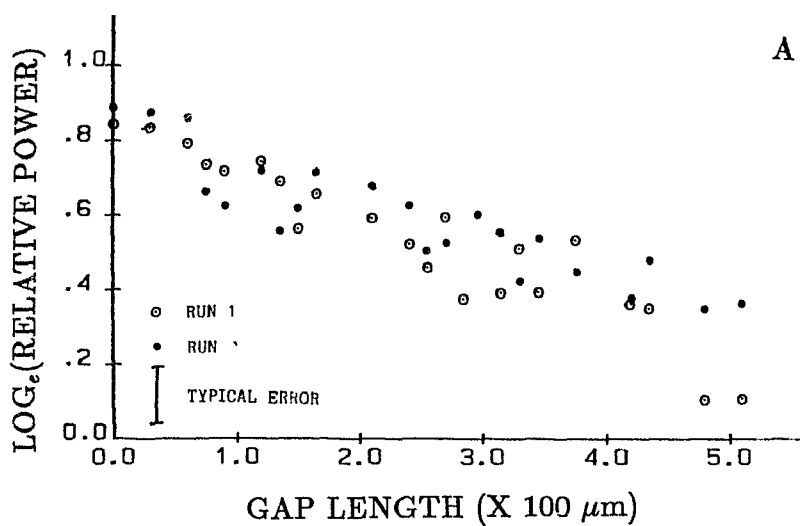
Figure 8.14: Log(power) versus gap length for LiNbO$_3$ waveguides formed from 4 μm (A) and 6 μm (B) titanium strips.
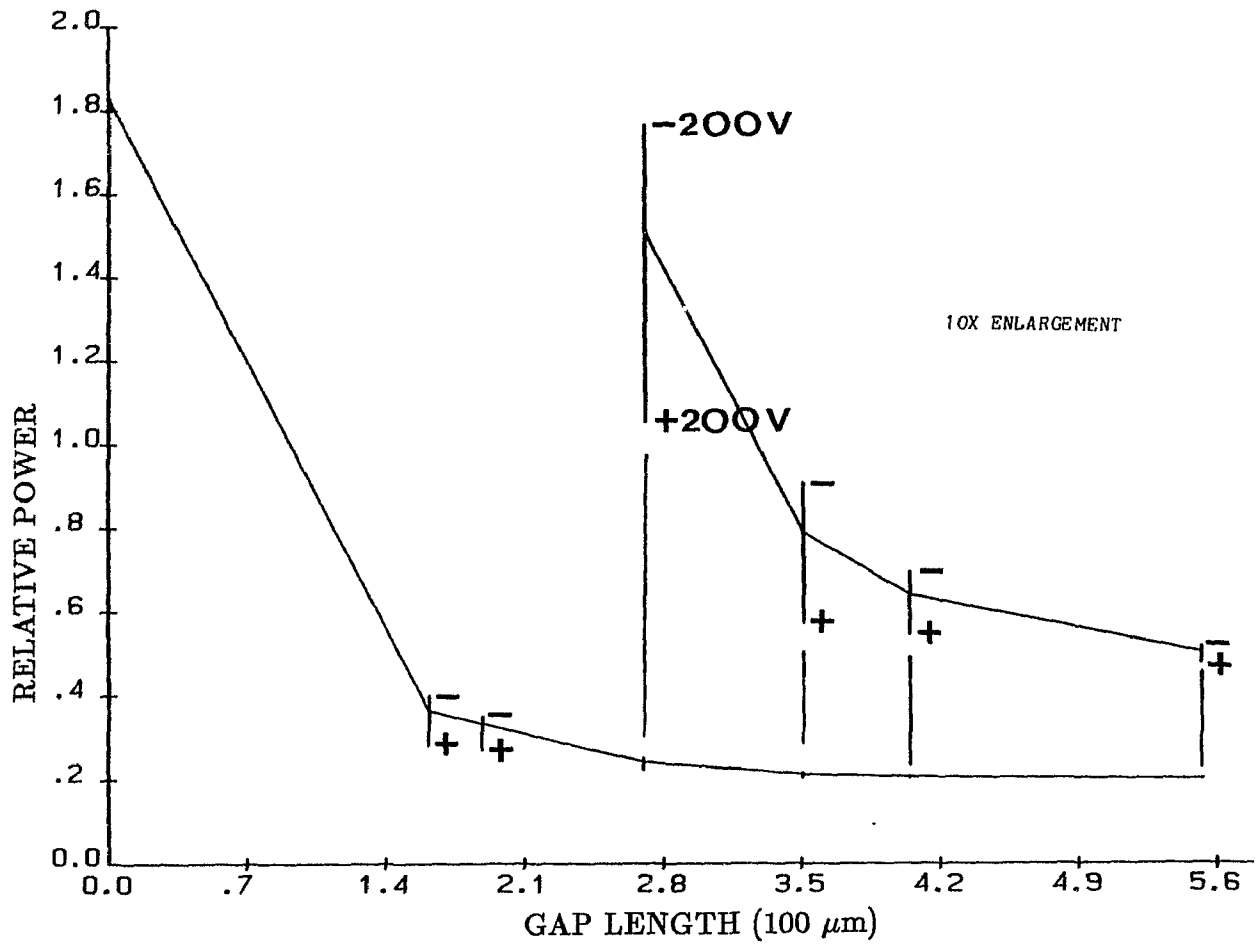
Figure 8.15: Modulator output power changes as a function of applied voltage. Inset shows 10X enlargement of long gap modulators.
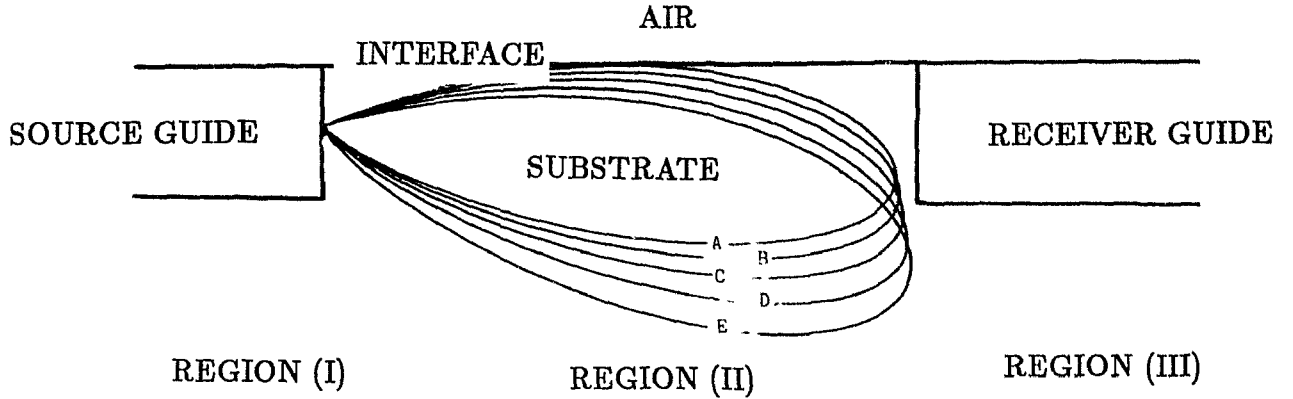
Figure 8.16: Effect of applied electric field on radiation pattern in gap region,
A - Power factor (R) = 1419, E = -10 V/μm, B - Power factor (R) = 1296,
E = -5 V/μm, C - Power factor (R) = 937, E = 0 V/μm, D - Power factor
(R) = 811, E = 5 V/μm, E - Power factor (R) = 384, E = 10 V/μm.

The observed increase in power is caused by an electric field directed opposite
to the Z optical axis while the observed decrease in power is caused by the electric
field directed along the optical axis. From the recorded power levels when the
applied fields are -10 , -5, 0, +5 and +10 V/μm, an exponential curve has been fitted
to the recorded power level points and the new attenuation coefficients obtained for
these applied electric fields are:

$$\alpha_{-10} = 1.23E - 2\mu m^{-1} \qquad \alpha_{-5} = 1.25E - 2\mu m^{-1} \qquad (8.13)$$

and

$$\alpha_{+5} = 1.40E - 2\mu m^{-1} \qquad \alpha_{+10} = 1.63E - 2\mu m^{-1} \qquad (8.14)$$

Using the simplified coupling model the attenuation coefficient can be related
to the $\cos^R(\theta)$ function used to model the profile of the source's radiation pattern.
Figure 8.16 shows that the radiation pattern is pushed away from the interface gap
region for positively directed electric fields and pulled up towards the interface for
negatively directed electric fields.

In discussing the device design in Appendix D, it is shown that when the electro-optic effect increases the index of refraction in the gap region, a new set of radiation modes can be created and the spectrum of substrate and air modes can therefore have a larger amplitude in this increased index region. The net effect of the new modes and increased amplitude of the substrate-air modes, is to concentrate power into the region between the endfaces of the coupled waveguides. This effect is observed by pulling the radiation pattern towards the interface and concentrating the power between the waveguides.

When the electric field direction is reversed, the decreased index of refraction in the gap region has the effect of reducing the amplitude of the air modes in that location. The amplitudes for the substrate modes are also decreased in that region but modes with β/k_o, with no field applied, between n_2 and $n_2 + \Delta n_2$ will now have an exponential decay amplitude in the gap region. The net effect is to increase the power spread into the substrate region. Using the simplified model, this effect is represented by pushing the maximum of the output power profile away from the interface and down into the substrate.

8.7 Summary

In this chapter the effects of waveguide interconnections have been studied for the fibre to integrated-optic waveguide combination and gaps in waveguides formed in LiNbO$_3$ substrates.

For the fibre to integrated-optic interconnection three misalignment mechanisms have been examined and the experimental observations discussed using radiation mode expressions and the simplified coupling model. The effect of the waveguide interspacing has been found to follow an exponential decay curve thus allowing the evaluation of a power attenuation coefficient. The coefficient can be related to an imaginary propagation constant which results from the presence of the gap. The attenuation coefficients observed are two orders of magnitude larger

than those of LiNbO$_3$ waveguides and seven orders of magnitude larger than those in optical fibres. They are however two orders of magnitude smaller than those in MQW waveguides.

For LiNbO$_3$ waveguides with gaps the exponential decay curve fits the data well. For these waveguides the attenuation coefficient is found to be approximately twice that of the above fibre-waveguide pair. The increase in attenuation coefficient is accounted for by the influence of the crystal-air interface which pushes the central maximum of the radiation pattern away from the interface and into the substrate.

The device design of appendix D is shown to alter the power coupling and is expressed through a change in the attenuation coefficient. Using the simplified coupling model, the change in power is discussed in terms of the power spread in the immediate vicinity of the gap region. Negatively directed electric fields have the effect of concentrating the power in the immediate vicinity of the gap region while positively directed electric fields increase the spread of power into the substrate. These arguments are consistent with results developed from the radiation mode coupling treatment.

CHAPTER 9 NONLINEAR DIRECTIONAL COUPLER

9.1 Introduction

Controlling the properties of light has been the major achievement of integrated optics. Devices have been designed to operate as, for example, modulators, attenuators and switches. For optical information processing high speed devices in the GHz range are desirable. If conventional electrically controlled integrated optic devices were used, they would have to be operated at the upper limits of their speed and future enhancement of systems using these devices would be difficult. At high speeds the electrical controlling signal and the optical pulse must be perfectly synchronized to ensure proper operation. A better design would be to encode the switching information with the incoming pulse. For electrically controlled devices this means the signal must first be decoded and the light pulse then processed. Clearly the presence of the electrical interface adds another complication to be dealt with and it is desirable to replace it with a better method for controlling the light pulse. Being able to process the light directly within the device is an attractive alternative. This requires a medium that can act not only on the incident light but can react differently depending on the encoding technique. To keep switching time to a minimum the recovery period for this process would have to be very short. Such materials do exist and are actively studied in nonlinear-optics where the intensity of the input beam can alter the properties of the waveguide material. Several liquid crystal[83] and organic compounds[84] exhibit nonlinear behavior; however we shall focus our attention on the optical properties of the relatively new, artificial media called Multiple-Quantum-Wells (MQWs) manufactured by molecular beam

epitaxy (MBE).

The possibility of all-optical signal processing using a MQW is addressed by focusing attention on a nonlinear directional coupler[85]. In the analysis presented here, nonlinear field distributions are applied in calculating the coupling coefficients as opposed to the previous work[85] that dealt only with the linear field approximation. Another feature of our analysis shows that the waveguides consist of linear low loss AlGaAs slabs, enabling lower absorption losses to be achieved and making device realization possible. As will be shown in this work, the losses of the structure must be taken into account and as a result completely different features between the lossless and lossy cases are observed for the same design geometry. It will be shown that the device can perform switching operations based solely on the input light intensity. Furthermore, parameter values taken from experiments published in the literature are used in the calculations to show that the device can be manufactured with materials and techniques currently available.

Before discussing in detail the nonlinear directional coupler, the linear directional coupler is described. It is simpler to analyze in theory and the concepts are applicable when the nonlinear coupler is operated at low power.

9.2 Linear Directional Coupler

The directional coupler shown in figure 9.1 can consist, for example, of two channel waveguides which are coupled over a length, L, and exchange power by evanescent means. For complete exchange of power to take place between the waveguides, guided light must propagate with the same propagation constant, β, in each channel. The rate of coupled power is determined by the overlap of the the modal fields in the separate waveguides and depends on the guide separation, the interaction length and lateral mode penetration into the substrate[86].

For the coupled waveguides, the mode's normalized electric field amplitude
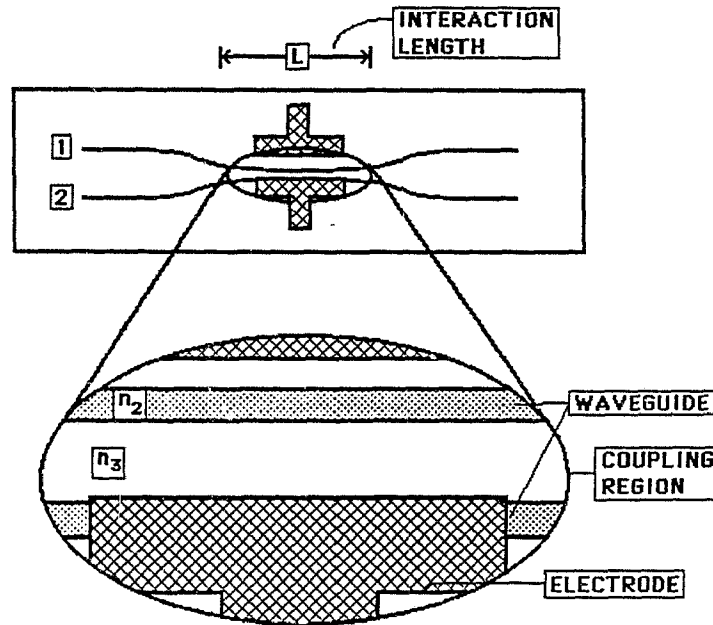
Figure 9.1: Linear evanescent directional coupler with asymetric controll electrode geometry.

(a$_1$ or a$_2$) obeys the following equation:[86]

$$\frac{da_j(z)}{dz} = -iQa_i(z) - \frac{\alpha_d}{2}a_j(z) \qquad i,j = 1,2 \quad and \quad i \neq j \qquad (9.1)$$

where α_d is the single waveguide attenuation coefficient of the optical power and Q is the coupling coefficient which is determined from waveguide parameters of the form:[87]

$$Q = \frac{\omega(n_2^2 - n_3^2)}{4\pi P_o} \int_{-\infty}^{+\infty} E_1 E_2 \, dx dy \qquad (9.2)$$

where n$_2$ is the waveguide index, n$_3$ is the substrate index and P$_o$ is the normalized power. In equation (9.2), E$_1$ is the modal field profile an $\cdot$ is obtained by solving the two-dimensional wave equation for waveguide 1 only, with waveguide 2 completely removed.

When all the power is launched in waveguide 1, the initial conditions are:

$$a_1(0) = 1 \qquad and \qquad a_2(0) = 0 \qquad (9.3)$$

and the solutions for the field's amplitudes are:

$$a_1(z) = cos(Qz)e^{\frac{-\alpha_d z}{2}} \qquad (9.4)$$

and

$$a_2(z) = -isin(Qz)e^{\frac{-\alpha_d z}{2}} \qquad (9.5)$$

These expressions demonstrate that energy couples sinusoidally from one guide to the other and back again (figure 9.2, solid trace). The power at any position along the waveguide depends on initial conditions, the coupling coefficient and the exponential decay factor. The linear nature of the guiding and interaction mediums results in the power division, between the waveguides at the end of interaction length L, being independent of the input launch conditions. The output power can, however, be changed by making use of the electro-optic properties of the substrate and the asymetrical electrode layout above the waveguides to alter the coupling coefficient. In figure 9.2 the dashed trace shows a situation where the electric field generated by a voltage across the electrodes has modified the coupling coefficient so that at the exit end of the structure all power is now in the other waveguide. Many of these devices have been reported[88-93] and a commercial device is now available from Crystal Technology, Inc.

9.3 Nonlinear Directional Coupler

The MQW structures are formed from many alternating layers of pure semi-conductor and doped semiconductor[94-97] material put down in one atomic mono-layer. Thichness of the individual layers varies for different applications and is
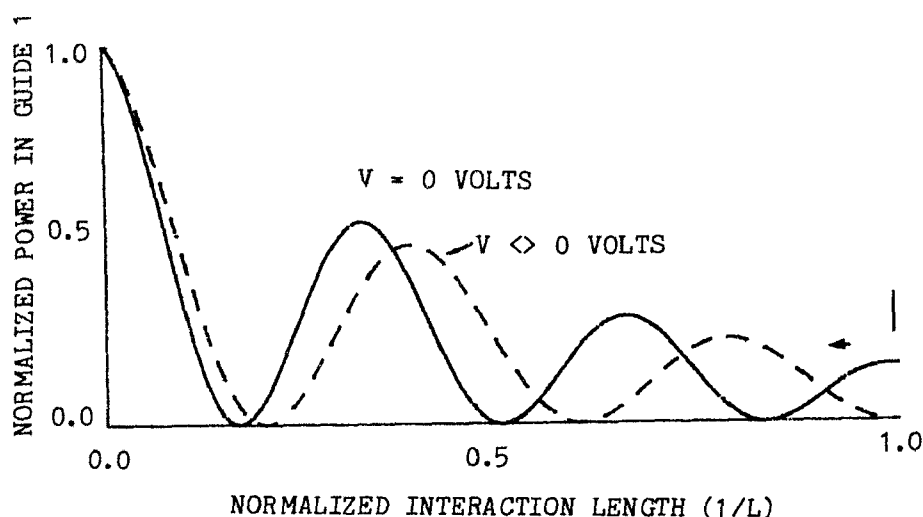
Figure 9.2: Power in guides for linear directional coupler, solid trace - normal power amplitude curves, dashed trace - electro-optically increased transfer length.

typically in the 50 to 150 Angstroms range. The nonlinear optical properties of the MQW's are characterized by an optical intensity dependent contribution to the bulk index of refraction of the semiconductor material ($n = n_3 + \eta I$) and are determined by excitons which are created by the absorption of incident photons. Excitons are electron-hole pairs forming a bound state analogous to the hydrogen atom. Because of the bandgap difference between the two components of the MQW structure, the excitons are confined in the wells of the conduction band. This confinement reduces the distance between the particles and increases the binding energy making excitonic effects observable at room temperature. Typical lifetimes of the photoionized exciton states are in the nanosecond to picosecond range[96]. These features of the MQW appear promising for the realization of high speed self-controlling devices and are actively being studied in research institutions world wide. Here we focus our attention on the nonlinear directional coupler. It should be noted that the refractive index changes in MQW's depend, in principle, upon the number of carriers generated in the semiconductor material. However, in our particular case, a direct relationship between the change and the intensity of light may be used because
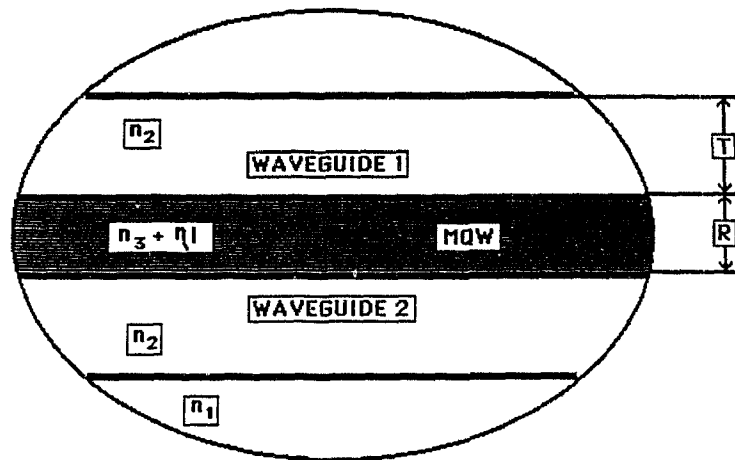
Figure 9.3: Nonlinear directional coupler.

operation is assumed to be at or very close to the exciton resonance. Saturation intensities were taken as approximately 2.5 E06 W/m^2.

The major difference between the nonlinear coupler and the linear coupler discussed above, is that at least one of the media of the coupler is nonlinear. Here electrodes are not required to modify the fields because light itself modifies the coupling coefficient. Figure 9.3 shows an enlargement of the interaction region of such a device originally proposed by Stegeman et. al.[98], and designed by us[100], where planar instead of channel waveguides have been used. Due to the presence of the MQW the evanescent wave coupling theory has to be reworked.

9.3.1 Lossless Analysis

A particularly useful analysis for numerical calculations by Jensen[85] includes the nonlinearity in the evanescent coupling theory and develops a differential equation for the normalized amplitudes (a$_i$ dimensionless) of the electric field for the

two single mode waveguides. The new coupling equations are written as:

$$-i\frac{\partial a_1}{\partial z} = Q_1 a_1 + Q_2 a_2 + (Q_3|a_1|^2 + 2Q_4|a_2|^2)a_1 \qquad (9.6)$$

and

$$-i\frac{\partial a_2}{\partial z} = Q_1 a_2 + Q_2 a_1 + (Q_3|a_2|^2 + 2Q_4|a_1|^2)a_2 \qquad (9.7)$$

The coupling coefficients, Q's, are expressed as:

$$Q_1 = \frac{\omega n_a^2 \epsilon_o}{4P_o} \int_{-\infty}^{\infty} |E_1|^2 dx \qquad (9.8)$$

$$Q_2 = \frac{\omega(n_t^2 - n_a^2)\epsilon_o}{4P_o} \int_{-\infty}^{\infty} E_1 E_2^* dx \qquad (9.9)$$

$$Q_3 = \frac{\omega n_3^2 \eta \epsilon_o}{Z_o 4P_o} \int_{-\infty}^{\infty} |E_1|^4 dx \qquad (9.10)$$

$$Q_4 = \frac{\omega n_3^2 \eta \epsilon_o}{Z_o 4P_o} \int_{-\infty}^{\infty} |E_1|^2|E_2|^2 dx \qquad (9.11)$$

In this treatement P_o is the normalized input power per unit width across the waveguide slab, n_t is the index of refraction profile of the complete waveguide structure, while n_a is the index profile of one waveguide structure with the MQW layer extending to infinity, n_3 is the power independent index of refraction of the nonlinear medium and Z_o is the free space impedance. In these expression, E_1 and E_2 are the electric field profiles of modes in guides 1 and 2 respectively.

The identity of each coupling term can be linked to a particular mode interaction. The term involving Q_1 results from the dielectric perturbation to one waveguide due to the presence of the other waveguide, and represents only a small correction to the propagation constant, β. The term involving Q_2 arises from the mode in the adjacent guide and leads to linear coupling between the waveguides. From the similarity of expressions (9.6) and (9.7) with (9.1), Q_2 is identified with Q of the linear directional coupler. The term Q_3 is the strongest nonlinear term and arises from the nonlinear interaction of the mode, itself due to the presence of the

MQW. The second order nonlinear term, Q_4, arises from the nonlinear interaction of one mode with the mode of the adjacent waveguide and is small compared to Q_3.

The evaluation of the coupling coefficients, equation (9.8 - 9.11), requires that electric field expressions and total input power be known in the structure. The general wave equation when the nonlinear index of refraction is included has the form:

$$\nabla^2 E + k_o^2 n_3^2 E = k_o^2 \alpha_2 |E|^2 E \tag{9.12}$$

and uses the following expression for the dielectric constant:[99]

$$\epsilon = n^2 = (n_3 + \eta I)^2 = n_3^2 + \alpha_2 |E|^2 \tag{9.13}$$

The term with η^2 has been neglected against n_3^2 since $\eta I \ll n_3$, α_2 is related to the nonlinear component of the index of refraction through:

$$\alpha_2 = \frac{n_3^2 \eta}{Z_o} \tag{9.14}$$

$$I = \frac{n_3 |E|^2}{2 Z_o} \tag{9.15}$$

Seaton, et. al.[99], have solved the wave equation for a linear dielectric slab bounded by nonlinear self defocusing substrate cladding ($\eta < 0$) and linear superstrate cladding. As shown by Cada[100], using their equations does not present any problem in calculating the coefficients since, in the coupled mode analysis, E_1 and E_2 are the field expressions of the single waveguide with the other waveguide removed and the nonlinear cladding extended to infinity. The solutions to the wave equation in each layer are:[99]

$$E_{top\ cover} = c_2 e^{-s(x-R-T)} \tag{9.16}$$

$$E_{guide1} = c_1 (cos(k(R-x)) - \frac{q}{k} M_1 sin(k(R-x))) \tag{9.17}$$

$$E_{MQW} = \sqrt{\frac{1}{2\alpha_c}} \frac{q}{sinh(q(Z_1 + R - x))} \tag{9.18}$$

where C_i's are evaluated by matching the fields at the interfaces. In these expressions M_1, k, q, s, an d Z_1 are given by:

$$M_1 = coth(k_o q Z_1) \tag{9.19}$$

$$k = \sqrt{k_o^2 n_2^2 - \beta^2} \tag{9.20}$$

$$q = \sqrt{\beta^2 - k_o^2 n_1^2} \tag{9.21}$$

$$s = \sqrt{\beta^2 - k_o^2 n_3^2} \tag{9.22}$$

$$Z_1 = \frac{1}{k_o q} sinh^{-1}\left(\frac{q^2 \beta}{k_o n_3^2 |\eta| I_o}\right) \tag{9.23}$$

In equation (9.23), I_o is the light intensity present at the slab-MQW interface and it is this parameter which is varied in the calculation in order to generate curves for different input powers. The total power at input per unit width across the slab can be evaluated from:

$$P = \frac{\frac{\beta}{k_o}}{2\sqrt{\frac{\mu_o}{\epsilon_o}}} \int_{-\infty}^{+\infty} |E|^2 dx = P_s + P_f + P_{MQW} \tag{9.24}$$

where P_s, P_f and P_{MQW} are the powers contained in the superstrate, film and MQW-substrate respectively.

Equations (9.6) and (9.7) have been solved by Jensen[85] to obtain the expression for the power in the guides at any position, z, down the structure for any input power, $P_1(0)$. With the initial conditions of all power launched in guide 1, equation (9.3), the power remaining in guide 1 is given by:

$$P_1(z) = \frac{P_1(0)}{2}(1 + cn(2Q_2 z|m)) \tag{9.25}$$

where $cn(\psi|m)$ is the Jacobian elliptic function and $m = (P_1(0)/P_c)^2$, and P_c is the so called critical power where power launched at this level divides evenly between the waveguides and no further power exchange is observed.

The characteristics of a device depend highly on P_c and in Jensen's[85] analysis an approximate expression is:

$$P_c = P_o \left(\frac{4Q_2}{Q_3 - 2Q_4} \right) \tag{9.26}$$

which requires the evaluation of Q_2, Q_3 and Q_4.

An exact method of obtaining the critical power developed by Cada[101] was used in our analysis and does not require the evaluation of the coupling coefficients. It involves solving self-consistently two sets of equations where the critical electric field amplitude at the waveguide-MQW interface, E_c, and the critical input intensity, I_{oc}, are obtained from (9.27) and (9.28) respectively.

$$E_c^2 = \frac{1}{\alpha_2} \left((n_3^2 - n_2^2) + \sqrt{(n_2^2 - n_3^2)^2 + \left(\frac{\beta^2}{k_o^2} - n_3^2 \right)^2} \right) \tag{9.27}$$

$$I_{oc} = \frac{n_3 E_c^2}{2Z_o} \tag{9.28}$$

When the iteration produces no further change in the critical intensity, the input power $P_1(0)$ is calculated from (9.24). This particular value of $P_1(0)$ now corresponds to the critical power P_c. The approximate expression (9.26) and this technique provide values which are in good agreement.

9.3.2 Calculations

A computer program has been written to calculate the power remaining in guides 1 and 2 as a function of the interaction length and input power, $P_1(0)$. The structure design parameters are given below and are taken from published data:

- superstrate index, $n_1 = 3.210$,

- waveguide index, $n_2 = 3.513$,

- MQW power independent index, $n_3 = 3.502$,

- MQW power dependent index, $\eta = -2$ E-08 m^2/W,

- waveguide thickness, T = 1.8 μm,

- MQW layer thickness, R = 0.90 μm.

The steps for calculating the power remaining in the waveguides are as follows:

1. Choose an input irradiance, I_o, and calculate the propagation constant from the dispersion equation for slab waveguides with the nonlinear index included.

2. Calculate values for expressions (9.19) to (9.23), which will enable calculation of the electric field profile (9.16 to 9.18) at any position in the waveguide structure.

3. Obtain the input power from equation (9.24).

4. Obtain P_c by solving equations (9.27) and (9.28) and repeating steps 1 to 4 for I_{oc}.

5. From equation (9.25) evaluate the power remaining in the launch guide for various interaction lengths, z, down the structure. The power level of the second waveguide is obtained from $P_2(z) = P_1(0) - P_1(z)$.

Using this technique the curves of figure 9.4 have been generated.

From the graph, the exchange nature of the guided power depends on whether the input power is above, below or close to the critical power, P_c. For input powers below P_c, a position along the structure can be reached where all of the power from guide 1 has coupled to guide 2. The interaction length required for this power exchange to occur for the first time is called the **full power transfer length**. For these power levels the structure reacts similarly to a linear coupler with both waveguide modes having identical propagation constants, $\beta_1 = \beta_2$. At low powers, (0 to 0.18 mW/mm), in this particular case, the full power transfer length is relatively insensitive to small changes in power and the structure operates as a linear directional coupler. This is expected, since in the limit of low input power, the Jacobian elliptic function cn$(\psi|m)$ approaches the cosine function, and thus the well known
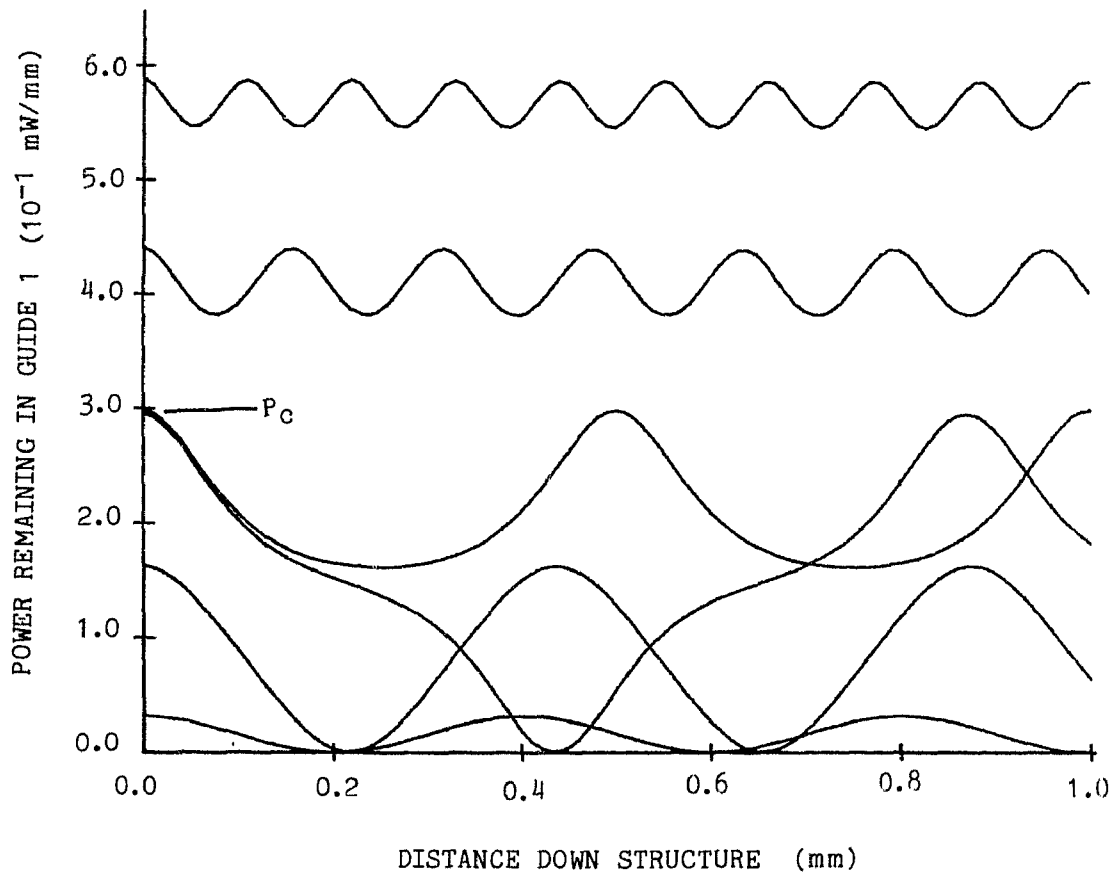
Figure 9.4: Power remaining in launch guide as a function of interaction length and input power.

solutions of the linear coupler are obtained.

For input powers in the vicinity of P_c, but with $P_{in} < P_c$, an increase in the full transfer length is observed. This is explained by observing the nature of the propagation constant, β, which is dependent on input power. Initially all of the power is propagated by the mode of guide 1 with propagation constant β_1 different from its low power value and that of waveguide 2. As power couples into guide 2, the mode of guide 2 increases in power while the mode of guide 1 decreases in power. This has the effect of reducing the difference that exists between β_1 and β_2. When the power of guide 2 equals the power remaining in guide 1, the propagation constants will be equal. This sets up the condition of full transfer of power between the two waveguides. The initial inequality of the propagation constants and the fact that power must exchange before $\beta_1 = \beta_2$ has the effect of increasing the full transfer length.

For input powers above P_c, full transfer of power from guide 1 to guide 2 no longer occurs. At these input power levels the 50:50 power division between the waveguides is never reached and the propagation constants are always phase detuned $(\beta_1 \neq \beta_2)$. In this case the **partial transfer length** is defined as the interaction length required for the power of the second waveguide to reach a maximum for the first time. For powers above P_c, the transfer length decreases with increasing power contrary to that observed for input powers below P_c. In this region the structure reacts as a phase detuned power dependent directional coupler. Phase detuning and the corresponding partial transfer of power have been observed experimentally in linear directional couplers[102,103].

At $P_1(0)$ equal to P_c the power divides evenly between the two waveguides with no further transfer of power observed. This situation corresponds to the case where full transfer length reaches infinity. The equality of the powers in the two waveguides can be regarded as setting up a single stable symmetric mode of the two waveguide structure with a single propagation constant $\beta = \beta_1 = \beta_2$.
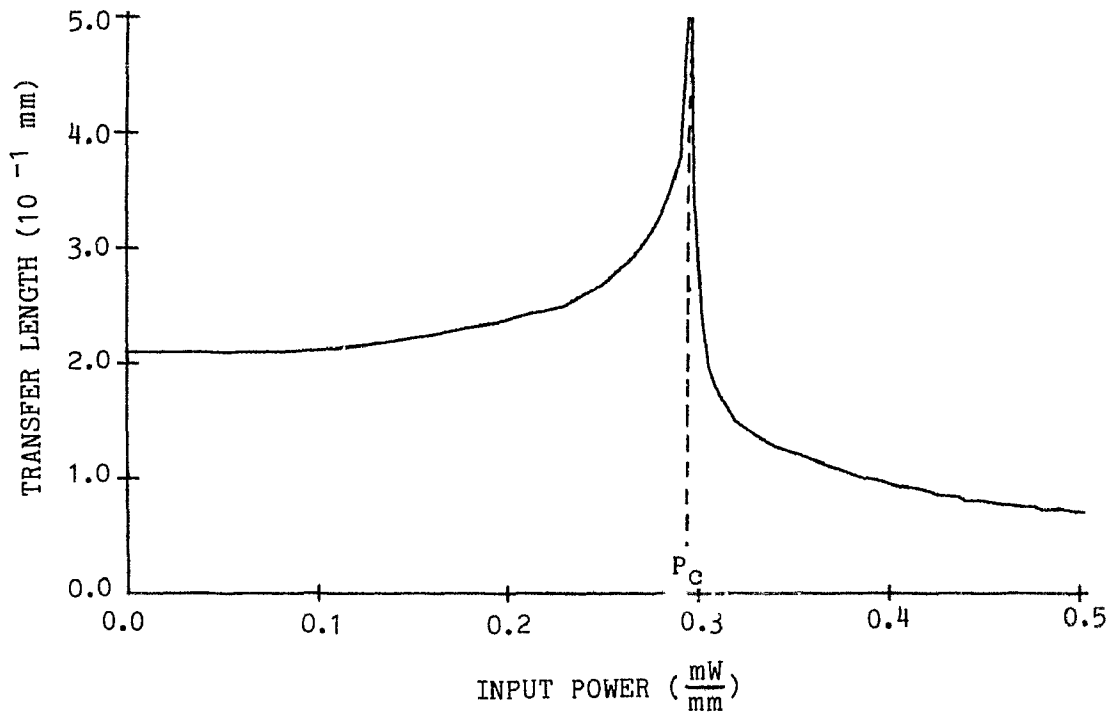
Figure 9.5: Power dependent nature of the transfer length.

The nature of the transfer length below and above P_c is shown in figure 9.5 with the assymptote occuring at $P_1(0) = P_c$. The flat region on the left of P_c corresponds to a device operating as a linear directional coupler. In this region all of the propagated power in the structure can completely transfer from the mode of guide 1 to the mode of guide 2. Just below and above P_c the drastically changing value of the transfer length illustrates the strong power-dependent nature of the nonlinear directional coupler. For input powers above P_c, full transfer of power from guide 1 to guide 2 is no longer possible.

Plots of output power for each waveguide versus input power as a function of the interaction length (figure 9.6), best display the power dependent nature of the structure. The solid trace represents the output power of guide 1 while the dashed trace represents the output power of guide 2. The value of P_c is indicated by an arrow on the input power axis. Each of these figures can be regarded as originating

0.05 mm further down the structure from the previous plot as shown in figure 9.7. Note that for the curve with $z \geq 0.3$ mm, rapid changes in the waveguide's output power occur for small changes in input power about P_c, and that P_c corresponds to the crossing point of the two curves (i.e., 50:50 power division between guides).

It can be seen from the features of the curves in figure 9.6 that devices such as all-optical switches, attenuators, transistors and logic elements can be designed[104]. Consider, for instance, the design of an all-optical switching element based on the power dependent curve of figure 9.6 E, with $z = 0.25$ mm. If the output power level from guide 1 is monitored, then an input power of 0.25 mW/mm will cause all the pow' to exit guide 2, which corresponds to the off state of the switch. On the other hand, increasing the power to 0.33 mW/mm will result in all the power exiting guide 1, corresponding to the on state of the switch.

The design of the switching element based on the curves of figure 9.6 is somewhat optimistic since the losses of the structure have not yet been included in our analysis. In the next section the losses of the structure are included in the analysis and the results compared to those of the lossless case.

9.3.3 Lossy Analysis

Optical absorption losses are essential in the MQW in order that the material exhibit a strong nonlinearity since the absorption of a photon is required to generate the exciton. This means that losses cannot be avoided by shifting the wavelength of operation too far off the exciton resonance peak or else a decrease in loss would result in a decrease in the optical nonlinearity. In terms of optical waveguide characteristics, the structure of figure 9.3 has to be analysed with n_3 being complex as well as optical intensity dependent. To incorporate losses into the analysis, the approach of Cada et. al.[105] uses analytical continuation of the dispersion equation from real to complex propagation constants and involves solving the wave equation for TE modes and applying appropriate boundary conditions to all interfaces. The
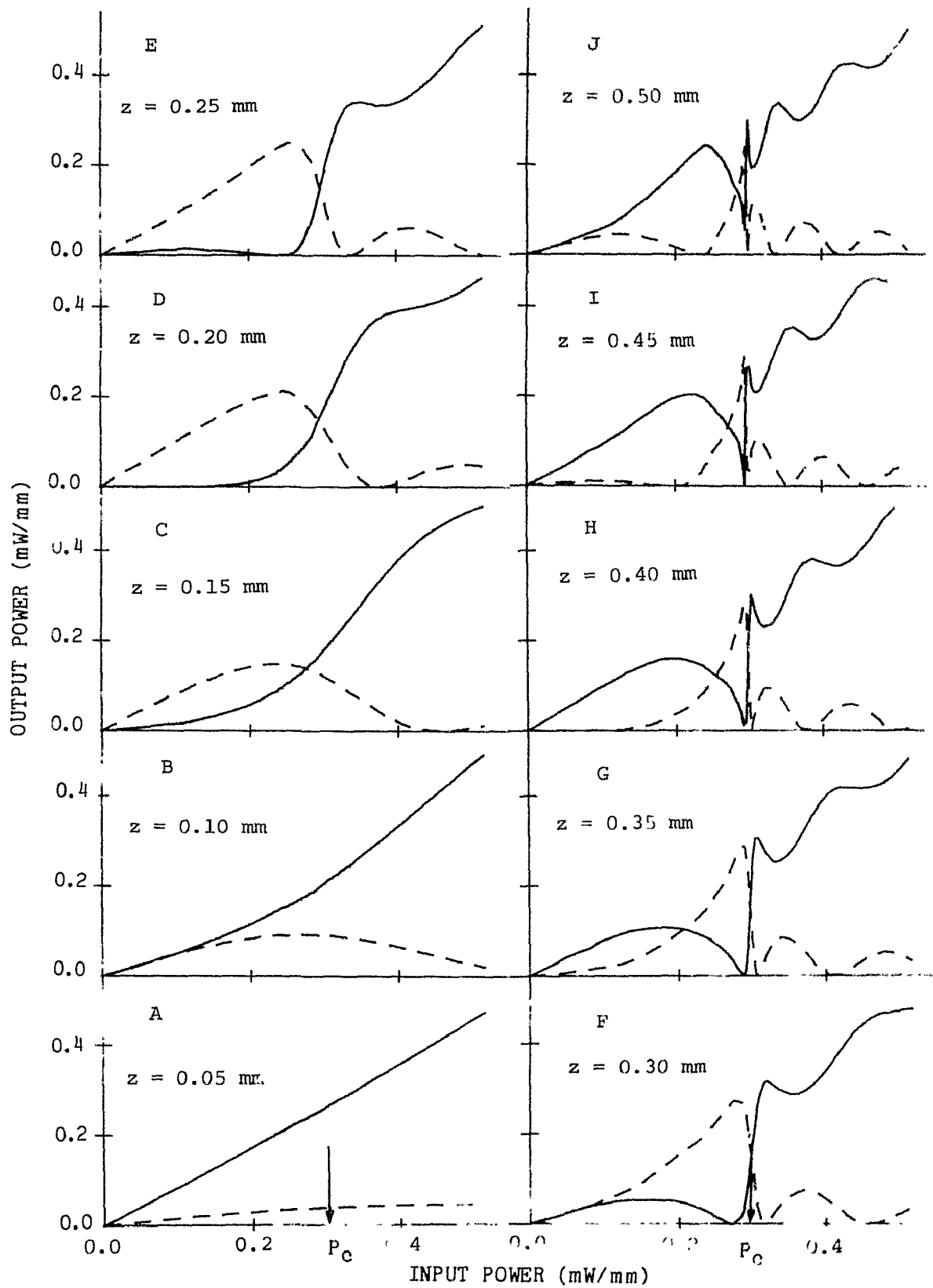
Figure 9.6: Output power from waveguides as a function of input power for specific interaction lengths, solid line - Launched guide (1), dashed line - Coupled guide (2).
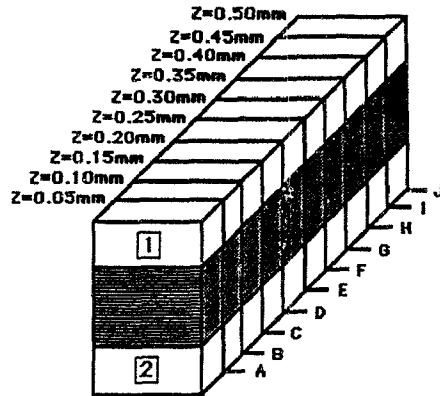
Figure 9.7: Sectioning of the nonlinear directional coupler in 0.05 mm lengths.

dispersion equation of the structure for real refractive indices and real propagation constants is found to be:

$$(\gamma_2^2(\gamma_1 C - \gamma_2 S)^2 + \gamma_3^2(\gamma_1 S + \gamma_2 C)^2)SH + 2\gamma_2\gamma_3(\gamma_1 S + \gamma_2 C)(\gamma_1 C - \gamma_2 S)CH = 0 \quad (9.29)$$

where

$$\gamma_2 = \sqrt{n_2^2 - (\frac{\beta}{k_o})^2} \quad (9.30)$$

$$\gamma_3 = \sqrt{(\frac{\beta}{k_o})^2 - n_3^2} \quad (9.31)$$

$$\gamma_1 = \sqrt{(\frac{\beta}{k_o})^2 - n_1^2} \quad (9.32)$$

$$S = sin(k_o\gamma_2 T) \quad (9.33)$$

$$C = cos(k_o\gamma_2 T) \quad (9.34)$$

$$SH = sinh(k_o\gamma_3 R) \quad (9.35)$$

$$CH = cosh(k_o\gamma_3 R) \quad (9.36)$$

Analytical continuation requires $n_3 = n_3' + i n_3''$ and seeks complex solutions for the propagation constant β, i.e., $\beta = \beta_r + i\beta_i$. It is noted that n_3'' is simply

related to the absorption loss of the MQW, α_n, through the relationship $\alpha_n = 2k_0 n_3''$. For analytical purposes the largest value of the highest absorption loss has been used and thus the changes in α_n with intensity have been neglected (α_n decreases with intensity at or close to the exciton resonance). Equation (9.29) has been solved by computer for our design parameters. The propagation loss, α_p, is related simply to the imaginary part of β, i.e., β_i through $\alpha_p = 2\beta_i$. An easy method of visualizing this loss term is to recall the nature of the loss mechanism of the metal cladding of chapter 6. Here the MQW is also treated as a cladding to the slab waveguide with real and imaginary components of the index of refraction.

A second loss mechanism has also been included which accounts for the loss in optical power for energy coupled from one waveguide to the other through the MQW. The experimental value of the loss coefficient for power propagating in the MQW has been taken as[4] $\alpha_n = 1/3$ E+04 cm^{-1}, which corresponds to a loss in the MQW of approximately 1 dB/μm. Both loss mechanisms have been considered in the lossy nonlinear analysis[106,107].

Figure 9.8 shows an infinitesimal segment (dz) of the nonlinear coupler used to perform numerical calculations with losses included. The input powers, P_1 and P_2, are known and may correspond to either the initial power launched or to the power division at any point along the structure. From the lossless analysis, the power coupled from guide 1 to guide 2 or from 2 to 1, (P_R), has been calculated for the interaction length of dz.

For no losses the total power at dz down the structure can be obtained as:

$$P_{1,dz} = P_1 - P_R \tag{9.37}$$

and

$$P_{2,dz} = P_2 + P_R \tag{9.38}$$

Next, losses are applied to each term such that in guide 1, P_1 - P_R is replaced by $(P_1 - P_R)e^{-\alpha_p dz}$ and in guide 2, P_2 is replaced by $P_2 e^{-\alpha_p dz}$, taking into account
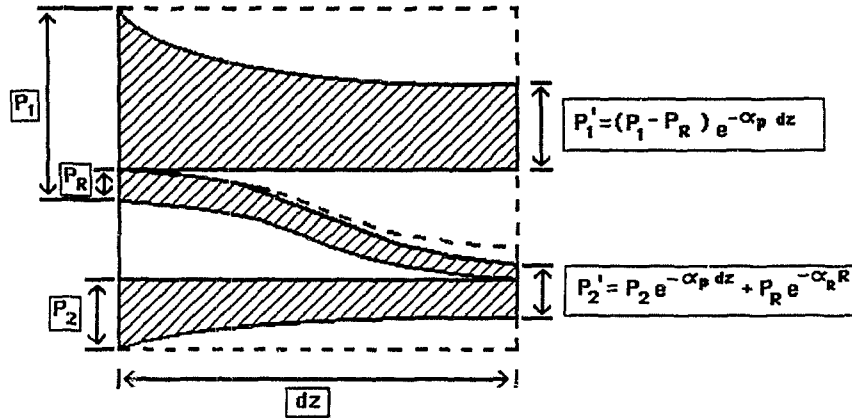
Figure 9.8: Power exchange and loss considerations.

the propagation losses. In guide 2 only, P_R is replaced by $P_R e^{-\alpha_R R}$, taking into account the cross coupling loss. The powers remaining at dz after the losses are included are now given by:

$$P_1' = (P_1 - P_R)e^{-\alpha_p dz} \tag{9.39}$$

and

$$P_2' = P_2 e^{-\alpha_p dz} - P_R e^{-\alpha_R R} \tag{9.40}$$

The new power levels P_1' and P_2' can now be used as the input values for the next infinitesimal segment of the structure. Repeating the procedure, the power in the waveguides versus interaction length graphs (figures 9.9 to 9.14) have been generated for our design parameters given in the lossless analysis section. The corresponding lossless curves are also included for comparison purposes.

The following features can be observed from the sets of curves:

- For input powers below P_c, the lossy transfer power curves are similar in appearance to those of the linear coupler with losses discussed above. However, for
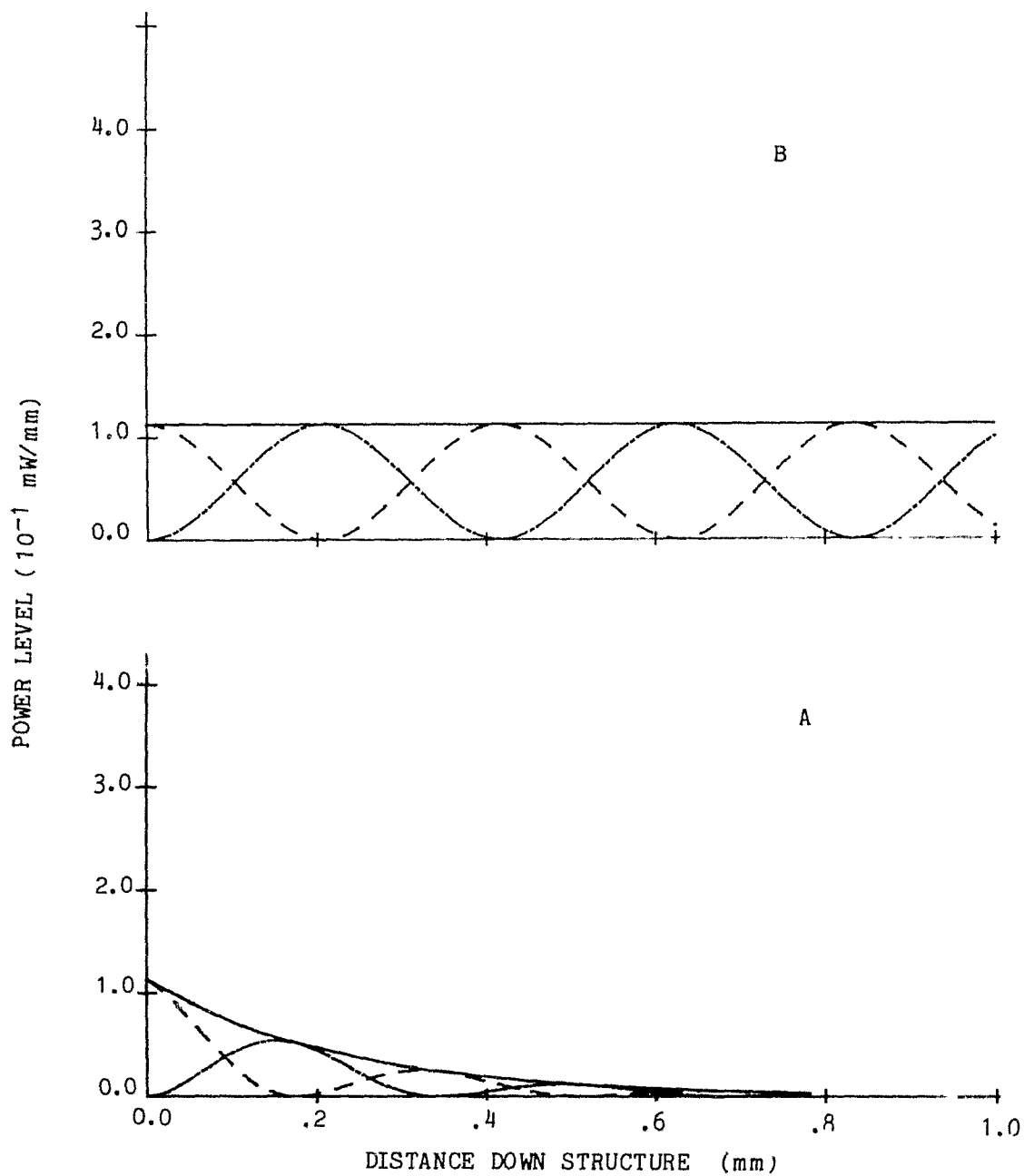
Figure 9.9: Power level versus interaction length, $P_1(0) = 0.12$ mW/mm : A - lossy, and B - lossless curves. Solid line - total power, dashed line - power in guide 1. Dot-dashed line - power in guide 2.
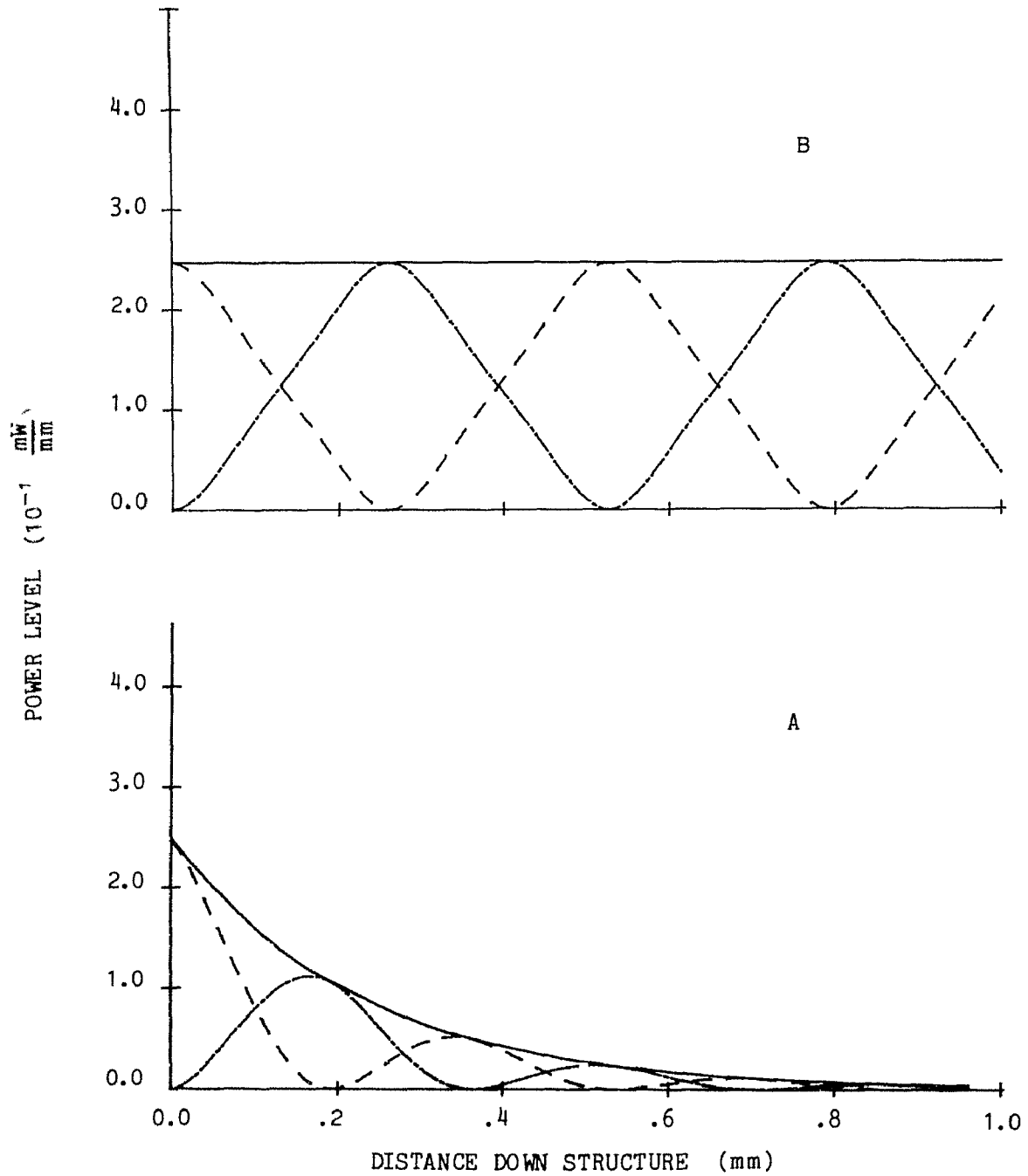
Figure 9.10: Power level versus interaction length, $P_1(0)$ = 0.25 mW/mm : A - lossy and B - lossless curves. Solid line - total power, dashed line - power in guide 1. Dot-dashed line - power in guide 2.
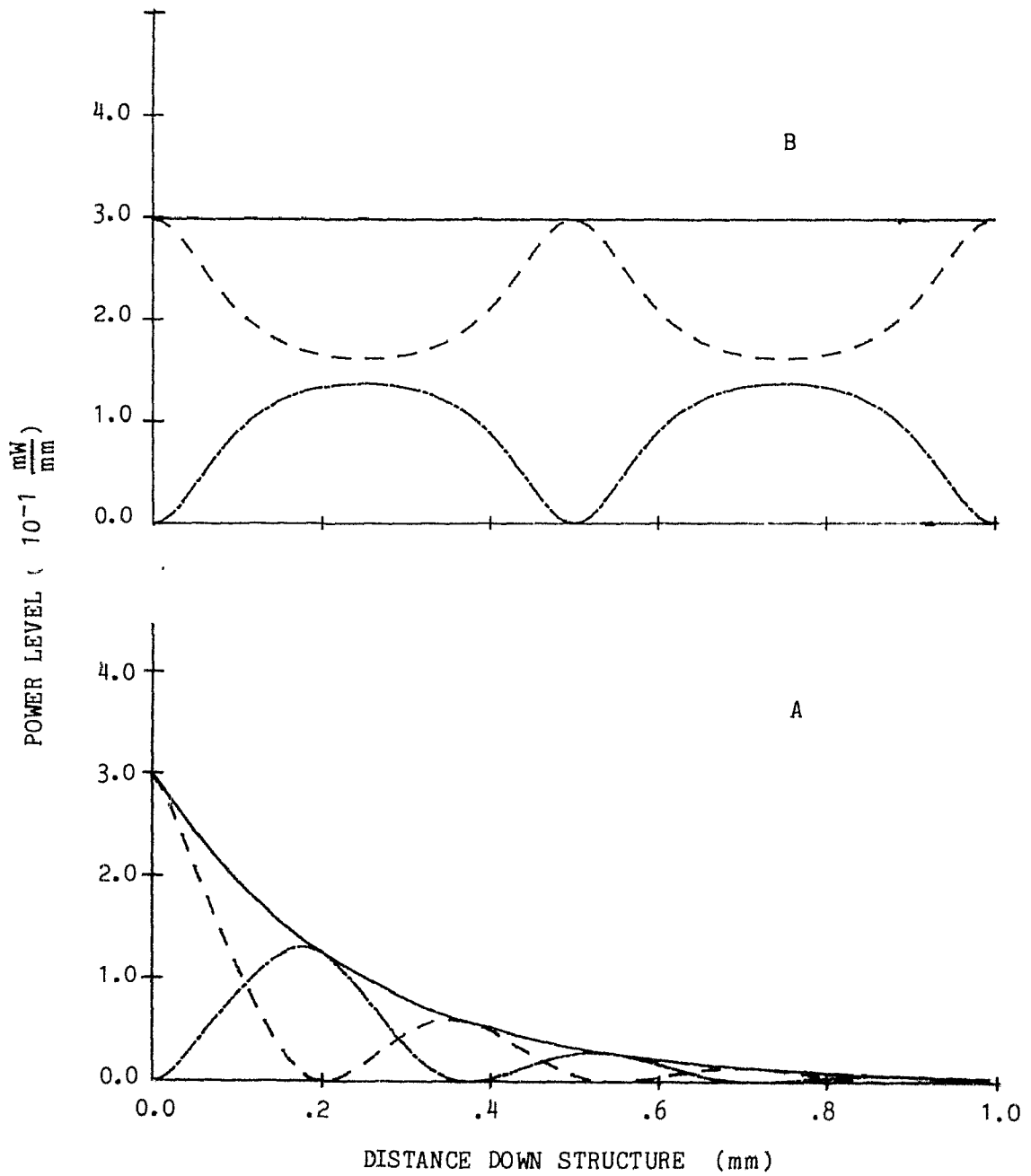
Figure 9.11: Power level versus interaction length, $P_1(0) = 0.30$ mW/mm
: A - lossy and B - lossless curves. Solid line - total power, dashed line - power in guide 1. Dot-dashed line - power in guide 2.
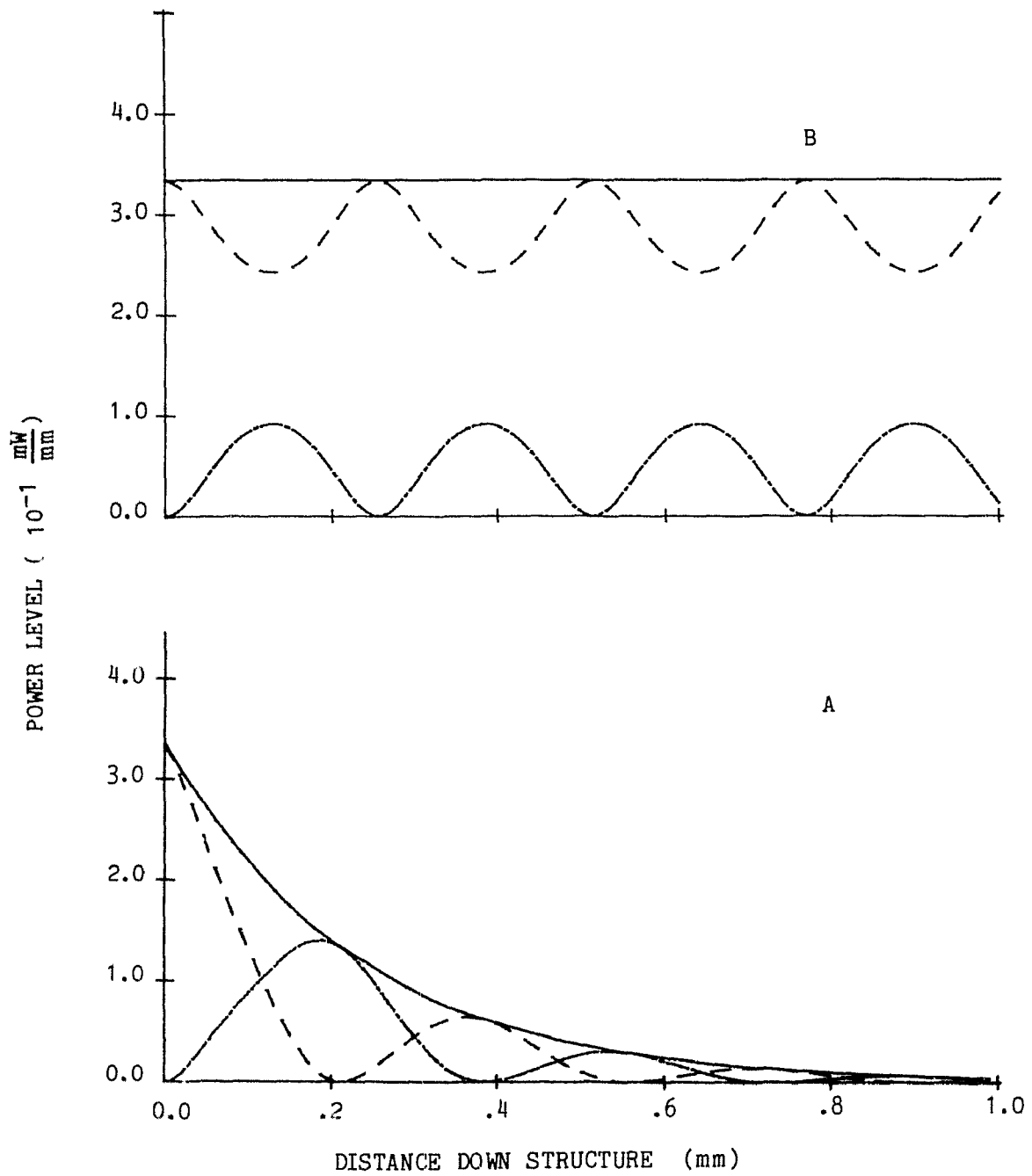
Figure 9.12: Power level versus interaction length, $P_1(0) = 0.34$ mW/mm : A - lossy and B - lossless curves. Solid line - total power, dashed line - power in guide 1. Dot-dashed line - power in guide 2.
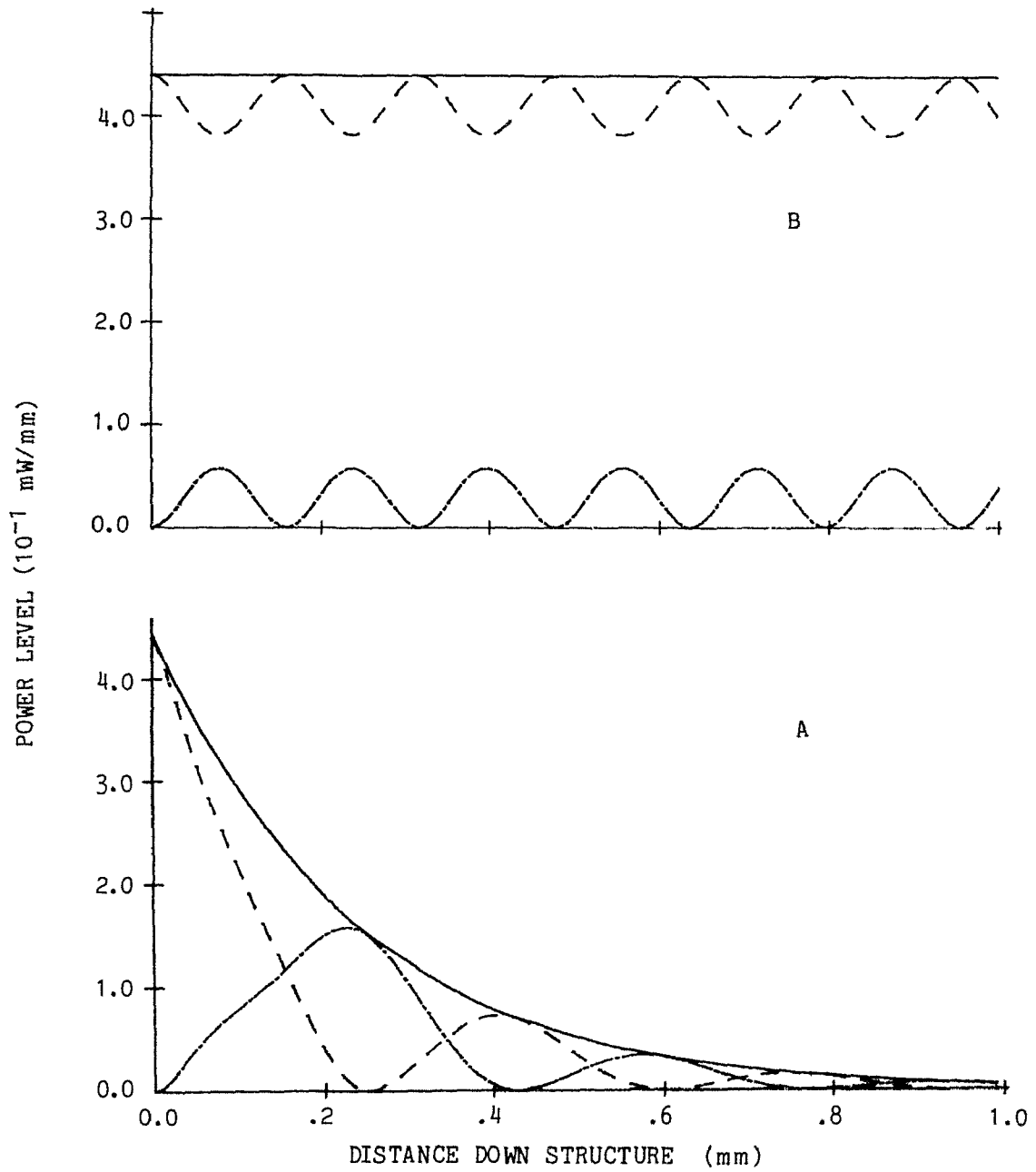
Figure 9.13: Power level versus interaction length, $P_1(0) = 0.45$ mW/mm
: A - lossy and B - lossless curves. Solid line - total power, dashed line -
power in guide 1: Dot-dashed line - power in guide 2.
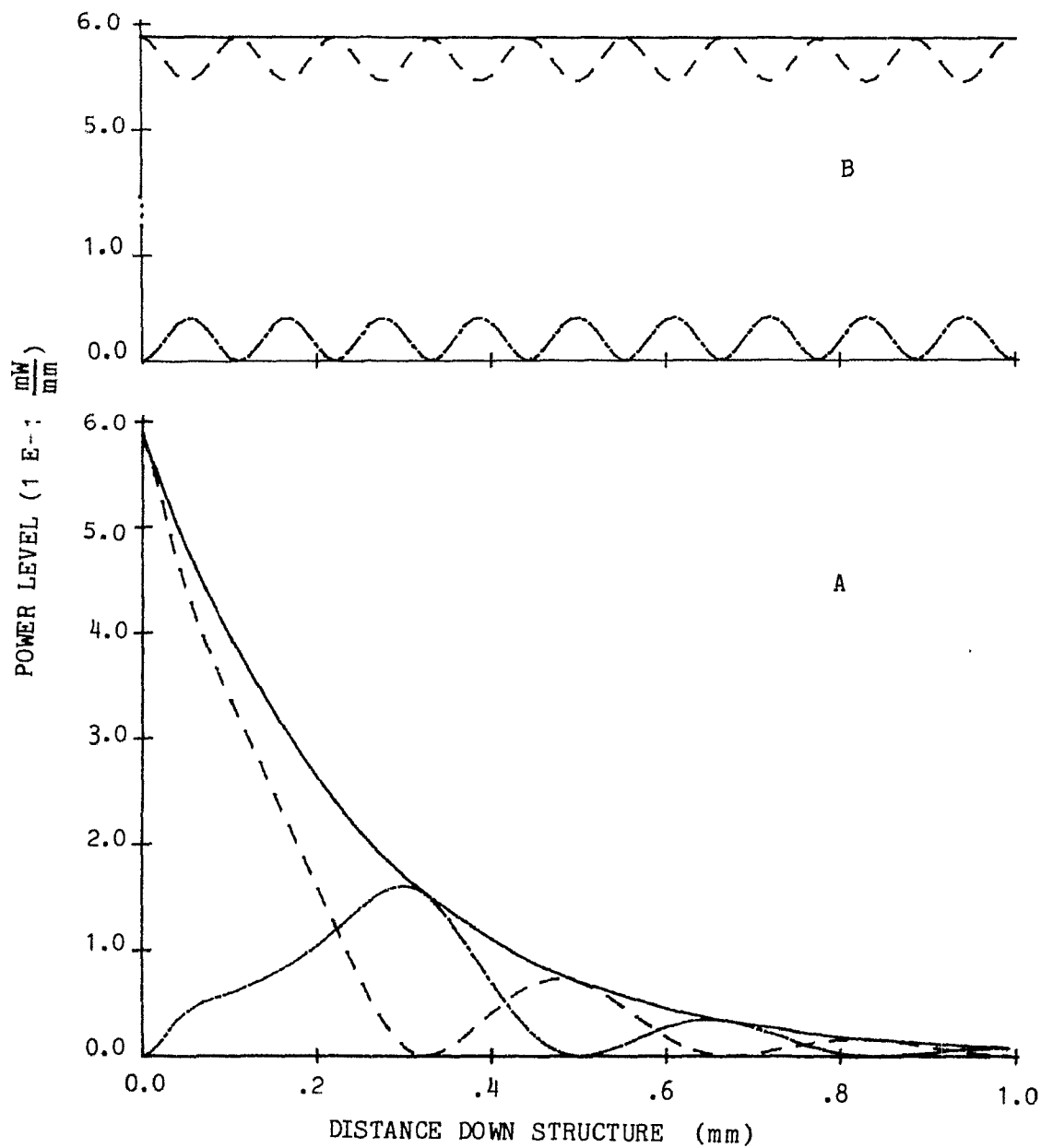
Figure 9.14: Power level versus interaction length, $P_1(0) = 0.59$ mW/mm A - lossy and B - lossless curves. Solid line - total power, dashed line - power in guide 1. Dot-dashed line - power in guide 2.

the nonlinear coupler with losses described here, the total power curve is no longer a simple exponential decay but is complicated by the cross coupling losses through the MQW.

- An infinite full power transfer length at P_c is no longer observed when losses are included. The losses of the structure gradually attenuate the total power to lower power levels where complete transfers between the waveguides are once again possible.

- For input powers above P_c a full transfer of power from guide 1 to guide 2 is observed. This is contrary to the lossless case discussed above where only partial transfers of power from guide 1 to guide 2 are possible at these input levels. The nature of the lossy curves results from the gradual attenuation of the total power to a level below P_c, where complete tranfers are again possible. Note that the first full power transfer length (guide 1 to guide 2) is longer than the second full power transfer length (guide 2 to guide 1) for these input power levels. The asymmetry is due to the requirement that the total power must first be attenuated below P_c before complete exchange is possible. The curve of the first full transfer length versus input power is shown in figure 9.15. This curve shows that the full transfer length increases with input power and shows no asymptote at P_c. In the lossy case the concept of P_c is retained to mark the boundary between full and partial transfer input power levels.

- For input powers above P_c in the lossy case, structure is observed in the power level curve of guide 2 before the first full transfer length. This structure originates from the partial periodic exchange of power as has been observed in the lossless case, but here the losses of the structure tend to overshadow these features. Figure 9.16 shows a curve where the propagation losses have been excluded but cross coupling losses are included. The partial periodic exchange of power characteristic above P_c is more clearly displayed in this curve.

From the sets of figures 9.9 to 9.14, the 3 dB position along the structure
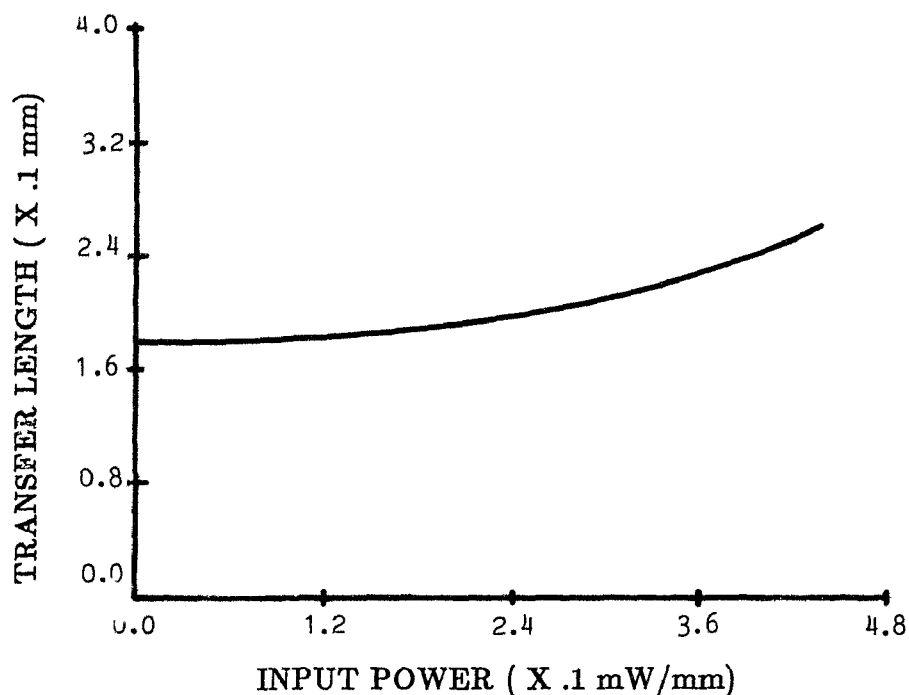
Figure 9.15: Full transfer length versus input power for a lossy nonlinear directional coupler.

has been plotted in figure 9.17 as a function of the input power.

It shows that the 3 dB point is a weak function of the input power as observed by the small slope of the curve. When devices are designed using MQW's in nonlinear coupler configurations, the length of interaction is fixed. Figure 9.17 shows that, independent of the operating power levels chosen, the intrinsic losses of the device will remain relatively unchanged over large input power variations.

In order to discuss potential device applications, the curves of output power versus input power for various interaction lengths have been plotted in figure 9.18. These curves show that changes in output power as a function of input power are more gradual than those of the lossless case (figure 9.6). Devices can be designed based on these theoretical curves of figure 9.18. In particular the lossless optical switch previously discussed is redesigned and an all-optical "AND-OR" logic gate is discussed.
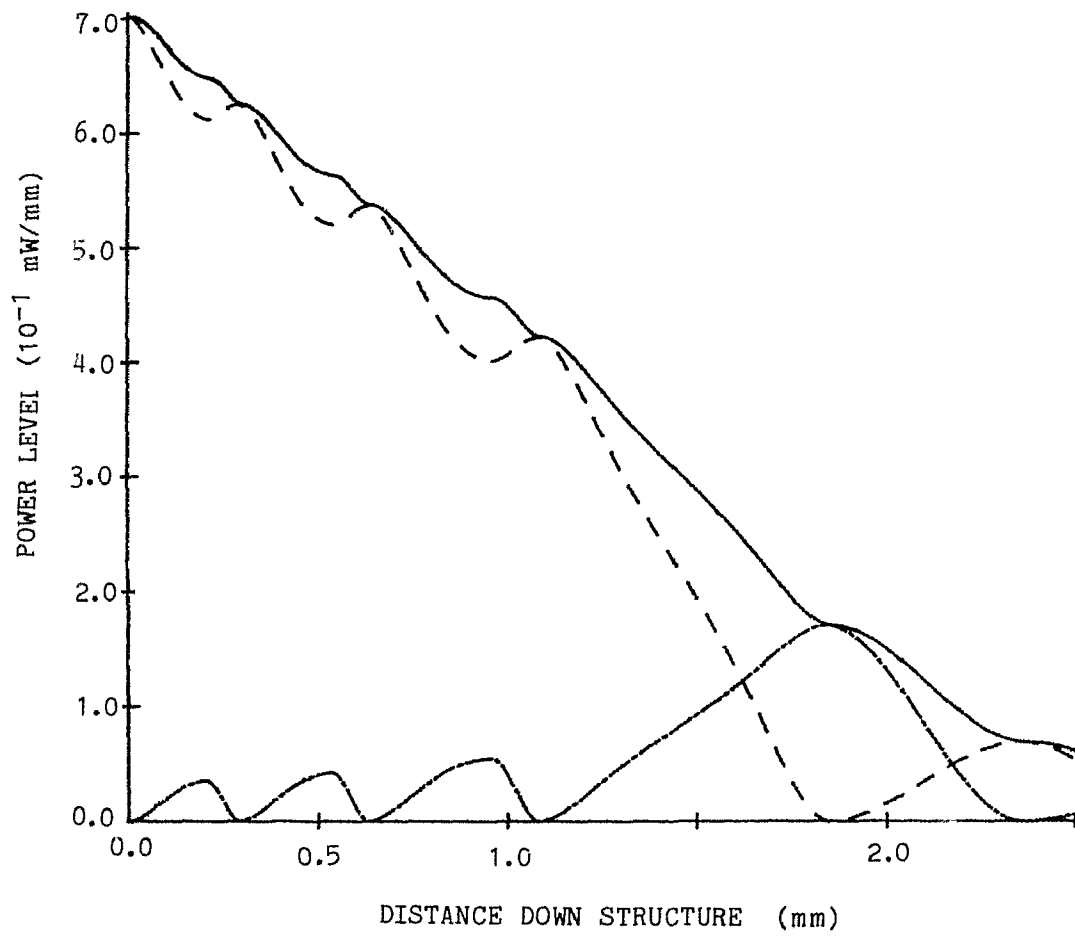
Figure 9.16: Power versus position curve with the cross coupling losses only included.
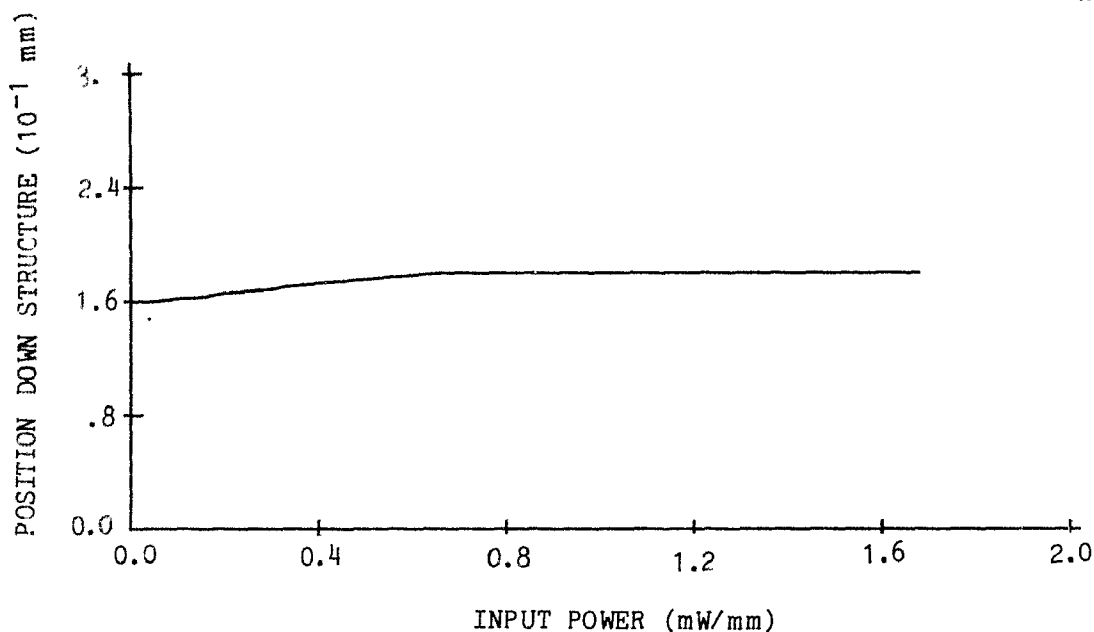
Figure 9.17: 3 dB position for the nonlinear directional coupler analysed.

9.3.4 Optical Switching Element

A power controlled optical switch can be designed from figure 9.18 F, with z = 0.30 mm for example. For an input power of 0.4 mW/mm the power exits guide 2 only. If the output power of guide 1 is monitored, this corresponds to the off state of the switch. When the input power is increased to 1.2 mW/mm, 80 percent of the power exits guide 1 and 20 percent exits guide 2 and may correspond to the on state of the switch. A 100 percent power switch could be designed if the interaction length were longer, z > 0.50 mm. However the device would have an intrinsic loss greater than 9 dB due to absorption while the z = 0.30 mm device has only a 6 dB intrinsic absorption loss. A trade off between high performance and low loss has thus to be sought.

9.3.5 "AND-OR" Optical Gate

This device can be designed based on the information of figure 9.18 E, z =
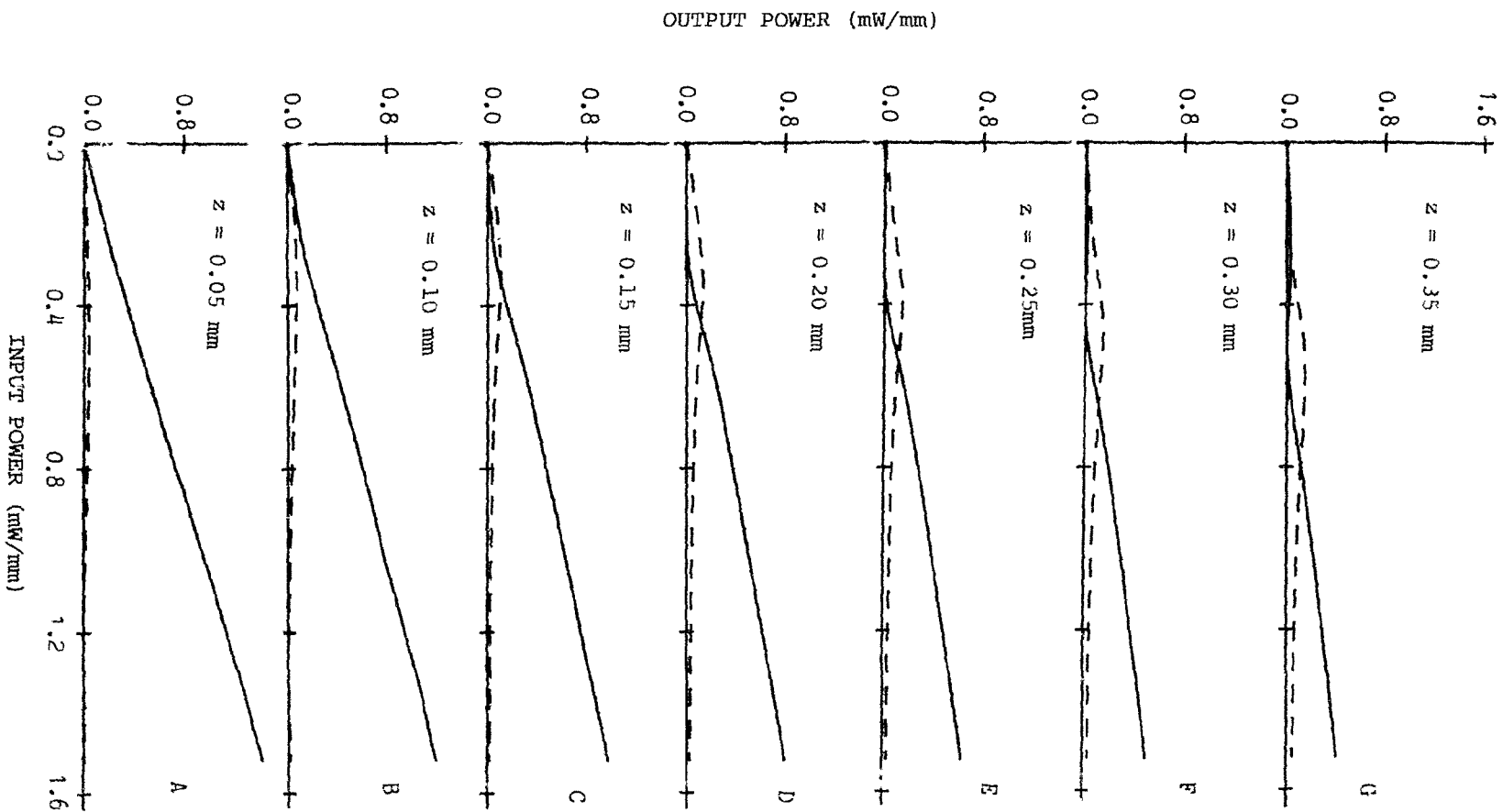
Figure 9.18: Output power of guides versus input power to structure for various exchange lengths, solid trace - guide 1, Dashed trace - guide 2.

0.25 mm. Suppose that a Y branch coupler is used as input to guide 1, combining two separate signals (A, B) into one optical power. If a logic "1" is chosen as 0.25 mW/mm and a logic "0" is chosen as 0.00 mW/mm, the following truth table for guides 1 and 2 can be established from the figure.

Table 9.1

Logic level for each input to guide 1		Outputs of the guides	
A	B	1	2
0,	0	0	0
0	1	0	1
1	0	0	1
1	1	1	1

From guide 1, the only situation where any power exits the guide is that when both inputs provide 0.25 mW/mm to the total input power. This type of output is characteristic of the "AND" function. The output of guide 2 is characteristic of the "OR" function. However for the gate to work properly the threshold level for distinguishing a "1" from a "0" must be carefully chosen.

9.4 Summary

In this chapter it has been shown that the nonlinear directional coupler must be analyzed with both the cross coupling and the propagation loss mechanisms included. The power remaining in the waveguides versus the interaction length have been shown in figures 9.9 to 9.14 and in the lossless case the coupling features of the structure depend highly on P_c, while for the lossy case, P_c indicates a power level for which the propagated power must attenuate below before full exchange of power between the waveguides becomes possible. With the losses included in the analysis the power in the guides versus interaction length curves strongly resemble

those of the linear directional coupler with losses of figure 9.2. The lossless analysis shows that for an input power level of P_c an infinite full power transfer length is expected with full power exchange possible for input powers below P_c and only partial exchange of power possible for input powers above P_c. In the lossy analysis the transfer length monotonically increases with increased input power and full exchange of power is always possible.

The design of an all-optical switch using both the lossless and lossy curves has also been discussed. It has been shown that similar operational features are obtained when one of the waveguide's outputs is monitored as the input power is varied. The lossy switch, however, contains losses and thus a tradeoff between device performance and power loss has to be sought. It is shown from the lossy curves that an all-optical logic gate can be designed from the nonlinear directional coupler analyzed, with both AND and OR functions possible on the same chip at the same time. The 3 dB loss per 1.5 mm propagation length is a considerable reduction in loss as compared to previous works where the losses have been in the dB/μm range and the MQW has formed the waveguides[108]. It is expected that the nonlinear directional coupler will play a key role in future optical systems since it is simple in structure, can be manufactured by techniques currently available, can be used in a number of design configurations and can be integrated with sources and detectors onto a single substrate of GaAs.

CHAPTER 10. CONCLUSION

Several areas of integrated-optic technology have been addressed by focusing attention on waveguides with claddings, propagations at an angle to the optical axis, gaps in waveguides, and a nonlinear directional coupler[*].

The effect of the metallic cladding overlay was to introduce an imaginary component to the index of refraction which resulted in an imaginary component to the propagation constant. This new factor led to high losses in the TM mode's guided optical power as a function of the interaction length while leaving the TE mode's guided power relatively unaffected. Several integrated-optic devices, which made use of this principle, have been discussed including polarizers, sensors and an electro-wetting-optical switch. The sensors represent one of the first applications of integrated-optics in this arena.

When the guided light was propagated at an angle to the optical axis of the crystal, the anisotropy of the substrate was shown to introduce losses to the extraordinary modes when the propagation angle became greater than a well defined critical angle. The loss of optical power depended on the interaction length and could be expressed in terms of a loss coefficient and linked to the imaginary propagation constant. Several devices have been designed, based on the losses due to angle propagations, and include the polarizer, mode selector, polarization rotator and electro-optic switch. The switch shows an 84 % depth of modulation for a 1.5 V/μm applied electric field between the controlling electrodes.

For gaps in the waveguides studied, the power coupling expressions have been

---

[*] See the appropriate chapter for complete summary of results

163

derived in the appendices and shown to be of a form that does not permit their evaluation. Experimental results of power coupling measurements show that the loss in power as a function of the gap length can be fitted to an exponential function. This allows the identification of an attenuation coefficient which can be related to an imaginary component in the propagation constant. An integrated-optic device has been shown to be capable of altering the power coupling across the gap by changing the index of refraction between the waveguide endfaces. The theoretical treatment of the nonlinear evanescent directional coupler shows that losses must be included in the analysis. As a result, completely different output characteristics have been obtained between the lossless and lossy cases. It has been shown that this structure can react depending on the input light intensity and enables the design of all-optical devices such as switches and logic gates. From a single chip it is shown that both the "AND" and the "OR" logic functions can be obtained simultaneously.

Observations on these waveguide geometries indicate that the guiding properties of optical waveguides are contained in the mode's propagation constant which is determined from the index of refraction profile, polarization state and wavelength of light. The changing of one or more of the waveguide's parameters would result in a change of the propagation constant and alter the guided light optical properties. When the changes are produced in a controlled fashion, integrated-optic devices result.

The future of integrated-optics looks promising. The first commercial devices have appeared on the market in the last few months. The possibility of mass production techniques borrowed from the semiconductor industry will reduce the component cost while making devices feasible in optical systems applications. In this research the geometries examined have been configured into devices such as sensors, switches, attenuators and all-optical devices such as logic gates and switches. The waveguide and device configurations studied here will find applications in future systems since they are simple in structure and can be built in a few steps.

Work still remains in the field of integrated-optics. Of particular interest to this research is the work proceeding on the theoretical and experimental investigations of metallic cladding overlays and the electro-wetting switch between scientists at Dalhousie University and those of the Electrical Engineering Section of the National Research Council in Ottawa. Work is underway at the Technical University of Nova Scotia and Bell Northern Research Laboratories to build and test MQW devices and verify the predictions of the nonlinear directional coupler. For off axis beam propagation, the leaky properties of channel waveguides still remain to be examined, while for gaps in the guides the theoretical coupling expressions of appendices C and D, based on the radiation mode treatment, have yet to be evaluated numerically. Any of these areas of research can easily provide the bases for other Ph. D. theses.

APPENDIX A. OFF-AXIS PROPAGATION THEORY

A.1 Introduction

.

In chapter 3 the isotropic, lossless slab waveguide has been analyzed theoretically and the releaevent features discussed. TE and TM polarized modes have been shown to be valid solutions of the wave equation. In this appendix details of the anisotropy of the crystal substrate and waveguide are introduced in the slab waveguide analysis. New features not observed in the isotropic waveguide treatment are also discussed. To gain insight into the physics involved in these waveguides, the step index slab structure is considered.

A.2 Step Slab Anisotropic Waveguide

The waveguide structure is shown in figure A.1. The three layers consist of an isotropic superstrate (air), an anisotropic substrate ($LiNbO_3$), and an anisotropic guiding layer formed by uniformly doping the substrate to a depth $-t_g$. The z axis is chosen as the propagation direction throughout the analysis.

The wave equation, developed in chapter 3 equation (3.13), can no longer be used in its final form since $\mathbf{D}$ and $\mathbf{E}$ are now related by a dielectric tensor (2.2) as
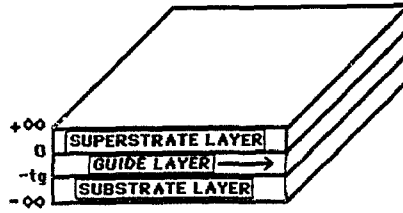
Figure A.1: Anisotropic step index slab waveguide.

opposed to a scalar dielectric constant. The usable form of the wave equation is:

$$\nabla X \nabla X \mathbf{E} = \frac{-1}{c^2} \epsilon \frac{\partial^2 \mathbf{E}}{\partial t^2} \qquad (A.1)$$

where, in the principle coordinate system, ϵ is of the form:

$$\epsilon = \begin{pmatrix} \epsilon_x & 0 & 0 \\ 0 & \epsilon_y & 0 \\ 0 & 0 & \epsilon_z \end{pmatrix} \qquad (A.2)$$

with $\epsilon_x = \epsilon_y = n_o^2$ and $\epsilon_z = n_e^2$. The solution to the wave equation for an arbitrary propagation direction is not developed[1] since the crystal cuts used restrict the wave propagation to planes formed in the Y-X axis (Z-cut crystal) or the Y-Z axis (X-cut crystal). Waveguides formed in the X-Z plane (Y-cut crystals) are equivalent to waveguides in the Y-Z plane for LiNbO$_3$ and the analysis is not repeated.

A.2.1 X-cut Crystals

The waveguide geometry is shown in figure A.1, and the coordinate system and optical axis are oriented as shown in figure A.2. The optical axis (Z) forms an angle with respect to the propagation axis (z) and lies in the (y,z) plane. In the

---

[1]See references [109] and [110] for general development
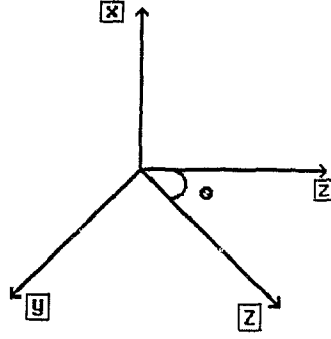
Figure A.2: Coordinate system for X-cut waveguide.

(x,y,z) coordinate system, the rotation tensor T (equation 2.4) reduces to:

$$T = \begin{pmatrix} 1 & 0 & 0 \\ 0 & cos(\theta) & sin(\theta) \\ 0 & -sin(\theta) & cos(\theta) \end{pmatrix} \qquad (A.3)$$

The anisotropic dielectric tensor can be rewritten in the (x,y,z) coordinate system using equation (2.5) as:

$$\epsilon = \begin{pmatrix} n_x^2 & 0 & 0 \\ 0 & n_y^2 & \delta \\ 0 & \delta & n_z^2 \end{pmatrix} \qquad (A.4)$$

where

$$n_x^2 = n_o^2 \qquad (A.5)$$

$$n_y^2 = n_o^2 cos^2(\theta) + n_e^2 sin^2(\theta) \qquad (A.6)$$

$$n_z^2 = n_e^2 cos^2(\theta) + n_o^2 sin^2(\theta) \qquad (A.7)$$

$$\delta = (n_e^2 - n_o^2) sin(\theta) cos(\theta) \qquad (A.8)$$

Guided mode solutions of the slab wave equation are characterized by their field dependence in the x direction, which is assumed to be $e^{\gamma x}$ for fields in the substrate $(x \le -t_g)$ and superstrate $(x \ge 0)$, and $e^{\pm \gamma x}$ for fields in the film $0 \le x \le -t_g$[111-113]. In these profiles γ is the transverse propagation constant and we recall, from chapter 3 for TE modes in a step index slab waveguide, that γ represents p in the substrate, q in the superstrate and h in the guiding layer. It is assumed as

usual that the propagation factor is $e^{-i(\omega t - \beta_m z)}$ and β_m is the propagation constant of the mth mode in the z direction. With this notation the wave equation for the anisotropic layer can be written as a 3 x 3 matrix of the form[111-114]:

$$0 = \begin{pmatrix} (\beta_m^2 - k_o^2 n_x^2) & 0 & -i\beta_m(\pm i)\gamma \\ 0 & (\beta_m^2 - (\pm i)\gamma^2 - k_o^2 n_y^2) & -k_o^2\delta \\ -i\beta_m(\pm i)\gamma & -k_o^2\delta & ((\pm i)\gamma^2 - k_o^2 n_z^2) \end{pmatrix} \begin{pmatrix} E_x \\ E_y \\ E_z \end{pmatrix} \quad (A.9)$$

The term $(\pm\, i)$ preceding the γ is to be included if the fields are in the film, but is replaced by 1 for fields in the anisotropic substrate. For wave components in the superstrate, $n_x = n_y = n_z$ and ϵ is a scalar and the wave equation (3.11) can be used. From chapter 3 it was identified that TE modes had no E_x or E_z components, while for TM modes the E_y component was absent. In the above equation the E_y component is coupled to the E_z component when $\delta \neq 0$ and thus the propagation modes will contain all three field components. It is instructive to look first at solutions obtained for γ in (A.9) by setting $\delta = 0$. This corresponds to the case where $\theta = 0$ or 90 degrees. Under these conditions the E_y and E_z components are uncoupled and these modes can exist separately. The solutions in the guiding layer are:

$$(\pm i)\gamma_{TE}^2 = (\beta_m^2 - k_o^2 n_y^2) \quad (A.10)$$

and

$$(\pm i)\gamma_{TM}^2 = (\frac{n_z}{n_x})^2(\beta_m^2 - k_o^2 n_x^2) \quad (A.11)$$

For arbitrary θ, $\delta \neq 0$, the solutions for γ can be written as:

$$\gamma_o^2 = (\frac{a}{a+b})\gamma_{TE}^2 + (\frac{b}{a+b})\gamma_{TM}^2 \quad (A.12)$$

and

$$\gamma_e^2 = (\frac{a}{a+b})\gamma_{TE}^2 + (\frac{a}{a+b})\gamma_{TM}^2 \quad (A.13)$$

where a $= (\beta_m^2 - k_o^2 n_z^2)\cos^2(\theta)$, b $= k_o^2 n_z^2 \sin^2(\theta)$, and γ_{TE} and γ_{TM} are evaluated using equation (A.5 to A.8) for the angle of propagation θ. Equation (A.12 and A.13) show that the general solutions for γ are circular combinations of the uncoupled TE and TM mode solutions of (A.7 and A.8). This brings out the hybrid nature of the exact solutions of γ_o and γ_e. Note that the nature of the solutions changes as the angle θ is varied: γ_o is pure TE for $\theta = 0$ and pure TM for $\theta = 90$ degrees.

It can be shown through algebraic manipulation that γ_o is angle independent, a requirement if the definition of ordinary modes is to be applied, while for γ_e it is a function of angle, consistent with the definition of extraordinary modes propagating in the crystal and waveguides[115]. The electric fields associated with the two solutions may be readily obtained. The relationship between E_y and E_z is obtained from (A.9). For $\gamma = (\pm i)\gamma_o$, this reduces to:

$$E_z = -tan(\theta)E_y \qquad (A.14)$$

and for $\gamma = (\pm i)\gamma_e$:

$$E_z = \frac{-\beta_m^2 - k_o^2 n_x^2}{k_o^2 n_x^2 tan(\theta)} E_y \qquad (A.15)$$

Equation (A.14) shows that the γ_o solution is always perpendicular to the optical axis. Using the index ellipsoid developed in chapter 2 implies that this field component is polarized in the plane with constant radius vector n_o, and thus the component encounters the angle independent index of refraction.

Equation (A.15) shows that for γ_e solutions the electric field direction depends on β_m. These fields contain a component which is polarized in a plane formed by the optical axis of the index ellipsoid and encounters the angle dependent index of refraction. It is known from the theory of homogeneous plane waves propagating in anisotropic media that the extraordinary wave propagates with a small angle[116] between propagation vector **K** and Poynting vector **S**. The same small angle occurs between the directions of **E** and **D**. Rewriting $E_z/E_y = A$, and using **D** $= \epsilon$ **E** and
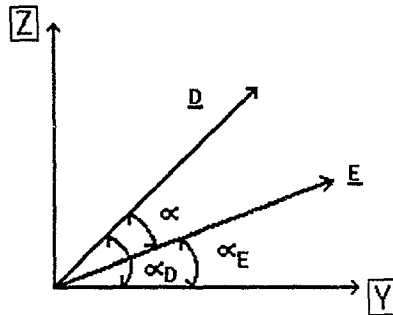
Figure A.3: Definition of propagation angles α_E, α_D and α

neglecting the x components, equation (2.2) becomes:

$$D_y = (n_y^2 + \delta A)E_y \qquad (A.16)$$

$$D_z = (\delta + n_z^2 A)E_y \qquad (A.17)$$

The angles α_E and α_D between the components **E** and **D** in the (y,z) plane and the y axis, shown in figure A.3, are given by:

$$tan(\alpha_E) = A \qquad (A.18)$$

$$tan(\alpha_D) = \frac{\delta + n_z^2 A}{n_y^2 + \delta A} \qquad (A.19)$$

The angle $\alpha = \alpha_E - \alpha_D$ is then given by:

$$tan\alpha = \frac{\delta A^2 + A(n_y^2 - n_z^2) - \delta}{n_z^2 A^2 + 2\delta A + n_y^2} \qquad (A.20)$$

Equations (A.14) and (A.15) can be used to further evaluate the angle α. For the ordinary mode $((\pm i)\gamma_o = \gamma$ and using (A.14), $\alpha = 0$, which implies that for this mode **E** and **D** are parallel. For the extraordinary mode $(\pm i)\gamma_e = \gamma$, α is given by:

$$tan(\alpha) = \frac{\delta C}{(n_o^2 sin^2(\theta) + C^2 n_e^2 cos^2(\theta)} \qquad (A.21)$$
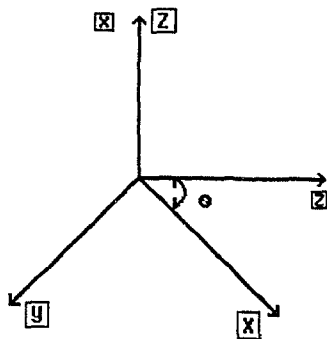
Figure A.4: Coordinate system used for the Z-cut waveguide.

where $C = 1 - (\frac{k_o n_x}{\beta_m \cos(\theta)})^2$. For these solutions we see that $\mathbf{E}$ and $\mathbf{D}$ are not parallel by an amount proportional to the anisotropy. Thus the energy will propagate at a small angle to the z axis.

A.2.2 Z-cut Crystals

Analysis of the Z-cut crystal closely follows that of the X-cut crystal above. The relationship between the principle axis system and the E field coordinate system is shown in figure A.4, with the slab waveguide of figure A.1 contained in the (X,Y) plane. The angle θ is measured between the X axis and the z axis. The dielectric tensor for this orientation is given by:

$$\epsilon = \begin{pmatrix} n_x^2 & \delta & 0 \\ \delta & n_y^2 & 0 \\ 0 & 0 & n_z^2 \end{pmatrix} \qquad (A.22)$$

where $\delta = (n_z^2 - n_y^2)\cos(\theta)\sin(\theta)$. For LiNbO$_3$, where $n_y = n_z = n_o$ and $n_x = n_e$, then $\delta = 0$ for all angles of propagation. This implies that the dielectric tensor is diagonal and as a result the TE and TM modes can propagate independently for this waveguide/crystal geometry. The TE mode will be polarized in the waveguide plane and propagate in the z direction. It will correspond to the ordinary mode since
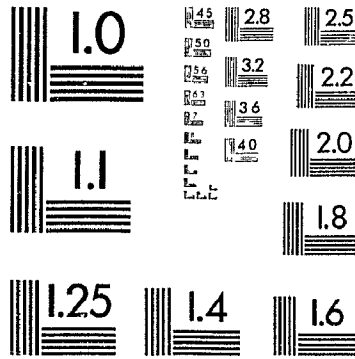
it encounters the ordinary index of refraction of the index ellipsoid for all angles of propagation. The TM mode contains the E_x component and a component along the z direction. This mode corresponds to the extraordinary mode since the electric field component is perpendicular to the plane of the waveguide and polarized along the Z axis.

APPENDIX B. WAVEGUIDE INTERCONNECTION LOSS MECHANISMS

In coupling single mode fibres to integrated-optic waveguides, there are a large number of mechanisms which influence the coupled power. The major loss mechanisms include: Fresnel reflection, Fabry Perot cavity resonances, alignment, modal mismatch, and end termination imperfections. Rather than give the details of each loss mechanism here, several papers and books have been cited in the references[117-128].

APPENDIX C. THE COUPLING EXPRESSION

C.1 Introduction

In this appendix is derived, for the first time, the general expression for the coupled power of one waveguide to another waveguide separated by a gap geometry as shown in figure C.1. To account for the coupled power, modal analysis in the separate regions must be employed. The coupling model for the derived expression contains the following assumptions:

1) In region (I), there are guided modes only while region (II) contains both the substrate and superstrate continuous spectrum of modes. In region (III) there is the possibility of guided modes as well as the continuum of substrate and air modes.

2) At the interfaces (I)-(II) and (II)-(III), there is assumed to be no reflected powers. This is a good approximation since the index of refraction change is small at the interfaces ($\Delta \approx 1\%$, reflection coefficient ≈ 5 E-04) and is graded in nature.

3) The mode pattern propagating in region (I) is present unchanged at the interface $z = 0$. That is, the profile in the guide is continuous across the interface. This results from the continuity conditions of the field components across the interface and no back-reflected component is assumed.

4) Only the TE mode solutions will be analysed, since TE modes can be excited independently from TM modes. For the X-cut crystals analyzed experimentally these modes correspond to the extraordinary modes which encounter the extraordinary index and are influenced by the r_{33} electro-optic coefficient. Any polarization rotations at the interface are also neglected since the propagation di- ⟨
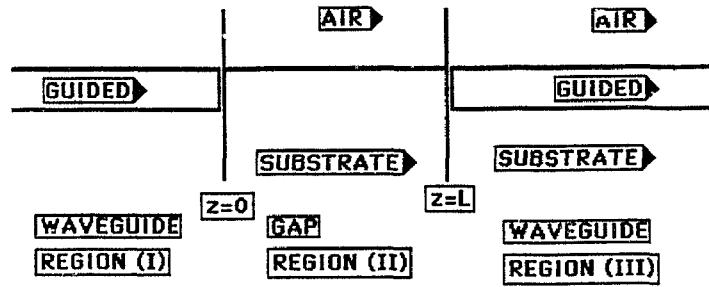
Figure C.1: Geometrical arrangement of waveguide with gap and the modes of propagation.

rections are along the principle axis of the crystal.

5) In the analysis it is not necessary to consider magnetic field components since the use of Maxwell's equation enables these fields to be written in terms of electric fields.

C.2 Derivation of the Power Coupling Expression

C.2.1 Region (I)

The solution to the wave equation of region (I) for arbitrary index profile is given in equation C.1. The notation stresses the fact that the mode expressions are to be used in region (I) only.

$$E_m^I(x,y,z) = \psi_m^I(x,y)e^{-i\beta_m^I z} \qquad (C.1)$$

The allowed values of the propagation cons_ant, β_m^I, range from $n_3 \leq \frac{\beta_m^I}{k_O} \leq n_2$ and are solved for using the techniques of chapter 3.

C.2.2 Region (II)

The solutions to the wave equation in region (II) can be expressed as a continuum of radiation modes. These modes, like bound modes, obey nearly all of the general properties outlined in chapter 3. The essential difference between guided and radiation modes is that there is no eigenvalue equation for the propagation constants, because of the relaxation of the boundary condition that the fields are zero at infinity. Furthermore, at large distances from the waveguide, their fields are oscillatory. There are two regimes for the β_m^{II} values. The first is that of the substrate modes given by $n_3 \leq \frac{\beta_m^{II}}{k_o} \leq n_1$ and the second that of the air modes given by $0 \leq \frac{\beta_m^{II}}{k_o} \leq n_1$.

The continuum of substrate modes in region (II) has the electric field expressed as:

$$E_{ms}^{II}(x,y,z) = \int_{n_1 k_o}^{n_3 k_o} \psi_{ms}^{II}(x,y)e^{-i\beta_{ms}^{II}z}d\beta_{ms}^{II} \qquad (C.2)$$

The air modes are expressed as:

$$E_{ma}^{II}(x,y,z) = \int_0^{n_1 k_o} \psi_{ma}^{II}(x,y)e^{-i\beta_{ma}^{II}z}d\beta_{ma}^{II} \qquad (C.3)$$

C.2.3 Region (III)

The waveguide of region (III) being exactly the same as that of region (I) enables writing of the electric field solutions for the guided modes by replacing the superscript (I) by (III). In this region the radiated profile due to the presence of the gap may induce other modes of different order than the one launched in the initial waveguide. To account for the generation of these modes the substitution of (n) for (m) is made in (C.1). The possibility of having both substrate and air modes in this region can also be accounted for, in the theory, using the expressions of region (II).

C.2.4 Coupling Region (I) to (II)

The continuity of the electric field at $z = 0$ can be expressed as:

$$E_m^I(x, y, 0) = \int_{n_1 k_o}^{n_3 k_o} D_s^{II}(\beta_{ms}^{II}) \psi_{ms}^{II}(x, y, 0) d\beta_{ms}^{II}$$

$$+ \int_0^{n_1 k_o} D_a^{II}(\beta_{ma}^{II}) \psi_{ma}^{II}(x, y, 0) d\beta_{ma}^{II} \qquad (C.4)$$

where the D_i^{II} spectrum of coefficients determines the power converted from the guided mode of region (I) into the radiation modes of region (II). Using the orthogonality condition of the modes, equation (3.13), the D_i^{II} coefficients can be expressed as:

$$D_s^{II}(\beta_{ms}^{II}) = \frac{\frac{\beta_{ms}^{II}}{k_o}}{2\sqrt{\frac{\mu_o}{\epsilon_o}}} \int_{-\infty}^{+\infty} \int_{-\infty}^{+\infty} \psi_m^I(x, y) \psi_{ms}^{II*}(x, y) dx dy \qquad (C.5)$$

$$D_a^{II}(\beta_{ma}^{II}) = \frac{\frac{\beta_{ma}^{II}}{k_o}}{2\sqrt{\frac{\mu_o}{\epsilon_o}}} \int_{-\infty}^{+\infty} \int_{-\infty}^{+\infty} \psi_m^I(x, y) \psi_{ma}^{II*}(x, y) dx dy \qquad (C.6)$$

Using these coefficients the total electric field propagating in region (II) may be expressed as:

$$E_{tot}^{II}(x, y, z) = \int_{n_1 k_0}^{n_3 k_o} D_s^{II}(\beta_{ms}^{II}) \psi_{ms}^{II}(x, y) e^{-i\beta_{ms}^{II} z} d\beta_{ms}^{II} +$$

$$\int_0^{n_1 k_o} D_a^{II}(\beta_{ma}^{II}) \psi_{ma}^{II}(x, y) e^{-i\beta_{ma}^{II} z} d\beta_{ma}^{II} \qquad (C.7)$$

Equation (C.7) represents the closed form expression of the electric field in region (II) as a function of x, y and z which depends on the input mode electric field profile of region (I) through the D_i^{II} coefficients.

C.2.5 Coupling Regions (II) and (III)

The electric field profile at the interface ($z = L$) can be obtained from the expression of $E_{tot}^{II}(x,y,z)$ by setting $z = L$. Once again the continuity of the electric

field at this interface between the mode components of regions (II) and (III) can be expressed in a simple form since the field profiles are known in both regions. Coupling back into the same mode that was excited in region (I), this is explicitly written as:

$$E_{tot}^{II}(x,y,L) = G_m E_m^I(x,y,0) \qquad (C.8)$$

Expanding both sides in terms of the ψ's:

$$G_m \psi_m^I(x,y) = \int_{n_1 k_o}^{n_3 k_o} D_s^{II}(\beta_{ms}^{II}) \psi_{ms}^{II}(x,y) e^{-i\beta_{ms}^{II} L} d\beta_{ms}^{II} +$$

$$\int_0^{n_1 k_o} D_a^{II}(\beta_{ma}^{II}) \psi_{ma}^{II}(x,y) e^{-i\beta_{ma}^{II} L} d\beta_{ma}^{II} \qquad (C.9)$$

The coupling coefficient G_m can be obtained by applying the orthogonality of the modes and is expressed as:

$$G_m = \frac{\frac{\beta_m^I}{k_o}}{2\sqrt{\frac{\mu_o}{\epsilon_o}}} \int_{-\infty}^{+\infty} \int_{-\infty}^{+\infty} \int_{n_1 k_o}^{n_3 k_o} D_s^{II}(\beta_{ms}^{II}) \psi_{ms}^{II}(x,y) e^{-i\beta_{ms}^{II} L} d\beta_{ms}^{II} \psi_m^{I*}(x,y) dx dy +$$

$$\frac{\frac{\beta_m^I}{k_o}}{2\sqrt{\frac{\mu_o}{\epsilon_o}}} \int_{-\infty}^{+\infty} \int_{-\infty}^{+\infty} \int_0^{n_1 k_o} D_a^{II}(\beta_{ma}^{II}) \psi_{ma}^{II}(x,y) e^{-i\beta_{ma}^{II} L} d\beta_{ma}^{II} \psi_m^{I*}(x,y) dx dy \qquad (C.10)$$

Equation (C.10) can be simplified by changing the order of the integrations and recaling the form of the D_i^{II} coefficients. The simplified form is:

$$G_m = \int_{n_1 k_o}^{n_3 k_o} |D_s^{II}(\beta_{ms}^{II})|^2 e^{-i\beta_{ms}^{II} L} d\beta_{ms}^{II} + \int_0^{n_1 k_o} |D_a^{II}(\beta_{ma}^{II})|^2 e^{-i\beta_{ma}^{II} L} d\beta_{ma}^{II} \qquad (C.11)$$

The power in the guided mode of region (III) at z = L can be expressed as:

$$P = \frac{\frac{\beta_m^I}{k_o}}{2\sqrt{\frac{\mu_o}{\epsilon_o}}} \int_{-\infty}^{+\infty} \int_{-\infty}^{+\infty} G_m G_m^* \psi_m^I(x,y) \psi_m^{I*}(x,y) dx dy \qquad (C.12)$$

or, simply by using the orthogonality relation, as:

$$P = G_m G_m^* \qquad (C.13)$$

If the expansion of the $G_m G_m^*$ term is carried out, four terms result. The power coupled can be expressed in simple form as:

$$P = T_s + T_a + T_{as} + T_{sa} \qquad (C.14)$$

The term T_s represents power from the input guide converted to substrate modes and then coupled back to the guided mode in region (III) and is expressed as:

$$T_s = |\int_{n_1 k_o}^{n_3 k_o} \frac{\beta_m^I}{\beta_{ms}^{II}} (D_s^{II}(\beta_m^{II}))^2 e^{-i\beta_{ms}^{II}L} d\beta_{ms}^{II}|^2 \qquad (C.15)$$

The term T_a is the term which represents power from the input guide converted to air modes and then coupled back to the guided mode in region (III) and is expressed as:

$$T_a = |\int_0^{n_1 k_o} \frac{\beta_m^I}{\beta_{ma}^{II}} (D_a^{II}(\beta_m^{II}))^2 e^{-i\beta_{ma}^{II}L} d\beta_{ma}^{II}|^2 \qquad (C.16)$$

The terms T_{sa} and T_{as} represent interactions (phase interference) between the various modes and are expressed as:

$$T_{sa} = |\int_{n_1 k_o}^{n_3 k_o} \frac{\beta_m^I}{\beta_{ms}^{II}} (D_s^{II}(\beta_m^{II}))^2 e^{-i\beta_{ms}^{II}L} d\beta_{ms}^{II}|| \int_0^{n_1 k_o} \frac{\beta_m^I}{\beta_{ma}^{II}} (D_a^{II}(\beta_m^{II}))^2 e^{-i\beta_{ma}^{II}L} d\beta_{ma}^{II}|^* \qquad (C.17)$$

$$T_{as} = |\int_{n_1 k_o}^{n_3 k_o} \frac{\beta_m^I}{\beta_{ms}^{II}} (D_s^{II}(\beta_m^{II}))^2 e^{-i\beta_{ms}^{II}L} d\beta_{ms}^{II}|^*| \int_0^{n_1 k_o} \frac{\beta_m^I}{\beta_{ma}^{II}} (D_a^{II}(\beta_m^{II}))^2 e^{-i\beta_{ma}^{II}L} d\beta_{ma}^{II}| \qquad (C.18)$$

In region (III), there is also the possibility of having other modes which are guided solutions of the wave equation and are not initially excited in region (I). The coupling coefficients to any one of these modes at interfaces (II)-(III) can be expressed as:

$$G_n = \frac{\frac{\beta_n^{III}}{k_o}}{2\sqrt{\frac{\mu_o}{\epsilon_o}}} \int_{-\infty}^{+\infty} \int_{-\infty}^{+\infty} E^{II}(x,y,L)\psi_n^{III*}(x,y)dxdy \qquad (C.19)$$

In region (III) there is the further possibility of having substrate and air modes defined as in region (II). Normally when designing a device these modes

would be neglected since they represent power which is not coupled to the waveguide and is not measured. The coupling coefficients to the substrate and air modes can be expressed as G_s and G_a, repectively, as given by expressions similar to equation (C.19).

Derived is the power coupling expression for a pair of waveguides separated by a gap region that contains an interface. The coupling coefficient G_m multiplied by its complex conjugate represents an optical power transfer function. The technique used here to treat the coupling can be employed to treat other coupling geometries.

APPENDIX D. GAP DEVICE BASED ON COUPLING THEORY

A device design which can alter the coupling efficiency of the modes across the gap is shown in figure D.1. The waveguides are oriented such that they run parallel to the X axis for Y-cut crystals or to the Y axis for X-cut crystals. The electrodes are positioned parallel to the waveguides and along the length of the gap region.

For this waveguide-electrode and crystal orientation, n_2 corresponds to the extraordinary index, n_e. When a voltage is applied to the electrodes, a highly confined electric field is set up inside the crystal between the electrodes with components given by[128,129]:

$$E_x = \frac{V n_e}{\pi n_o} \frac{sin(\phi/2)}{\sqrt{\sqrt{(a^2 + y^2 - x^2)^2 + (2xy)^2}}} \qquad (D.1)$$

$$E_y = \frac{V}{\pi} \frac{cos(\phi/2)}{\sqrt{\sqrt{(a^2 + y^2 - x^2)^2 + (2xy)^2}}} \qquad (D.2)$$

where $tan(\phi) = 2xy/(a^2 + y^2 - x^2)$, and 2a is the electrode spacing, x represents the depth coordinate from the top surface of the crystal, and y is measured parallel to the waveguide with the origin at the centre of the waveguide.

In chapter 2, the electro-optic effect has been discussed and it has been shown that an applied electric field produces a change in the extraordinary index of refraction given by:

$$\Delta n_2(x,y) = \frac{-1}{2} r_{33} n_2^3 E_y(x,y) \qquad (D.3)$$

In the derivation of the coupled power expression across the gap, the effects of
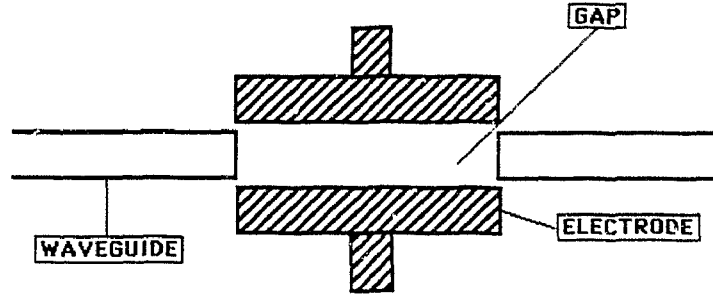
Figure D.1: Gap based device design.

changing the index of refraction, n_2, in region (II) must be included in the analysis of appendix C. The index of refraction is no longer uniform but varies as:

$$n_2(x,y) = n_2 + \Delta n_2(x,y) \qquad (D.4)$$

In region (II) the modal solutions must be altered to account for the index change. For an applied voltage which increases the index $n_2(x,y)$, i.e. $\Delta n_z(x,y) \geq 0$, the modal radiation fields can be written as:

$$E^{II} = E^{II}_{mE} + E^{II}_{ms} + E^{II}_{ma} \qquad (D.5)$$

where

$$E^{II}_{mE} = \int_{n_2 k_o}^{n_2 k_o + \Delta n_2(x,y) k_o} \psi^{II}_{mE}(x,y) e^{-i\beta^{II}_{mE} z} d\beta^{II}_{mE} \qquad (D.6)$$

where E^{II}_{mE} is the contribution to the electric field due to new modes guided in the higher index region. The expression describing the coupling from region (I) to (II) will have the additional term in equation (C.7):

$$\int_{n_2 k_o}^{n_2 k_o + \Delta n_2(x,y) k_o} (D^{II}_E(\beta^{II}_{mE}) \psi^{II}_{mE}(x,y) d\beta^{II}_{mE} \qquad (D.7)$$

with $D^{II}_E(\beta^{II}_{mE})$ expressed similarly to those of equations (C.5) and (C.6). Working through the derivation the G_m coefficient will now contain an additional factor in equation (C.10) of the form:

$$\int_{n_2 k_o}^{n_2 k_o + \Delta n_2(x,y) k_o} \frac{\beta^I_m}{\beta^{II}_{mE}} (D^{II}_E(\beta^{II}_{mE}))^2 e^{-i\beta^{II}_{mE} L} d\beta^{II}_{mE} \qquad (D.8)$$

The total power coupled to region (III) can be expressed in the contracted notation as:

$$P_{tot} = T_a + T_s + T_{as} + T_{sa} + \mathbf{T_E} + \mathbf{T_{Es}} + \mathbf{T_{Ea}} + \mathbf{T_{sE}} + \mathbf{T_{aE}} \qquad (D.9)$$

Comparing this expression with (C.14) shows that five new terms exist which represent contributions to the total coupled power due to the new modes of the higher index region caused by the electro-optic effect and applied voltage.

The new terms in expression (C.9) represent power coupling from the guided mode of region (I) into the new modes of region (II). These modes can then couple directly into region (III) guided modes, $(\mathbf{T_E})$, or exchange power with the substrate and air modes $(\mathbf{T_{Ea}}, \mathbf{T_{Es}})$ before coupling to region (III). The other two terms represent power from the substrate and air modes which couple to the new modes before coupling to region (III).

The other two electric field contributions to (C.5) will also be influenced by the increased index region. Considering the modal functional form of the substrate and air modes, their amplitudes will be larger where the index of refraction is larger, i.e. in the induced increased index region. As a result the power carried by these modes will be larger in the gap region when the index is increased.

The set of new modes and the increased amplitude of the old modes in the higher index region combine to focus the power in the gap region. If no new modes are created there is still a focusing of power observed since the substrate and air modes will contain larger amplitudes in the gap region between the interfaces and equation (C.9) can be used with the new modal field profiles.

The index of refraction increase in region (II) results in the creation of a profile similar to that of figure 3.10. The index increase partially bridges the gap between the guides by inducing a waveguide-like index layer. It has the effect of the converging lens concept introduced at the begining of chapter 3 and shown in figure D.2.
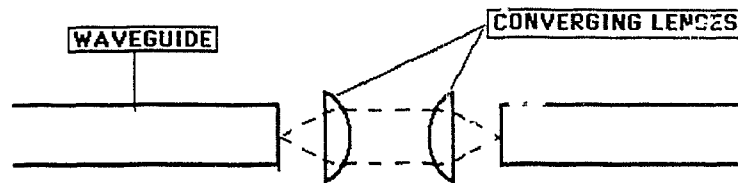
Figure D.2: Effect of converging lens in gap region.

When voltage is applied so as to decrease the index $n_2(x,y)$, the modal field components of (D.5) are given by:

$$E_{mE}^{II} = \int_{n_2 k_o}^{n_2 k_o + \Delta n_2(x,y)k_o} \psi_{mE}^{II}(x,y) e^{-i\beta_{mE}^{II}z} d\beta_{mE}^{II} \qquad (D.10)$$

and

$$E_{ms}^{II} = \int_{n_2 k_o}^{n_2 k_o + \Delta n_2(x,y)k_o} \psi_{ms}^{II}(x,y) e^{-i\beta_{ms}^{II}z} d\beta_{ms}^{II} \qquad (D.11)$$

where the expression for E_{ma}^{II} remains retains its same functional form. The field components of E_{mE} in the decreased index region will be exponentially decaying (evanescent) in that region. The wave components for E_{ms} and E_{ma} will be real in the decreased index region but will now have a smaller amplitude than when no voltage is applied to the electrodes. The total power coupled to region (III) is now smaller since the decreased index region has the effect of increasing the lateral spreading of power. The negative index increase in region (II) has the effect of producing an antiguide-like layer between the waveguide ends with an overall effect much as the diverging lens shown in figure D.3.

For this geometry of waveguide and electrodes the coupling theory has been reworked to include electro-optic effects. It is shown that, through the application of a voltage, the coupling coefficient and coupled power can be altered, a feature useful in design of devices such as modulators, attenuators and switches.

In this appendix the effect of applying a voltage to the electrodes placed in the gap region has been discussed. A new power coupling expression has been
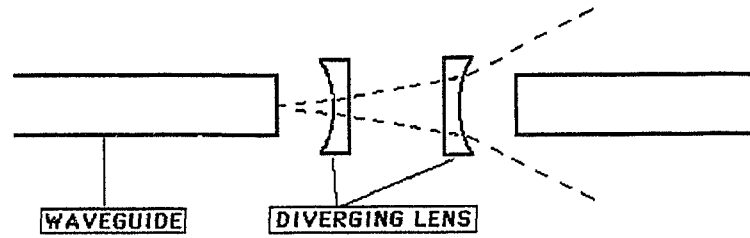
Figure D.3: Effect of diverging lens in gap region.

developed when the increased index region allows for new modes to be valid solutions of the wave equation. In the event that no new modes are created the change in the functional form of the substrate and air modes are discussed.

REFERENCES

1. J. M. Stone, <u>Radiation and Optics</u>, McGraw-Hill Book Company, New York, 1963, p. 420.

2. A. Yariv and P. Yeh, <u>Optical Waves in Crystals</u>, John Wiley and Sons, New York, 1984, p. 2.

3. A. Yariv and P. Yeh, <u>Optical Waves in Crystals</u>, John Wiley and Sons, New York, 1984, p. 70.

4. F. Ayres, Jr., <u>Matrices</u>, McCraw-Hill Book Company, New York, 1962, p. 163.

5. M. R. Spiegel, <u>Theoretical Mechanics</u>, McGraw-Hill Book Company, New York, 1967, p. 168.

6. F. A. Jenkins and H. E. White, <u>Fundamentals of Optics</u>, McGraw-Hill Book Company, New York, 1937, p. 560.

7. R. G. Hunsperger, <u>Integrated Optics: Theory and Technology</u>, Springer-Verlag, Berlin, 1985, p. 123.

8. A. Yariv and P. Yeh, <u>Optical Waves in Crystals</u>, John Wiley and Sons, New York, 1984, p. 232.

9. I. P. Kaminow and E. H. Turner, "Electro-optic light modulators", Proc. IEEE, Vol 54, No. 10, p. 1374, Oct. 1966.

10. A. Yariv and P. Yeh, <u>Optical Waves in Crystals</u>, John Wiley and Sons, New York, 1984, p. 222.

11. G. Arfken, <u>Mathemetical Methods for Physicists</u>, Academic Press, New York, 1970, p. 42.

12. A. Kumar and E. Khular, "A perturbation analysis for modes in diffused waveg-

uides with a Gaussian profile", Optics Comm., Vol. 27, No. 3, 1978, p. 349.

13. C. Pichot, "The inhomogeneous slab, a rigorous solution to the propagation problem", Optics Comm., Vol. 23, No. 2, 1977, p. 285.

14. P. Mishra and A. Sharma, "Analysis of single mode inhomogeneous planar waveguides", J. Lightwave Technol., Vol. LT-4, No. 2, 1986, p. 204.

15. A. Reisinger, "Characteristics of optical guided modes in lossy waveguide", Appl. Opt., Vol. 12, No. 5, 1973, p. 1015.

16. J. Janta and J. Ctyroky, "On the accuracy of the WKB analysis of TE and TM modes in planar graded-index waveguides", Optics Comm., Vol. 25, No. 1, 1978, p. 49.

17. A. Gedeon, "Comparison between rigorous theory and the WKB-analysis of modes in graded-index waveguides", Optics Comm., Vol. 12, No. 3, 1974, p. 329.

18. D. Marcuse, "TE modes of graded-index slab waveguides", IEEE J. Quantum Electron., Vol QE-9, No. 10,1973, p. 1000.

19. A. Voltenkov and V. Mogilevich, "Determination of the refractive index profile of few-mode planar waveguides", Sov. J. Quantum Electron., Vol. 13, No. 10, 1983, p. 1423.

20. V. Ramaswamy and R. Lagu, "Numerical field solutions for an arbitrary asymmetrical graded-index planar waveguide", J. Lightwave Technol., Vol. LT-1, No. 2, 1983, p. 408.

21. G. Hocker and W. Burns, "Modes in diffused optical waveguides of arbitrary index profile", IEEE J. Quantum Electron., Vol. QE-11, No. 6, 1975, p. 270.

22. H. Kogelnik and V. Ramaswamy, "Scaling rules for thin-film optical waveguides", Appl. Opt., Vol. 13, No. 8, 1974, p. 1857.

23. E. Marcatili, "Dielectric rectangular waveguide and directional coupler for integrated optics", Bell Syst. Tech. J., Vol. 48, 1969, p. 2071.

24. J. Goell and R. Standley, "Integrated optical circuits", Proc. IEEE, Vol. 58, No. 10, 1970, p. 1504.

25. J. Noda and M. Fukuma, "Optical field calculation of impurity diffused channel waveguides by linear segment layer approximation", Appl. Opt., Vol. 19, No. 17, 1980, p. 2897.

26. R. Lagu and V. Ramaswamy, "A variational finite-difference method for analysing channel waveguides with arbitrary index profiles", IEEE J. Quantum Electron., Vol. QE-22, No. 6, 1986, p. 968.

27. C. Pichot, "Exact numerical solution for the diffused channel waveguide", Optics Comm., Vol. 41, No. 3, 1982, p. 169.

28. H. Taylor, "Dispersion characteristics of diffused channel waveguides", IEEE J. Quantum Electron., Vol QE-12, No. 12, 1976, p. 748.

29. C. Yeh, S. Dong and W. Oliver, "Arbitrary shaped inhomogeneous optical fibre and integrated optical waveguides", J. Appl. Phys., Vol. 46, No. 5, 1975, p. 2125.

30. M. Matsuhara, "Analysis of TEM modes in dielectric waveguides, by a variational method", J. Opt. Soc. Am., Vol. 63, No. 12, 1973, p. 1514.

31. E. Schweig and W. Bridges, "Computer analysis of dielectric waveguides: a finite-difference method", IEEE Trans. Microwave Theory and Tech., Vol. MTT 32, No. 5, 1984, p. 531.

32. A. Hallam, I. Bennion and W. Stewart, "Photochromic stripe waveguides for integrated optics", First European Conference on Integrated Optics, 14-15 Sept., 1981, p. 26.

33. K. Biedermann and O. Holmgen, "Large-size distortion-free computer-generated holograms in photoresist", Appl. Opt., Vol. 16, No. 8, 1977, p. 2014.

34. I. Ben-David, S. Berlowitz, M. Itzkowitz, S. Ruschin and N. Croitoru, "Laser beam photolithographic system for integrated optics applications", Ecio'85, Berlin, Germany, 1985, p. 34.

35. Y. Rytz-Froidevaux, R. Salathe and H. Gilgen, "Laser generated microstrutures", Appl. Phys. A, Vol. 37, 1985, p. 121.

36. K. Wilson, C. Mueller and E. Garmire, "Laser writing of masks for integrated optical circuits", IEEE Trans. on Comp., Hybrids and Manu. Tech., Vol. CHMT-5, No. 2, 1982, p. 202.

37. R. Becker, B. Sopori and W. Chang, "Focused laser lithographic system", Appl. Opt., Vol. 17, No. 7, 1978, p. 1069.

38. R. Gauthier, J. Chrostowski, B. Paton and M. Cada, "Mask making using a laser writing system", SPIE's Fiber LASE'86, Cambridge, Massachusetts, USA. Sept. 14-26, 1986, paper 704-20.

39. J. Crank, The Mathematics of Diffusion, Oxford University Press, New York, 1975.

40. G. Hocker and W. Burns, "Mode dispersion in diffused channel waveguides by the effective index method", Appl. Opt., Vol. 16, No. 1, 1977, p. 113.

41. M. Fukuma and J. Noda, "Optical properties of titanium-diffused $LiNbO_3$ strip waveguides and their coupling-to-a-fibre characteristics", Appl. Opt., Vol. 19, No. 4, 1980, p. 591.

42. A. Kumar and E. Khular, "A pertubation analysis for modes in diffused waveguides with a Gaussian profile", Opt. Comm., Vol. 27, No. 3, 1978, p. 349.

43. G. Hocker and W. Burns, "Modes in diffused optical waveguides of arbitrary index profile", IEEE J. Quantum Electron., QE-11, No. 6, 1975, p. 270.

44. R. Steinberg and T. Giallorenzi, "Performance limitations imposed on optical waveguide switches and modulators by polarization", Appl. Opt., Vol. 15, No. 10, 1976, p. 2440.

45. J. Feth and C. Chang, "Metal-clad fibre-optic cutoff polarizer", Opt. Lett., Vol. 11, No. 6, 1986, p. 386.

46. T. Findakly, B. Chen and D. Booher, "Single-mode integrated-optical polarizers in $LiNbO_3$ and glass waveguides", Opt. Lett., Vol. 8, No. 12, 1983, p. 641.

47. S. Uehara, T. Izawa and H. Nakagome, "Optical waveguide polarizers", Appl. Opt., Vol. 13, No. 8, 1974, p. 1753.

48. T. Takano and J. Hamasaki, "Propagating modes of a metal-clad-dielectric-slab waveguide for integrated optics", IEEE J. Quantum Electron., Vol. QE-8, No. 2, 1972, p. 206.

49. V. Fedoseev and P. Adamson, "Singularities in the absorption spectrum of guided TM modes in metal-dielectric heterostructures with narrow-gap electronic excitation of a buffer layer", Sov. J. Quantum Electron., Vol. 13, No. 10, 1983, p. 1320.

50. K. Thyagarajan, A. Kaul and S. Hosain, "Attenuation characteristics of single-mode metal-clad graded-index waveguides with a dielectric buffer: a simple and accurate numerical method", Opt. Lett., Vol 11, No. 7, 1986, p. 478.

51. J. Polky and G. Mitchell, "Metal-clad dielectric waveguide for integrated-optics", J. Opt. Soc. Am., Vol. 64, No. 3, 1974, p. 274.

52. Y. Suematsu, M. Hakuta, K. Furuya, K. Chiba and R. Hasumi, "Fundamental transverse electric field (TE_o) mode selection for thin-film asymmetric light guides", Appl. Phys. Lett., Vol. 21, No. 6, 1972, p. 291.

53. D. Eberhard and H. Bulow, "Single mode channel waveguide polarizer on $LiNbO_3$", integrated optics, Proceedings of the Third European Conference, ECIO'85, Berlin, Germany, 6-8 May, 1985, p. 202.

54. S. Wright, A. De Oliveira and M. Wilson, "Optical waveguide polarizer with synchronous absorption", Electron. Lett., Vol. 16, No. 17, 1979, p. 510.

55. Y. Yamamoto, T. Kamiya and H. Yanai, "Characteristics of optical guided modes in multiplayer metal-clad planar optical guide with low-index dielectric buffer layer", IEEE J. Quantum Electron., QE-11, No. 9, 1975, p. 729.

56. M. Masuda and J. Koyama, "Effects of a buffer layer on TM modes in a metal-clad optical waveguide using Ti-diffused $LiNbO_3$ C-plate", Appl. Opt., Vol. 16, No. 11, 1977, p. 2994.

57. K. Haegene and R. Ulrich, "Pyroelectric loss measurement in LiNbO$_3$:Ti guides", Opt. Lett. Vol. 4, No. 2, 1979, p. 60.

58. Y. Bourbin, A. Enard, M. Papuchon and K. Thyagarajan, "The local absorption technique: a straightforward characterization method for many optical devices", J. Light. Technol., Vol. LT-5, No. 5, 1987, p. 684.

59. J. Jackel and J. Vasalka, "Measuring losses in optical waveguides: a new method", Appl. Opt., Vol. 23, No. 2, 1984, p. 197.

60. K. Thyagarajan, Y. Bourbin, A. Enard, S. Vatoux and M. Papuchon, "Experimental demonstration of TM mode-attenuation resonance in planar metal-clad optical waveguides", Opt. Lett., Vol. 10,No. 6, 1985, p. 283.

61. R. Gauthier and B. Paton, "Alignment and evaluation of integrated optic components using an OTDR", SPIE Proceedings, Optical Testing and Metrology, Vol. 661, 3-6 June, 1986, Quebec City, Quebec, p.229.

62. G. Beni and S. Hackwood, "Electro-wetting displays", Appl. Phys. Lett., Vol. 38, No. 4, 1981, p. 207.

63. G. Beni, S. Hackwood and J. Jackel, "Continuous electro-wetting effect", Appl. Phys. Lett., Vol. 40, No. 10, 1982, p. 912.

64. J. Jackel, S. Hackwood, J. Veselka and G. Beni, "Electrowetting switch for multimode optical fibres", Appl. Opt., Vol. 22, No. 11, 1983, p. 1765.

65. K. Vetter, Electrochemical Kinetics, Academic Press, New York, 1967.

66. M. Cada, J. Ctyroky, I. Gregora and J. Schrofel, "WKB analysis of guided and semileaky modes in graded-index anisotropic optical waveguides", Opt. Comm., Vol. 28, No. 1, 1979, p. 59.

67. J. Ctyroky and M. Cada, "Generalized WKB method for the analysis of light propagation in inhomogeneous anisotropic optical waveguides", IEEE J. Quantum Electron., Vol. QE-17, No. 6, 1981, p. 1064.

68. W. Burns, S. Sheem and A. Milton, "Approximate calculation of leaky-mode loss coefficients for Ti-diffused LiNbO$_3$ waveguides", IEEE J. Quantum Electron.,

Vol. QE-15, No. 11, 1979, p. 1282.

69. W. Jiang and V. Ristic, "A simple solution for the wavenumber of off-axis modes in Y-Cut Ti:LiNbO$_3$ waveguides", IEEE J. Quantum Electron., Vol. QE-22, No. 6, 1986, p. 907.

70. J. Ctyroky, "Comments on approximate calculation of leaky-mode loss coefficients for ti-diffused LiNbO$_3$ waveguides", IEEE J. Quantum Electron., Vol. QE-16, No. 12, 1980, p. 1287.

71. S. Sheem, W. Burns and A. Milton, "Leaky-mode propagation in ti-diffused LiNbO$_3$ and LiTaO$_3$ waveguides", Opt. Lett., Vol. 3, No. 3, 1978, p. 76.

72. K. Yamanouchi, T. Kamiya and K. Shinbayama, "New leaky surface waves in anisotropic metal-diffused optical waveguides", IEEE Trans Microwave Theory Tech., Vol. MTT-26, No. 4, 1978, p. 298.

73. K. Yamanouchi, M. Yasumoto and K. Shibayama, "Optical switching device using leaky surface waves", IEEE J. Quantum Electron., Vol QE-14, No. 11, 1978, p. 863.

74. A. Nutt, "Experimental observations of light propagation in proton-exchanged lithium niobate waveguides", J. Opt. Commun., Vol. 6, No. 1, 1985, p. 8.

75. S. Yamamoto and Y. Okamura, "Guided-radiation mode interaction in off-axis propagation in anisotropic optical waveguides with application to direct-intensity modulators", J. Appl. Phys., Vol. 50, No. 4, 1979, p. 2555.

76. R. Gauthier, B. Paton, M. Cada and J. Chrostowski, "Integrated-optic attenuators", CAP Congress 1986, University of Alberta, Edmonton, AB., June 23-25, PG-10.

77. J. Stone, Radiation and Optics, McGraw Hill, New York, 1963, p. 156.

78. A. Snyder and J. Love, Optical Waveguide Theory, Chapman and Hill, New York, 1983, p. 514.

79. C. Angulo, "Diffraction of surface waves by a semi-infinite dielectric slab", IRE Trans. Antennas Propagat., Vol. Ap-5, 1957, p. 100.

80. E. Tamir, Integrated-Optics, Springer-Verlag, Berlin, 1962.

81. D. Marcuse, "Loss analysis of single-mode fibre splices", Bell System Tech. Journ., Vol. 56, No. 5, 1977, p. 703.

82. M. Bowman, P. Estenes, T. Joseph and X. Glavas, "Single mode optical rotary joint utilizing expanded beam optics", SPIE Proceedings Vol. 722, Cambridge, Mass., USA, Sept. 22-24, 1976, p. 722-40.

83. C. Seaton, X. Mai, G. Stegeman and H. Winful, "Nonlinear guided wave applications", Opt. Eng., Vol. 24, No. 4, 1985, p. 593.

84. G. Carter, Y. Chen and S. Tripathy," Intensity dependent index of refraction in organic materials", Opt. Eng., Vol. 24, No. 4, 1985, p. 609.

85. S. Jensen, "The nonlinear coherent coupler", IEEE J. Quantum Electron., Vol QE-18, No. 10, 1982, p. 1580.

86. S. Somekh, E. Garmire, A. Yariv, H. Garvin and R. Hunsperger, "Channel optical waveguide directional couplers",Appl. Phys. Lett., Vol.22, 1973, p. 47.

87. A. Yariv and P. Yeh, Optical Waves in Crystals, John Wiley and Sons, New York, 1984 , p. 459.

88. R. Alferness, G. Eisenstein, S. Korotky, R. Tucker, L. Buhl, I. Kaminow, C. Burrus and J. Veselka, "Mode locking a Ti:LiNbO$_3$-InGaAsP/InP composite cavity laser with an integrated high-speed directional coupler switch", Appl. Phys. Lett., Vol. 45, No. 9, 1984, p. 944.

89. M. Minakata, "Efficient LiNbO$_3$ balanced bridge modulator/switch with an ion-etched slot", Appl. Phys. Lett., Vol. 35, No. 1, 1979, p. 40.

90. R. Alferness, R. Schmidt and E. Turner, "Characteristics of Ti-diffused lithium niobate optical directional couplers", Appl. Opt., Vol. 18, No. 23, 1979, p. 4012.

91. O. Mikami, "LiNbO$_3$ coupled-waveguided TE/TM mode splitter", Appl. Phys. Lett., Vol. 36, No. 7, 1980, p. 491.

92. R. Schmidt, P. Cross and A. Glass, "Opically induced crosstalk in LiNbO$_3$ waveguide switches", J. Appl. Phys., Vol. 51, No. 1, 1980, p. 90.

93. O. Mikami and S. Zembutsu, "Modified balanced-bridge switch with two straight waveguides", Appl. Phys. Lett., Vol. 35, No. 2, 1979, p. 145.

94. D. Chemla and D. Miller, "Room-temperature excitonic nonlinear-optical effects in semiconductor quantum-well structures", J. Opt. Soc. Am. B., Vol. 2, No. 7, 1985, p. 1155.

95. D. Chemla, D. Miller and P. Smith, "Nonlinear optical properties of GaAs/GaAlAs multiple quantum well material: phenomena and applications", Opt. Eng., Vol. 24, No. 4, 1985, p. 556.

96. S. Smith, I. Janossy, H. Mackenzie, J. Matthew, J. Reid, M. Taghizadeh, F. Tooley and A. Walker, "Nonlinear optical circuit elements as logic gates for optical computers: the first digital optical circuits", Opt. Eng., Vol. 24, No. 4, 1985, p. 569.

97. D. Miller, D. Chemla, D. Eilenberger, P. Smith, A. Gossard and W. Tsang, " Large room-temperature optical nonlinearity in GaAs/Ga$_{1-x}$ Al$_x$As multiple quantum well structures", Appl. Phys. Lett., Vol. 41, No. 8, 1982, p. 679.

98. G. Stegeman, C. Seaton, J. Chilwell and D. Smith, "Nonlinear waves guided by thin films", Appl. Phys. Lett., Vol. 44, No. 9, 1984, p. 830.

99. C. Seaton, J.Valera, R. Shoemaker, G. Stegeman, J. Chilwell and S. Smith, "Anomalous nonlinear guided wave cut-off phenomena", Appl. Phys. Lett., Vol. 45, No. 11, 1984, p. 1162.

100. M. Cada, R. Gauthier, B. Paton and J. Chrostowski, "Nonlinear guided waves coupled nonlinearly in a planar GaAs/GaAlAs multiple quantum well structure", Appl. Phys. Lett., Vol. 49, No. 13, 1986, p. 755.

101. M. Cada and J. Begin, "GaAs/AlGaAs multiple quantum well nonlinear coupling element", Proceedings of the International Quantum Electronics Conference, IQEC'87, Baltimore, USA, 1987.

102. M. Papuchon, Y. Combemale, X. Mathieu, D. Ostrowsky, L. Reiber, A. Roy, B. Sejourne and M. Werner, "Electrically switched optical directional coupler: cobra", Appl. Phys. Lett., Vol. 27, No. 5, 1975, p. 289.

103. R. Alferness and R. Schmidt, "Tunable optical directional coupler filter", Appl. Phys. Lett., Vol. 33, No. 2, 1978, p. 161.

104. M. Cada, J. Glinski, Y. Leung and W. Leong, "Waveguide design for all-optical switching", Research Report of TUNS for BNR, Halifax, 1987.

105. M. Cada, R. Gauthier, B. Paton and j. Glinski "Multiple-quantum-well coupling element with losses", submitted to Appl.Phys. Lett., May, 1987

106. M. Cada, R. Gauthier and B. Paton, "Lossy nonlinear directional coupler", Orlando, USA, May 1987,

107. M. Cada, R. Gauthier, J. Chrostowski, B. Paton, "Multiple-quantum-well nonlinear coupler", Proceedings of SPIE, Integrated Optical Circuit Engineering, Vol. 704, Sept. 1986, Cambridge, USA.

108. P. Li KamWa, H. Marsh, P. Robson, J. Roberts and N. Mason, "Nonlinear propagation in GaAs/GaAlAs multiple quantum well waveguides", Proceedings of SPIE, Intergrated Optical Circuit Engineering II, Sept. 1985, Cambridge, USA, Vol. 578.

109. M. Kharusi, "Uniaxial and biaxial anisotropy in thin-film optical waveguides", J. Opt. Soc. Am., Vol. 64, No. 1, 1974, p. 27.

110. K. Yamanouchi, T. Kamiya and K. Shinbayama, "New leaky surface waves in anisotropic metal-diffused optical waveguides", IEEE Trans Microwave Theory Tech., Vol. MTT-26, No. 4, 1978, p. 298.

111. W. Burns and J. Warner, "Mode dispersion in optical waveguides", J. Opt. Soc. Am., Vol. 64, No. 4, 1974, p. 441.

112. W. Burns, S. Sheem and A. Milton, "Approximate calculation of leaky-mode loss coefficients for in-diffused LiNbO$_3$ waveguides", IEEE J. Quantum Electron., Vol. QE-15, No. 11, 1979, p. 1282.

113. W. Jiang and V. Ristic, "A simple solution for the wavenumber of off-axis modes in Y-Cut Ti:LiNbO$_3$ waveguides", IEEE J. Quantum Electron., Vol. QE-22, No. 6, 1986, p. 907.

114. E. Kolosvsky, D. Petrov, A. Tsarev and I. Yakovkin, "An exact method for analysing light propagation in anisotropic inhomogeneous optical waveguides", Opt. Comm., Vol. 43, No. 1, 1982, p. 21.

115. F. Jenkins and H. White, Fundamentals of Optics, McGraw-Hill, New-York, 1976, Chapter 26, p. 544.

116. R. Collin, "Field theory of guided waves", McGraw-Hill, New-York, 1960, Chapter 3.7, p. 97.

117. K. Cameron, "Simple and practical technique for attaching single-mode fibres to lithium niobate waveguides", Electron. Lett., Vol. 20, No. 23, 1984, p. 974.

118. V. Ramaswamy, R. Alferness and M. Divino, "High-efficiency single-mode fibre to Ti:LiNbO$_3$ waveguide coupling", Electron. Lett., Vol. 18, No.1, 1982, p. 30.

119. H. Hsu and A. Milton, "Single-mode coupling between fibres and indiffused waveguides", IEEE J. Quantum ectron., Vol. QE-13, No. 4, 1977, p. 224.

120. R. Keil and F. Auracher, "Coupling of single-mode Ti-diffused LiNbO$_3$ waveguides to single-mode fibres", Opt. Comm., Vol. 30, No. 1, 1979, p. 23.

121. W. Burns and G. Hocker, "End fire coupling between optical fibres and diffused channel waveguides", App. Opt., Vol. 16, No. 8, 1977, p. 2048.

122. O. Ramer, C. Nelson and C. Mohr, "Experimental integrated optic circuit losses and fibre pigtailing of chips", IEEE J. Quantum Electron., Vol. QE-17, No. 6, 1981, p. 970.

123. C. Bulmer, S. Sheem, R. Moeller and W. Burns, "High-efficiency flip-chip coupling between single-mode fibres and LiNbO$_3$ channel waveguides", Appl. Phys. Lett., Vol. 37, No. 4, 1980, p. 351.

124. R. Alferness, V. Ramaswamy, S. Korotky, M. Divino and L. Buhl, "Efficient single-mode fibre to titanium diffused lithium niobate waveguide coupling for $\lambda = 1.32~\mu$m", IEEE J. Quantum Electron., Vol. QE-18, No. 10, 1982, p. 1807.

125. R. Alferness and M. Divino, "Efficient fibre to X-cut Ti:LiNbO$_3$ waveguide coupling for $\lambda = 1.32~\mu$m", Electron. Lett., Vol. 20, No. 11, 1984, p. 465.

126. A. Yariv and P. Yeh, Optical Waves in Crystals, John Wiley and Sons, New York, 1984.

127. R. Hunsperger, Integrated Optics: Theory and Technology, Springer-Verlag, New York, 1985.

128. D. Marcuse, "Optimal electrode design for integrated-optics modulators", IEEE J. Quantum Electron., Vol. QE-18, No. 3, 1982, p. 393.

129. O. Ramer, "Integrated-optic electro-optic modulator electrode analysis", IEEE J. Quantum Electron., Vol. QE-18, No. 3, 1982, p. 386.